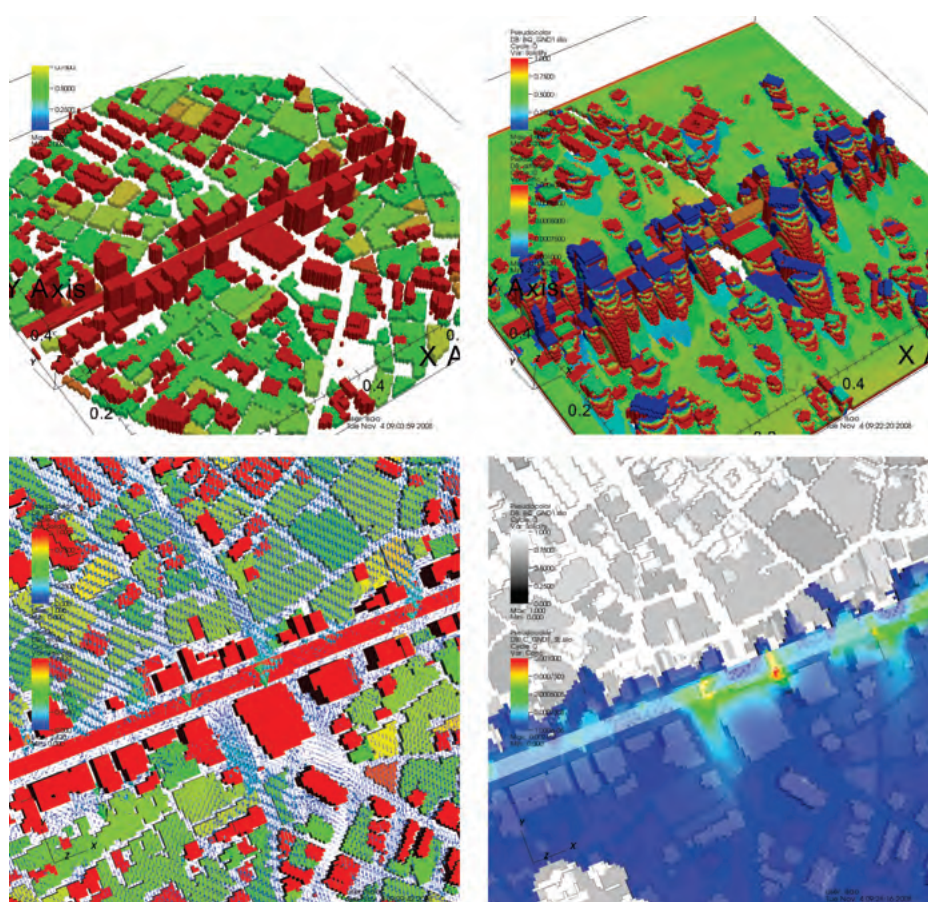


Development of a roadside atmospheric diffusion model MCAD



神田 勲、山尾幸夫、上原 清、大原利眞

Isao KANDA, Yukio YAMAOKA, Kiyoshi UEHARA, Toshimasa OHARA

NIES



独立行政法人 国立環境研究所

NATIONAL INSTITUTE FOR ENVIRONMENTAL STUDIES

Development of a roadside atmospheric diffusion model MCAD

神田 勲、山尾幸夫、上原 清、大原利眞

Isao KANDA, Yukio YAMAO, Kiyoshi UEHARA, Toshimasa OHARA

NIES

独立行政法人 国立環境研究所

NATIONAL INSTITUTE FOR ENVIRONMENTAL STUDIES

Foreword

This report summarizes the technical details, validation results, and application examples of the atmospheric diffusion model developed by the National Institute for Environmental Studies. This work was conducted in the SORA project (Study On Respiratory disease and Automobile exhaust) from 2005 to 2009 administered by the Ministry of Environment, Japan.

The model is able to simulate the complex diffusion behavior in street-scale geometries both rapidly and at high resolution.

The model is expected to be used in applications such as survey of air pollution status and atmospheric environment assessment on the street-scale.

Toshimasa Ohara
Director, Center for Regional Environmental Research

Contents

1	Introduction	1
2	Model description	7
2.1	Overview	9
2.2	MC method	10
2.3	AD method	32
2.4	Model implementation	43
3	Comparison with wind-tunnel experiments	45
3.1	Experimental method	47
3.2	Model parameters	48
3.3	Point source and uniform roughness	48
3.4	Line source and simple geometries	50
3.4.1	Oblique wind	55
3.4.2	Street canyon	57
3.4.3	Tall buildings	59
3.5	Real cities	61
3.5.1	City models	61
3.5.2	Results and comparison with a Gaussian-plume model	69
4	Extension to real-world situations	83
4.1	Hourly average concentration	85
4.1.1	Introduction	85
4.1.2	Review of field observations	86
4.1.3	Proposed method	91
4.1.4	Comparison with field observations	98
4.1.5	Summary and discussion	102
4.2	Emission along roads with signals	105
4.2.1	Introduction	105
4.2.2	Principles	105
4.2.3	Representative profile	126
4.2.4	Modification to sources.dat	128
4.2.5	Numerical integration of non-idling emission component	137
5	Summary	141

Abstract

This report describes an air-pollution prediction model MCAD for traffic-related emission in urban areas within a few hundred meters from relevant roads. The model adopts the mass-conservation (MC) principle for the velocity calculation and the advection-diffusion (AD) equation for the concentration calculation. This MC+AD combination allows low-cost calculation even with complex geometries. To compensate for the inherent deficiencies of MC and AD, as many known properties as possible of turbulent boundary-layer flow over obstacles are incorporated into the MC calculation, and the diffusivity in AD is derived from the velocity spectrum as a function of distance from the emission source.

The MCAD model is evaluated against wind-tunnel experiments for point-source emission in uniform urban canopy, line-source emission in street canyon, and along-road emission in reduced-scale real city geometries. MCAD performs well in relatively simple configurations, but the performance deteriorates substantially as the geometrical complexity increases. However, in terms of statistical evaluation indices, it is shown that MCAD performs distinctly better than a conventional Gaussian-plume model that neglects the effect of individual buildings.

In order to apply the model for prediction of hourly averages or prediction under low-wind-speed conditions, a spectral form in the AD step is proposed that accounts for the low-frequency and residual fluctuations observed in previous meteorological studies. Comparison with Gaussian models, which may be regarded as deduction from field observations, show that the proposed spectrum performs reasonably well.

Also, as a preprocessing step for the emission sources, we propose a method of redistributing emission strength in accordance to vehicle acceleration or deceleration near traffic signals. An emission distribution pattern is deduced from the traffic behavior in selected Japanese urban areas.

January 2012

Isao KANDA

Acknowledgements

The work was conducted as a part of the SORA project administered by the Japanese Ministry of Environment. The authors would like to thank Mr. S. Kagoshima for the construction of the wind-tunnel city models.

Chapter 1

Introduction

In urban areas, road vehicles are significant sources of air pollutants such as nitrogen oxide or suspended particulate matter. Although stricter emission regulations have reduced the overall pollution level, immediate neighborhoods of busy roads are still exposed to high pollutant concentration. To take effective countermeasures, it is necessary to estimate the concentration distribution and identify the relationship between the roadside obstacles and the concentration field. Estimation of the concentration field consists of emission and diffusion estimation steps. This report is concerned with diffusion estimation under neutral atmospheric stability within a few hundred meters from relevant roads, where the concentration contribution from the roads is comparable with that from the background.

There is a strong need for diffusion formulas or models that are numerically inexpensive and reasonably accurate. Numerical cost is important because annual-average exposure is often required since human health problems are usually caused through long-term exposure to pollutants. To estimate, say, an annual-average concentration near an intersection where two roads with different diurnal variation of pollutant emission rate meet, at least twice the number of wind directions (usually 32) cases need to be calculated because the ratio of contribution from the two roads differ every hour. If atmospheric stability or wind speed is a model parameter and their effect is not a simple multiplication by a spatially uniform coefficient, the number of necessary calculation cases increases further. Concentration in a particular hourly interval is estimated from these base calculation results for the corresponding weather and traffic conditions, and the annual average as the mean of 24×365 hourly values.

High accuracy is preferable but is not the highest priority for pollutant diffusion models. Even if a diffusion model that accurately reproduces controlled wind-tunnel experiments is employed, the predicted outdoor concentration is severely affected by the uncertainties in the emission estimation, the available meteorological data, and the geometrical database. Because small increase in accuracy of diffusion models often accompanies considerable increase in numerical cost, it is practical to employ diffusion models with accuracy compatible with those of other factors.

Various diffusion models have been developed previously. Due to the above-mentioned need for practically feasible models, equally ardent efforts have been paid to the developments of both numerically inexpensive moderate-accuracy models and numerically expensive high-accuracy ones. The numerically lightest and still widely used are the Gaussian-plume models, such as ISC (US-EPA 1987), ADMS (CERC 2007), AEROMOD (US-EPA 2004), OML (Olesen 1995), and METI-LIS (Kouchi *et al.* 2004), that use empirical and analytical formulas derived from field experiments. Although some of them (AEROMOD/PRIME, METI-LIS) account for the effect of an isolated building near the emission source, these models cannot estimate the effects of multiple buildings or structures in urban roadside areas. There are models for particular building configurations such as street canyons (*e.g.* STREET (Johnson *et al.* 1973), OSPM (Berkowicz 2000)), but their scope is limited to such special configurations. In contrast, models that resolve buildings by numerical grids and solve

fundamental physical equations can treat arbitrarily complex configurations but at a substantially higher numerical cost. However, because our concern is air pollution in roadside areas which are often geometrically complex, we shall focus on such building-resolving models.

There is a wide variety in building-resolving models. Most such models consist of velocity field calculation and concentration field calculation. Representative velocity calculation methods are mass-conserving (MC) method, mixing-length eddy-viscosity method, k - ϵ turbulent-viscosity (hereafter, k - ϵ) method, and large-eddy simulation (LES) method. The accuracy and numerical cost increase in this order. Except for MC, significant numerical cost is paid for the iterative solution of the momentum and turbulence-model equations. Concentration is calculated either by solving advection-diffusion (AD) equation or by tracking emitted fluid particles in the turbulent velocity field. A representative method of the latter is the Lagrangian stochastic model (LSM). Generally, the particle method has higher accuracy and requires higher numerical cost, but because turbulence parameters needed in the concentration calculation are derived from the velocity calculation results, the overall accuracy depends on the combination of the velocity and concentration calculation methods. Table 1.1 lists a few examples of previously studied combinations.

In this report, we present a model with the MC-AD combination, which requires less numerical cost than those in Table 1.1 and hence presumably has the lowest accuracy. Hereinafter, the model is called MCAD standing for the combination. A low-cost model is pursued because previously developed models are numerically demanding, and with today's computational power it is not feasible to use them for regulatory purposes where long-term averages at many urban sites need to be calculated on common PCs. The inevitable loss of accuracy is reduced as much as possible by specifying the initial velocity field in the MC step for a much wider variety of geometrical configurations than previous models based on the MC method and by specifying the eddy diffusivity in the AD step as a function of the distance from the emission source, which is more theoretically reasonable than the space-fixed eddy diffusivity employed in most AD-based models.

The outline of this report is as follows. Chapter 2 gives the overview of MCAD and describes the details of its main components: MC and AD methods. Chapter 3 evaluates MCAD against wind-tunnel diffusion experiments for geometries ranging from uniform block arrays to real-city shapes. Chapter 4 proposes two methods for dealing with real-world situations: one for estimating hourly-averaged concentration in the presence of meandering wind, and the other for estimating the emission distribution along roads with traffic signals. Summary and discussion are given in Chapter 5.

Table 1.1: Combinations of velocity and concentration calculation methods in previous studies. The list shows examples and is not exhaustive.

combination	references
MC-particle	Kaplan & Dinar (1996), Tinarelli <i>et al.</i> (1998), Williams <i>et al.</i> (2004)
mixing-length – AD	Moriguchi & Uehara (1993)
k- ϵ – AD	Eichhorn (1996), Yoshikawa & Kunimi (1998)
k- ϵ – particle	Dixon & Tomlin (2007)
LES – AD	Liu & Barth (2002)

Chapter 2

Model description

2.1 Overview

Our model MCAD is based on the work of Kaplan & Dinar (1996) who adopted the MC method for velocity calculation and LSM for concentration calculation. In Kaplan and Dinar's model, by using wind-tunnel results for the initial guess of the velocity field, the macroscopic flow patterns such as the shape of the recirculation zones around surface-mounted obstacles are calculated adequately whereas moderate-cost methods such as the $k - \epsilon$ method results in considerable errors due to inadequate turbulence modeling (Rodi 1997). In their model, near-source accuracy, which is poor with ordinary AD-based models, is achieved by adopting LSM.

In Kaplan & Dinar (1996), the initial guess of the velocity field was specified for street canyons and surface-mounted rectangular parallelepiped. In the real urban areas, however, there are other features that are amenable to modeling, *e.g.* urban canopy, elevated structures, or open areas. MCAD incorporates existing available formulas or experimental results for such features.

The LSM adopted by Kaplan & Dinar (1996), though theoretically satisfying for turbulent diffusion modeling, requires relatively fine numerical grids to produce smooth and reproducible concentration field (reproducibility problem arises from random flights of particles), and thus may lead to the loss of the cost advantage of using the MC method which is less demanding on numerical grids than other velocity calculation methods that solve momentum and turbulence-model equations.

The AD method, on the other hand, is far less costly than LSM, but has a problem that the near-source accuracy is low. The poor near-source accuracy cannot be overlooked because it is the near-source region where the concentration is high and is affected by the complexity of the building configuration. The low accuracy is due to the specification of the eddy diffusivity as a function of spatial coordinates but not as a function of the flight time of fluid particles containing pollutants emitted at the source. Because a fluid particle is affected by increasingly larger eddies as the flight time increases, the eddy diffusivity should increase with flight time until about the Lagrangian timescale of the ambient turbulence (Taylor 1921; Csanady 1973).

As a remedy to the above problem of AD, Csanady (1973) suggested defining the eddy diffusivity as a function of the distance from the emission source. For horizontal directions, in particular, the turbulence field may be regarded homogeneous and the eddy diffusivity can be derived from the velocity fluctuation spectra using Taylor's classical diffusion theory. Because distance-dependent eddy diffusivity has been successfully adopted by many authors (*e.g.* Sharan *et al.* 1996), we also adopt this scheme.

MCAD employs a numerical grid on which the relevant equations are discretized and are solved iteratively. A great advantage of adopting the MC method for velocity calculation is that the grid spacing need not be made progressively smaller toward solid walls. Hence, uniformly-sized grids are adopted with the spacing sufficiently small such that the salient features of the buildings and structures are resolved and the numerical diffusion in solving the AD

equations is not significant.

2.2 MC method

In the following, the spatial location is represented by the Cartesian coordinates (x, y, z) , where (x, y) are the horizontal coordinates and z is the vertical coordinate with the origin on the ground. The respective mean velocity components are denoted by (U, V, W) . Capitalized coordinates (X, Y, Z) represent local coordinates defined in special zones (described later). Bold symbols denote vectors.

First, the principle of the MC method is recapitulated from Kaplan & Dinar (1996). If an initial guess (U_i, V_i, W_i) is given, the MC method calculates a velocity field (U, V, W) that satisfies the mass conservation equation (assuming constant density)

$$\frac{\partial U}{\partial x} + \frac{\partial V}{\partial y} + \frac{\partial W}{\partial z} = 0, \quad (2.1)$$

and has the smallest L_2 -norm

$$I(U, V, W) = \iiint \alpha_x (U - U_i)^2 + \alpha_y (V - V_i)^2 + \alpha_z (W - W_i)^2 dx dy dz, \quad (2.2)$$

where $(\alpha_x, \alpha_y, \alpha_z)$ are weight functions. Introducing a Lagrange multiplier λ , minimizing $I(U, V, W)$ while satisfying (2.1) leads to minimizing

$$J(U, V, W; \lambda) = \iiint \alpha_x (U - U_i)^2 + \alpha_y (V - V_i)^2 + \alpha_z (W - W_i)^2 + \lambda \left(\frac{\partial U}{\partial x} + \frac{\partial V}{\partial y} + \frac{\partial W}{\partial z} \right) dx dy dz. \quad (2.3)$$

By the variational principle, we find

$$U = U_i + \frac{1}{2\alpha_x} \frac{\partial \lambda}{\partial x}, \quad V = V_i + \frac{1}{2\alpha_y} \frac{\partial \lambda}{\partial y}, \quad W = W_i + \frac{1}{2\alpha_z} \frac{\partial \lambda}{\partial z}.$$

By differentiating with respect to the corresponding coordinates, taking the sum, and applying (2.1), we obtain

$$\frac{\partial}{\partial x} \left(\frac{1}{2\alpha_x} \frac{\partial \lambda}{\partial x} \right) + \frac{\partial}{\partial y} \left(\frac{1}{2\alpha_y} \frac{\partial \lambda}{\partial y} \right) + \frac{\partial}{\partial z} \left(\frac{1}{2\alpha_z} \frac{\partial \lambda}{\partial z} \right) = -\frac{\partial U_i}{\partial x} - \frac{\partial V_i}{\partial y} - \frac{\partial W_i}{\partial z}, \quad (2.4)$$

The boundary conditions for this equation are

$$\lambda = 0 \quad \text{on the domain boundary}, \quad (2.5)$$

$$\frac{\partial \lambda}{\partial n} = 0 \quad \text{on solid walls}. \quad (2.6)$$

The equation (2.4) with the above boundary conditions is solved numerically by the incomplete Cholesky conjugate gradient method. The velocity field is obtained by substituting the solved λ into (2.4).

The quality of the solution (U, V, W) depends critically on the initial guess (U_i, V_i, W_i) . Especially, because deviatoric shear such as $\partial U/\partial z$ is not much altered by the MC procedure, shearing flows should be specified as accurately as possible. The initial field (U_i, V_i, W_i) is specified for the following zones in order of increasing priority.

- (i) ambient region
- (ii) in-between tall buildings
- (iii) far wake of tall buildings
- (iv) urban canopy
- (v) above open areas
- (vi) around elevated obstacles
- (vii) around surface-mounted obstacles
- (viii) street canyon

If a point is included in more than two zones of different category, the higher-number zones have priority. Definition of the zones and the initial velocity therein are explained below.

- (i) Ambient region

For the relatively low emission height of vehicular exhaust and a few-hundred-meter horizontal extent concerned here, it is sufficient to consider the flow only within the surface layer of approximately 150 m thick. In the surface layer, the velocity field is affected by the surface roughness but the effect of the Earth's rotation is negligible. For larger-scale problems such as emission from power plants, the whole boundary layer of approximately 600 m thick, where the Earth's rotation is important, needs to be considered. In the surface layer sufficiently high above buildings, the wind speed U_a can be approximated by the log law:

$$U_a = \frac{u_*}{\kappa} \ln \frac{z-d}{z_0}, \quad (2.7)$$

where u_* is the friction velocity, z_0 the roughness length, d the zero-plane displacement, and $\kappa = 0.4$ von Karman constant. Among various methods of determining the parameters z_0 and d (Grimmond & Oke 1999), we adopt the method proposed by Macdonald *et al.* (1998). By this method, we have

$$\frac{d}{\bar{H}} = 1 - \alpha^{-\lambda_p} (1 - \lambda_p), \quad (2.8)$$

$$\frac{z_0}{\bar{H}} = \left(1 - \frac{d}{\bar{H}}\right) \exp \left[- \left\{ \beta \frac{C_D}{2\kappa^2} \left(1 - \frac{d}{\bar{H}}\right) \lambda_f \right\}^{-1/2} \right], \quad (2.9)$$

where \bar{H} is the mean building height, $\alpha = 4.43$ is a constant determined for staggered arrays of cubes in a wind-tunnel experiment (Macdonald *et al.* 1998),

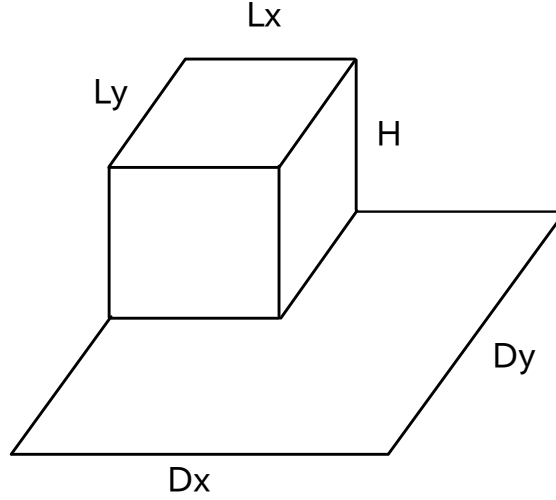


Figure 2.1: A building example. If the domain is filled with the pattern of this building, we substitute $D^2 = D_x D_y$, $L^2 = L_x L_y$, and $\overline{H} = H$ into (2.10).

$C_D = 1.2$ is the drag coefficient, and the plan-area ratio λ_p and the frontal area index λ_f are the parameters related to building density.

The mean building height \overline{H} is calculated as follows. First, the average height $\overline{\overline{H}}$ of all the buildings is calculated. Then, \overline{H} is calculated as the average of buildings excluding those taller than $2.5\overline{\overline{H}}$. Such tall buildings are treated in special manners in (ii) and (iii).

The parameters λ_p and λ_f are defined by

$$\lambda_p = \frac{L^2}{D^2}, \quad \lambda_f = \frac{L\overline{H}}{D^2}, \quad (2.10)$$

where D^2 is the average lot area per building and L^2 is the average horizontal-section area of a building (see Fig. 2.1 for an example).

The friction velocity u_* is determined from the given wind speed U_r at some reference height z_r .

(ii) In-between tall buildings

In urban areas, tall buildings are often close together and generate strong wind in-between them. We define tall buildings as those with height greater than $2.5\overline{\overline{H}}$. This height $2.5\overline{\overline{H}}$ is called the ‘blending height’ (Pasquill 1974) or ‘convergence height’ (Cheng & Castro 2002) as the height above which the vertical velocity profile becomes horizontally uniform if the building height has a uniform value \overline{H} . Thin stacks or water-reserve towers are excluded from tall buildings even if their height is greater than $2.5\overline{\overline{H}}$.

At sufficiently high position, we may assume that the flow is horizontal. Hence, except in the immediate neighborhood of tall buildings, the flow at a given height can be approximated by a two-component potential flow. (Note that the flow is two-component because the vertical component W is negligible. The flow is not two-dimensional because the wind speed varies with height.) In

the implemented code, a horizontal two-dimensional numerical grid is defined at each height with solid cells formed by the horizontal sections of tall buildings, and the Laplace equation $\nabla^2\phi$ for the velocity potential ϕ is solved with the boundary condition $\partial\phi/\partial n = U_a(z)(\cos\theta, \sin\theta)$, where θ is the wind direction angle, on the domain boundary. In the following, the solved potential flow is denoted by $\mathbf{U}_p(x, y, z) = \nabla\phi(x, y, z)$. Note that, in the immediate neighborhood of tall buildings, the higher priority zones (displacement, near-wake, and wake-diffusion) are applied.

(iii) Far wake of tall buildings

In the far wake of tall buildings, there is non-negligible velocity deficit from $\mathbf{U}_p(x, y, z)$. The geometry considered is shown in Fig. 2.2. Counihan *et al.* (1974) studied similarity solutions to surface-mounted 2D obstacles, and Taylor & Salmon (1993) extended the work to 3D obstacles introducing various empirical parametrizations. According to Taylor & Salmon (1993), the velocity deficit u' can be written as (with slight modification on H')

$$\frac{u'}{|\mathbf{U}_p(x_c, y_c, H)|} = \Gamma \tilde{C}_h \frac{W_{\text{eff}}}{H'} \left(\frac{X}{H'}\right)^{-3/2} F(\eta)G(\zeta), \quad (2.11)$$

where (x_c, y_c) is the coordinate of the center of the building, H is the height of the tall building, W_{eff} is the crosswind projection width of the building's horizontal section, $H' = H - d$ is the effective building height, and Γ and \tilde{C}_h are constants specified below. Note that, at the building top, $|\mathbf{U}_p(x_c, y_c, H)|$ is equal to $|U_a(H)|$. Also, note that we consider here the 'far' wake where the defect velocity obeys a similarity scaling. Therefore, trailing vortices or downwash in the near-wake region is not expressed by equation (2.11).

Functions $F(\eta)$ and $G(\zeta)$ representing, respectively, the horizontal and vertical profiles are defined by

$$F(\eta) = \frac{1}{\sqrt{2\pi}a_f} \exp\left(-\frac{\eta^2}{2a_f^2}\right), \quad \eta = \left(\frac{Y}{H'}\right) \left(\frac{X}{H'}\right)^{-1/2}, \quad (2.12)$$

$$G(\zeta) = c_a \zeta \exp(-a_g \zeta^{3/2}), \quad \zeta = \frac{z}{H'} \left(\frac{X}{H'}\right)^{-1/2}, \quad (2.13)$$

where c_a , a_f and a_g are given by

$$c_a = \sqrt{\frac{\ln \frac{H'+z_0}{z_0}}{2\kappa^2}}, \quad a_f = 0.5, \quad a_g = 0.67c_a^{3/2}.$$

The local coordinates (X, Y) are defined in Fig.1(a). The constant Γ is related to c_a by

$$\Gamma = 0.67c_a^2. \quad (2.14)$$

The constant \tilde{C}_h in (2.11) varies with the shape of the building. For cubical buildings, $0.2 \sim 0.35$ is recommended (Taylor & Salmon 1993). Tall buildings

are usually far from cubical, but because no alternative methods are available, we adopt the average value $\tilde{C}_h = (0.2 + 0.35)/2$ as a compromise.

We note that the equation (2.11) is valid in the far downwind region ($X \gg L_R$, where L_R is defined later as the downwind extent of the near-wake region) of the tall buildings. However, we apply (2.11) in $X > L_R$ as a gross approximation.

When there are multiple tall buildings upwind of the concerned point, the total deficit is calculated as a cumulative sum of the deficits from individual buildings calculated by (2.11). In other words, the defect velocity is calculated using the reduced velocity $|\mathbf{U}_p| - u'$ by the further upwind tall buildings. However, if we consider a road along which there are tall buildings, and which extends over multiple calculation domains, there will be substantial discontinuities in the wind speed at the domain borders where, on the inlet side, the wind is given unperturbed (model's assumption), but on the outlet side, the velocity is reduced by the upwind buildings. This is a problem inherent to models employing finite non-periodic domains.

The detailed procedure for multiple buildings is described below. For compactness, we write

$$f(X, Y, z, H', W_{\text{eff}}) = \Gamma \tilde{C}_h \frac{W_{\text{eff}}}{H'} \left(\frac{X}{H'} \right)^{-3/2} F(\eta) G(\zeta). \quad (2.15)$$

Then, the defect by the most upwind (0th) building becomes

$$U^{(0)}(H_0) f(X_0, Y_0, z, H'_0, W_{\text{eff},0}), \quad (2.16)$$

where $U^{(0)}(H_0)$ is the undisturbed ambient velocity at $z = H_0$, and H'_0 and $W_{\text{eff},0}$ are the effective height and width of the 0th building.

The velocity at the roof-top of the next upwind building (1st) is given by

$$U^{(1)}(H_1) = U^{(0)}(H_1) - U^{(0)}(H_0) f(X_0^1, Y_0^1, H_1, H'_0, W_{\text{eff},0}), \quad (2.17)$$

where X_0^1, Y_0^1 are the windward and crosswind coordinates of the 1st building with the origin at the 0th building. Then, the defect by the 1st building becomes

$$U^{(1)}(H_1) f(X_1, Y_1, z, H'_1, W_{\text{eff},1}). \quad (2.18)$$

Similarly, the velocity at the roof-top of the 2nd upwind building becomes

$$U^{(2)}(H_2) = U^{(1)}(H_2) - U^{(1)}(H_1) f(X_1^2, Y_1^2, H_2, H'_1, W_{\text{eff},1}), \quad (2.19)$$

and the defect by this building is

$$U^{(2)}(H_2) f(X_2, Y_2, z, H'_2, W_{\text{eff},2}). \quad (2.20)$$

Note that

$$U^{(1)}(H_2) = U^{(0)}(H_2) - U^{(0)}(H_0) f(X_0^2, Y_0^2, H_2, H'_0, W_{\text{eff},0}). \quad (2.21)$$

Thus, $U^{(i)}(H_i)$ must be calculated recursively.

In general, the roof-top velocity at the i 'th building becomes

$$U^{(i)}(H_i) = U^{(i-1)}(H_i) - U^{(i-1)}(H_{i-1})f(X_{i-1}^i, Y_{i-1}^i, H_i, H'_{i-1}, W_{\text{eff},i-1}), \quad (2.22)$$

where

$$U^{(i-1)}(H_i) = U^{(i-2)}(H_i) - U^{(i-2)}(H_{i-2})f(X_{i-2}^i, Y_{i-2}^i, H_i, H'_{i-2}, W_{\text{eff},i-2}), \quad (2.23)$$

$$U^{(i-1)}(H_{i-1}) = U^{(i-2)}(H_{i-1}) - U^{(i-2)}(H_{i-2})f(X_{i-2}^{i-1}, Y_{i-2}^{i-1}, H_{i-1}, H'_{i-2}, W_{\text{eff},i-2}), \quad (2.24)$$

...

Assuming that far wake defect is additive, although quite questionable, the velocity at (x, y, z) becomes

$$U^{(0)}(z) - \sum_{i=0}^{n-1} U^{(i)}(H_i)f(X_i, Y_i, z, H'_i, W_{\text{eff},i}), \quad (2.25)$$

where n is the number of tall buildings upwind of (x, y, z) .

Hereinafter, the ambient velocity after taking into account the far-wake defect by tall buildings is denoted by $\mathbf{U}_n(x, y, z)$ with $U_n = |\mathbf{U}_n|$. When U_n is written simply as $U_n(z)$, the dependence on (x, y) is understood.

(iv) Urban canopy

The log-law profile (2.7) is valid at z sufficiently higher than $z_0 + d$, say, above the blending height $2.5\overline{H}$. Below this height, there is non-negligible effect by individual buildings and the velocity field becomes horizontally inhomogeneous. In the wind-tunnel experiments by Cheng & Castro (2002), however, the log law is found valid if the velocity field is averaged horizontally for $z > \overline{H}$. Because, in the current model, the horizontally-averaged velocity field is sufficient for the purpose of securing moderate accuracy, we set the lower limit of the low-law profile at $z = \overline{H}$.

In the region below $z = \overline{H}$, called the urban canopy, the theory by Coceal & Belcher (2004) is applied. The velocity profile is obtained by solving a differential equation that expresses the balance between building drag and diffusion of momentum from above, *i.e.*

$$\frac{d}{dz} \left(l_m^2 \left(\frac{dU}{dz} \right)^2 \right) = \frac{U^2}{L_c}, \quad (2.26)$$

where L_c is the canopy-drag length scale defined by

$$L_c = \overline{H} \frac{1 - \lambda_p}{\lambda_f}, \quad (2.27)$$

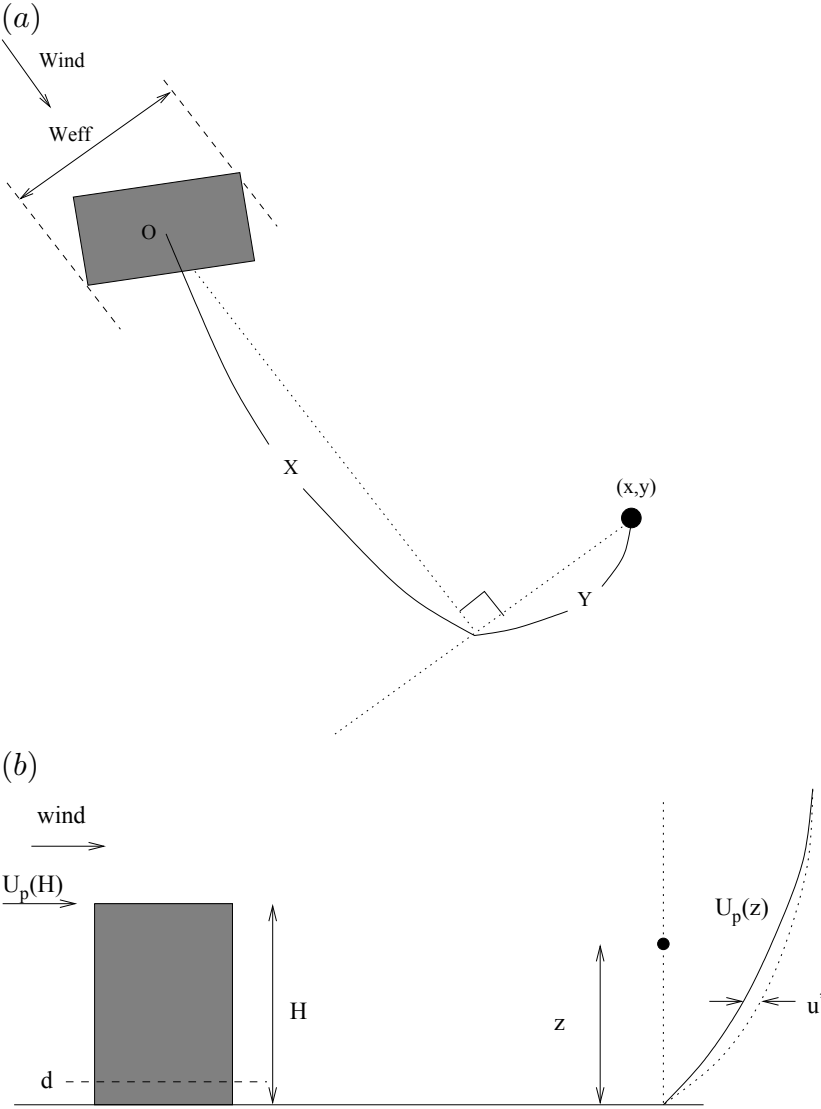


Figure 2.2: Plan (a) and side (b) views of the far-wake zone of a tall building (shaded block): plan (a) and side (b) views. Filled circle indicates the velocity evaluation point. O is the center of gravity of the building base.

and l_m is the vertical mixing length of the momentum, given by

$$\begin{cases} \frac{1}{l_m} = \frac{1}{\kappa z} + \frac{1}{\kappa(\overline{H}-d)} - \frac{1}{\kappa\overline{H}} & (z \leq \overline{H}), \\ l_m = \kappa(z-d) & (z > \overline{H}). \end{cases} \quad (2.28)$$

By this definition, l_m approaches the ground-based mixing length κz near the ground, and the canopy-based value $\kappa(z-d)$ above the canopy. The left-hand side of (2.26) represents vertical diffusion of the horizontal momentum, and the right-hand side the drag by the canopy. The equation (2.26) is solved numerically by the shooting method together with the 4th-order Runge–Kutta method for boundary conditions

$$U = 0 \quad \text{at} \quad z = z_{02}, \quad (2.29)$$

$$U = U_n(x, y, \overline{H}) \quad \text{at} \quad z = \overline{H}, \quad (2.30)$$

where z_{02} is the roughness length of open areas (see the next subsection).

(v) Above open areas

If wind moves out from an urban canopy to an open area, the speed increases because the surface friction decreases. We first consider a two-dimensional (2D) case depicted in Fig. 2.3 where the wind blows in the X direction, the roughness length changes from z_{01} to z_{02} at $X = 0$, and the zero-plane displacement from d to zero (negligible). The following procedure is due to Kaimal & Finnigan (1994). Upon change of roughness at $X = 0$, an internal boundary layer (IBL) that is in equilibrium with the new roughness starts to develop. Denoting the IBL thickness as δ_i and the friction velocity in IBL as u_{*2} , the growth of δ_i can be described by

$$\frac{d\delta_i}{dX} = \frac{B_1 u_{*2}}{\overline{U}}, \quad (2.31)$$

where $B_1 = 1.25$ is an empirical constant, and $\overline{U} = (u_{*2}/\kappa) \ln(\delta_i/z_{02})$ is the velocity at the top edge of IBL. For the initial condition $\delta_i(X = 0) = z_{02}$, the solution to (2.31) becomes

$$\frac{\delta_i}{X} \left(\ln \frac{\delta_i}{z_{02}} - 1 \right) = B_1 \kappa. \quad (2.32)$$

For non-negligible d , the initial condition $\delta_i(X = 0) = z_{02}$ is not strictly correct. However, in the current model where the immediate lee of the urban canopy is classified as the near-wake zone, which has higher priority than an open area, exact initial condition is not important. Hence, the condition $\delta_i(X = 0) = z_{02}$ is applied.

We assume that the vertical velocity profile above IBL obeys the same log law as in $X < 0$. Then, requiring continuity of wind speed across $z = \delta_i$, we find

$$u_{*2} = u_{*1} \frac{\ln \frac{\delta_i - d}{z_{01}}}{\ln \frac{\delta_i}{z_{02}}}. \quad (2.33)$$

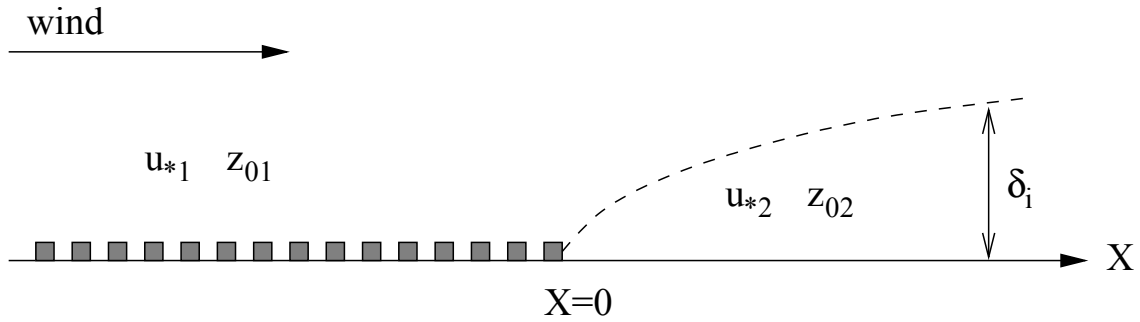


Figure 2.3: Side view of an open-area zone.

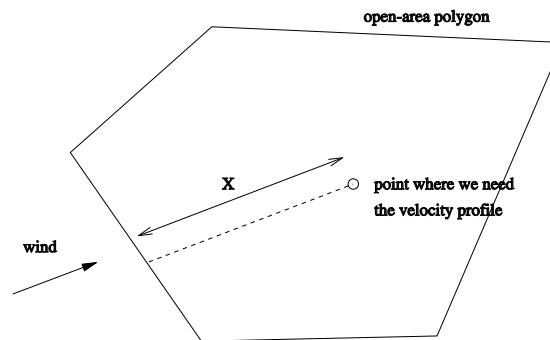


Figure 2.4: Three-dimensional open-area and the downwind distance X from the roughness change.

In reality, an open area has finite width in the direction normal to the plane of Fig. 2.3. For real finite open areas, we set the origin of X at the cross point between the area border and the wind-parallel line through the concerned point, and apply the 2D method described above.

(vi) Around elevated obstacles

In some urban areas, elevated highways run parallel to surface roads. Being the emission sources themselves, they have significant effect on the pollutant diffusion. Because they have much longer dimension in the road-parallel direction, we can treat them as 2D bodies. We first consider the case where the wind is normal to the infinite axis of a 2D body. Self-similar far-wake fields of 2D bodies were studied by many authors (*e.g.* Wygnanski *et al.* 1986), but the flow in the immediate neighborhood of 2D bodies have been revealed quantitatively only after the advent of the laser Doppler anemometry (LDA).

According to Lyn *et al.*'s (1995) wind-tunnel experiment with LDA, the flow around a square-section pillar can be divided into four zones: displacement, side-bubble, near-wake and far-wake zones. By the local coordinate systems

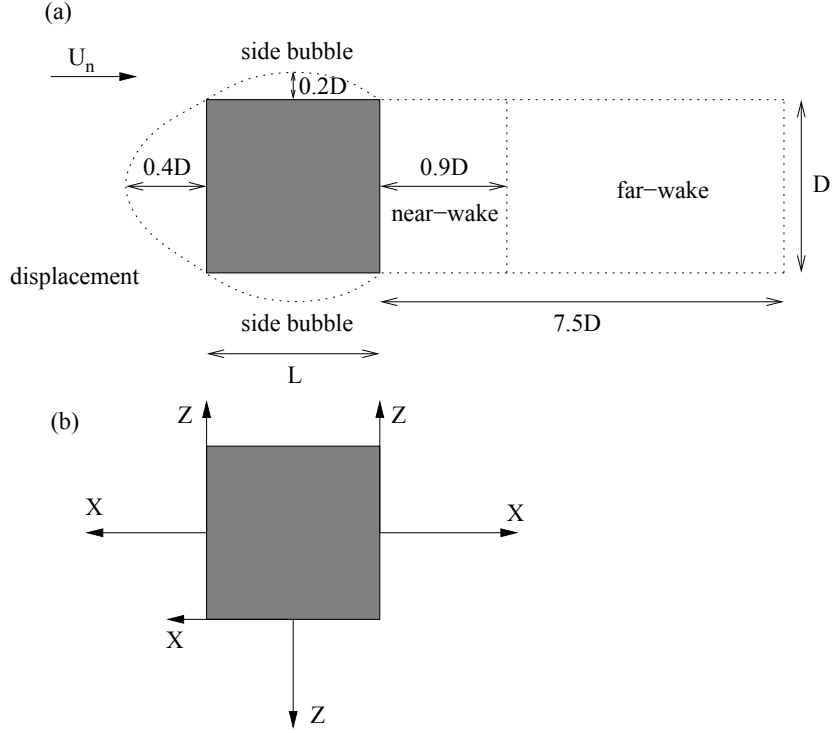


Figure 2.5: Zones around an elevated obstacle. (a) Zone definition, and (b) local coordinates.

defined in Fig. 2.5(b), the zone contours are given by

$$\text{displacement zone: } \frac{X^2}{(0.4D)^2} + \frac{Z^2}{(0.5D)^2} \leq 1, \quad X \geq 0, \quad (2.34)$$

$$\text{side-bubble zone: } \frac{X^2}{(L/2)^2} + \frac{Z^2}{(0.2D)^2} \leq 1, \quad Z \geq 0, \quad (2.35)$$

$$\text{near-wake, far-wake zones: } 0 \leq X \leq 0.9D, \quad 0.9D \leq X \leq 7.5D \quad |Z| \leq 0.5D, \quad (2.36)$$

where the windward pillar length L was equal to the crosswind width D in Lyn *et al.* (1995). The side-bubble zones on the top and the bottom surfaces of the 2D body are not considered in this model because the flow tends to reattach near the leading edge if the incident turbulence intensity is as high ($\gtrsim 20\%$) as in the urban boundary layer.

The initial velocity is specified as follows. In all zones, the velocity component parallel to the infinite axis is set equal to the ambient value $U_n(Z) \cos(\theta - \psi)$ where θ is the angle of the wind and ψ is the angle of the infinite axis of the 2D body. The component normal to the infinite axis is set zero in the displacement and side-bubble zones. In the near- and far-wake zones, based on the wind-tunnel results of Lyn *et al.* (1995), the value U_0 at the mid-height ($Z = 0$) of

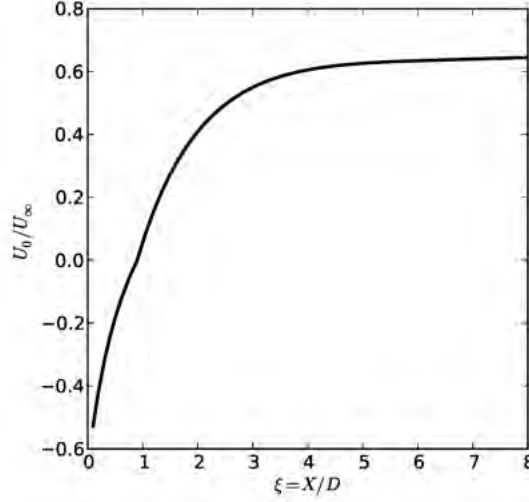


Figure 2.6: The centerline velocity (2.37) in the wake zone of an elevated obstacle.

the obstacle is specified by

$$\frac{U_0}{U_n(Z=0) \sin(\theta - \psi)} = \begin{cases} 1 - \sqrt{\frac{1.4}{\xi + 0.5}} & (\xi < 0.9), \\ 1 - \sqrt{\frac{1.4}{\xi + 0.5}} + \frac{1}{2}(\xi - 0.9) \exp\left(-\frac{\xi + 0.5}{2}\right) & (\xi \geq 0.9), \end{cases} \quad (2.37)$$

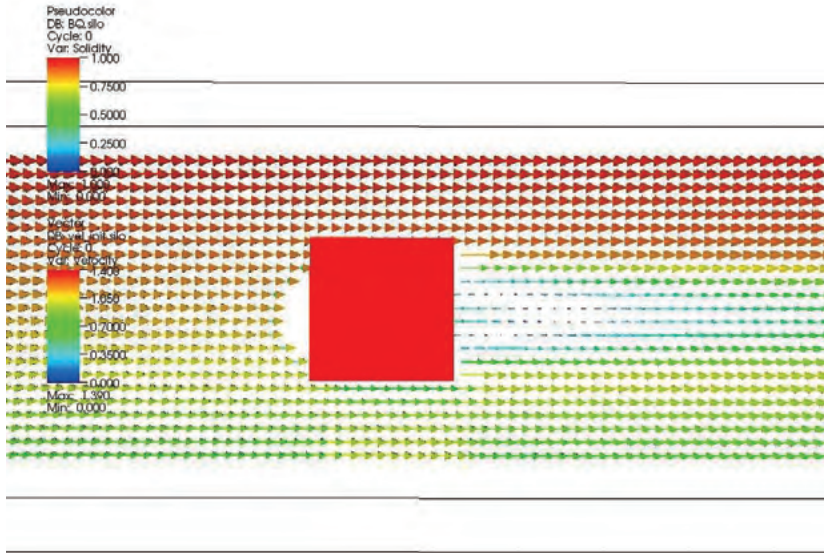
where $\xi = X/D$. Fig. 2.6 shows the dependence of U_0 on ξ . We observe that U_0 is opposite to the ambient wind for $\xi < 0.9$, and increases first rapidly and then gradually toward the ambient value $U_\infty = U_n(Z=0) \sin(\theta - \psi)$. Dependence on Z is given such that the wind speed changes smoothly to the ambient value:

$$\frac{U_X}{U_n(Z) \sin(\theta - \psi)} = 1 - \left(1 - \frac{U_0}{U_n(Z=0) \sin(\theta - \psi)}\right) \cos^2\left(\frac{\pi}{2} \frac{Z}{D/2}\right). \quad (2.38)$$

(vii) Around surface-mounted obstacles

As cited in Kaplan & Dinar (1996), Rockle (1990) considered displacement and near-wake zones on the upwind and downwind sides, respectively, of surface-mounted obstacles. We remark that these zones are called ‘cavity’ zones in Kaplan & Dinar (1996), but we use different notations to avoid confusion with the street-canyon flow that is traditionally called a cavity flow. There are alternative methods of dividing the space around obstacles (Robins *et al.* (2009)), but here we basically adopt Rockle’s method. The zones are shown schematically in Fig. 2.8. For a rectangular parallelepiped with dimensions shown in Fig. 2.8, the windward lengths L_F and L_R of the displacement and near-wake zones,

(a)



(b)

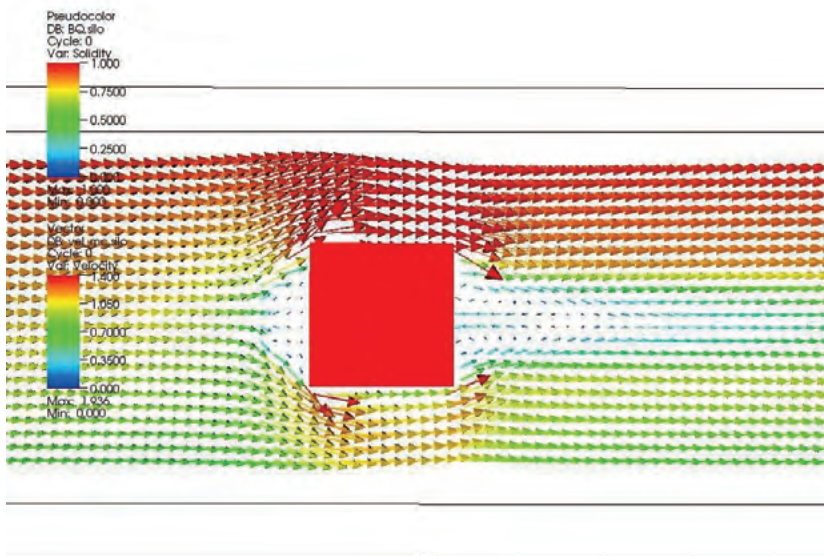


Figure 2.7: Initial (a) and mass-conserving (b) velocity fields around an elevated obstacle. Note that circulatory flow is produced in the lee of the obstacle. A power law profile $U = U_r(z/z_r)^{0.3}$ is specified for the ambient velocity: an option provided in MCAD for cases where there are few surface buildings in the domain but a measure of surface roughness needs to be assumed.

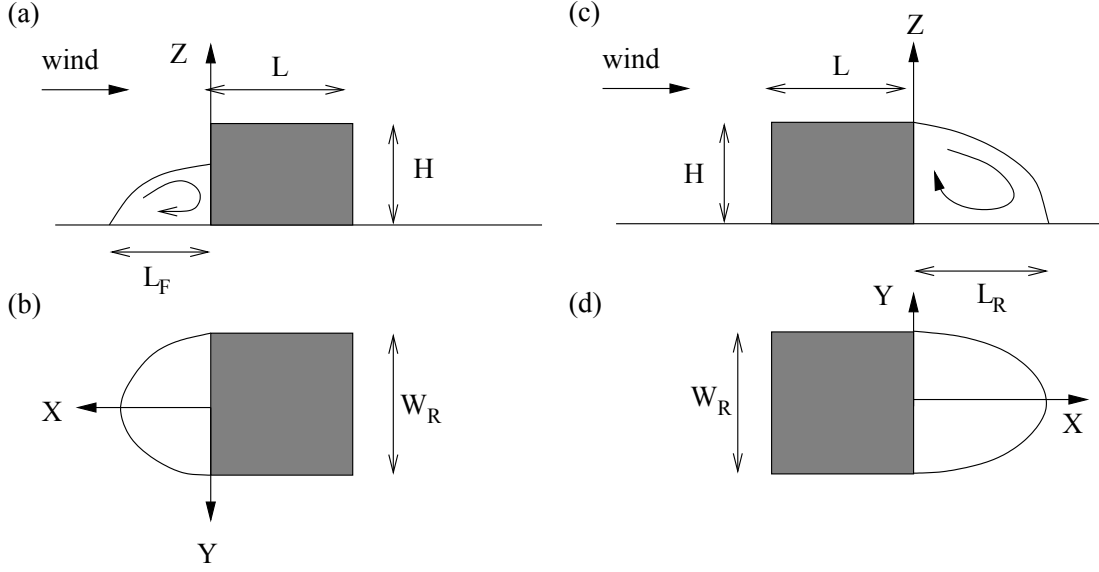


Figure 2.8: Zones around a surface-mounted obstacle: displacement zone (a: side view, b: plan view) and near-wake zone (c: side view, d: plan view).

respectively, are given by

$$L_F = \frac{2(W_R/H)}{1 + 0.8(W_R/H)}, \quad (2.39)$$

$$L_R = \frac{1.8W_R}{(L/H)^{0.3}(1 + 0.24W_R/H)} + \frac{L}{2}, \quad (2.40)$$

where L_F is due to Hosker (1984) and L_R to Fackrell & Pearce (1981). Then, the zones are defined as ellipsoids

$$\frac{X^2}{L_F^2 \left(1 - \left(\frac{Z}{0.6H}\right)^2\right)} + \frac{Y^2}{(W_R/2)^2} \leq 1, \quad X \geq 0, \quad Z \geq 0, \quad (2.41)$$

$$\frac{X^2}{L_R^2 (1 - (Z/H)^2)} + \frac{Y^2}{(W_R/2)^2} \leq 1, \quad X \geq 0, \quad Z \geq 0. \quad (2.42)$$

When the wind is oblique to the obstacle walls, a procedure similar to but a little modified from Kaplan & Dinar (1996) is applied. Displacement zone is defined on each of the two upwind walls with the zone length modified to

$$L'_F = L_F \sin^2(\phi - \theta), \quad (2.43)$$

where θ is the wind direction angle and ϕ is the angle of the wall vector defined in the direction looking the obstacle interior on the right-hand side (see Fig. 2.9).

In Kaplan & Dinar (1996), the effective width W_{eff} and length L_{eff} of the obstacle were defined by the projections of the building base perpendicular and

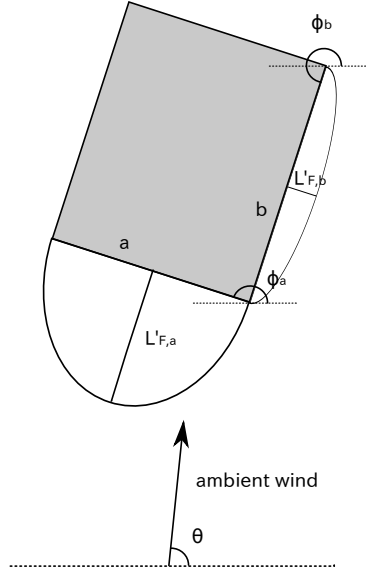


Figure 2.9: Displacement zones on two upwind walls a and b when the wind is oblique to the walls.

parallel, respectively, to the wind direction. W_{eff} and L_{eff} are then replaced with W_R and L , respectively, in equation (2.40) to obtain the base length L_R of the near-wake region. However, in Kaplan & Dinar (1996), the definition of the zone near the building base, where there can be regions close to the base but outside the near-wake zone, was left somewhat ambiguous. A clearer definition is proposed here. First, the definition of L_{eff} is modified. After W_{eff} is determined as a projection of the building base perpendicular to the wind direction (see Fig. 2.10), L_{eff} is defined by

$$L_{\text{eff}} = \frac{S_B}{W_{\text{eff}}}, \quad (2.44)$$

where S_B is the base area of the building. For an elongated thin building shown in Fig. 2.11, this definition is superior to wind-parallel projection because the latter definition results in oddly large L_{eff} . The shape of the base of the near-wake zone is specified as the minimum-area ellipse that passes the three solid-circled points (A,A',B) in Fig. 2.11 and has the center common with the building base. The minimum-area ellipse can be determined uniquely by standard numerical methods (Press *et al.* 2007).

The initial velocity field is specified in the same manner as in Kaplan & Dinar (1996). In the displacement zone, the velocity component parallel to the ambient wind is set zero, and that normal to the ambient wind has the same value as the ambient wind, *i.e.*

$$U_X = U_Z = 0, \quad U_Y = -U_n \cos(\theta - \phi). \quad (2.45)$$

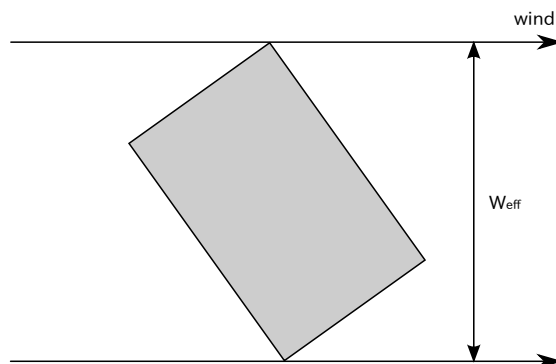


Figure 2.10: Effective width of a surface-mounted obstacle

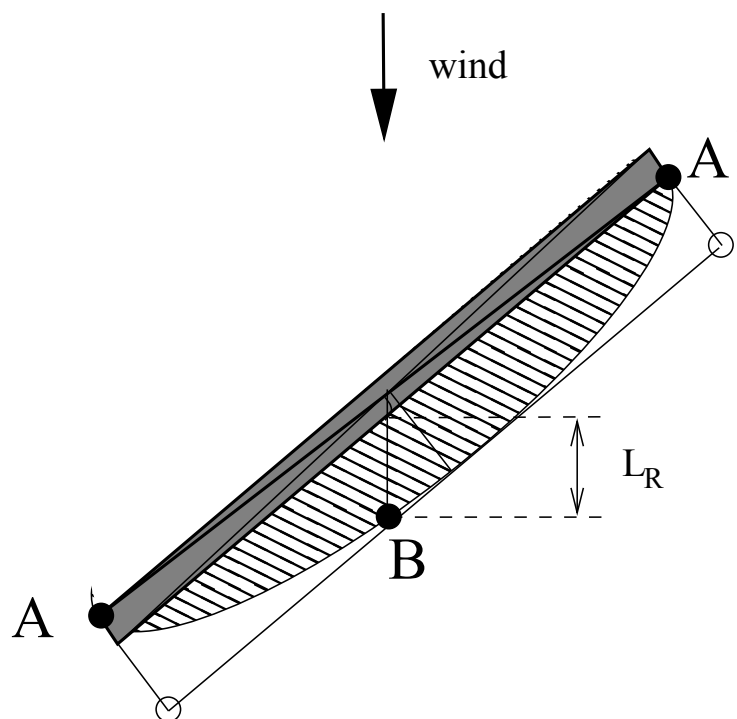


Figure 2.11: Near-wake zone of an elongated surface-mounted obstacle.

In the near-wake zone, the wind-parallel component is set as a reversed flow:

$$U_X = -U_n(Z = H) \left(1 - \frac{X}{d_N}\right)^2, \quad (2.46)$$

where

$$d_N = L_R \sqrt{\left(1 - \frac{Z^2}{H^2}\right) \left(1 - \left(\frac{Y}{W_R/2}\right)^2\right)}. \quad (2.47)$$

The other components are set as

$$U_Z = 0, \quad U_Y = -U_n \cos(\theta - \phi). \quad (2.48)$$

In Kaplan & Dinar (1996), ‘wake-zone’ was defined further downwind of the near-wake zone. Because, in the current model, this ‘wake-zone’ corresponds to the far-wake zone already treated in (iii), it is not considered here.

One may find the zero vertical velocity in equation (2.48) not representing the flow properly. In fact, vertical velocity component with appropriate sign and magnitude is induced after the MC calculation as demonstrated in Kaplan & Dinar (1996). Fig. 2.12 shows an example of initial and mass-conserving velocity fields in the near-wake and the displacement zones of a surface-mounted parallelepiped. In future, when the velocity field in the zones around obstacles is organized into more comprehensive formulas, we will specify more appropriate initial velocity field.

(viii) Street canyon

A street canyon is the region made by two facing buildings. The shape of the region depends on the wind direction relative to the buildings. The proposed model basically follows the procedure of Kaplan & Dinar (1996) except for modification for asymmetric street canyons.

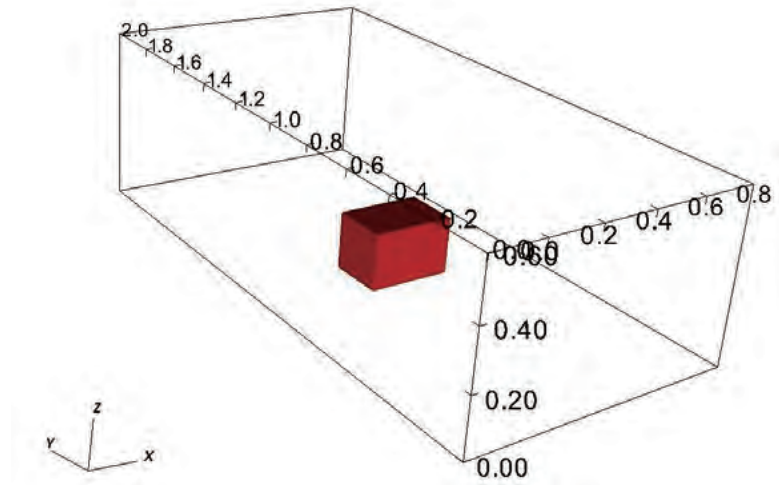
For a simple configuration shown in Fig. 2.13, the flow can be classified into isolated, wake-interference, and skimming-flow regimes depending on the aspect ratios (Fig. 2.14). MCAD specifies a particular velocity field if the flow is in the skimming-flow regime where there is a distinct standing eddy inside the street canyon. The skimming-flow regime occurs if the following relationship is satisfied.

$$\frac{W_c}{H_c} < \begin{cases} 1.25 + 0.15 \frac{L_c}{H_c} & \frac{L_c}{H_c} < 2 \\ 1.55 & \frac{L_c}{H_c} \geq 2, \end{cases} \quad (2.49)$$

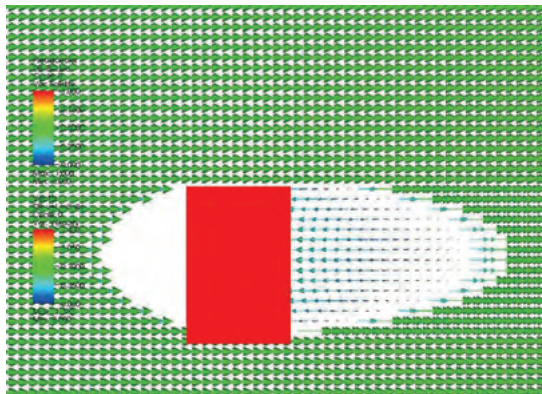
where H_c is the canyon height, L_c the canyon length and W_c the canyon width. Wind-tunnel experiments by Uehara *et al.* (2001) suggest that the height H_c be defined by

$$H_c = \begin{cases} \frac{1}{2} (H_1 + H_2) & (H_1 \leq H_2) \\ H_1 & (H_1 > H_2), \end{cases} \quad (2.50)$$

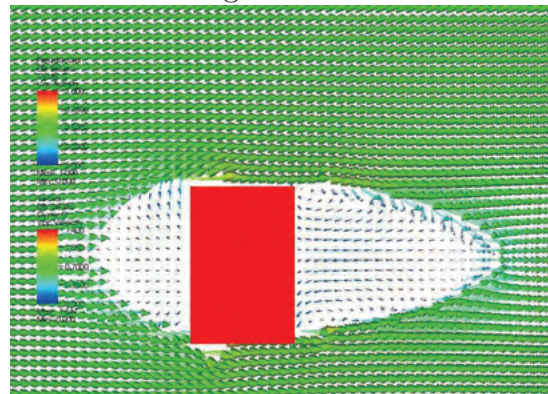
where H_1 and H_2 are the heights of upwind and downwind buildings, respectively. We define a street-canyon zone when the flow is in the skimming-flow regime.



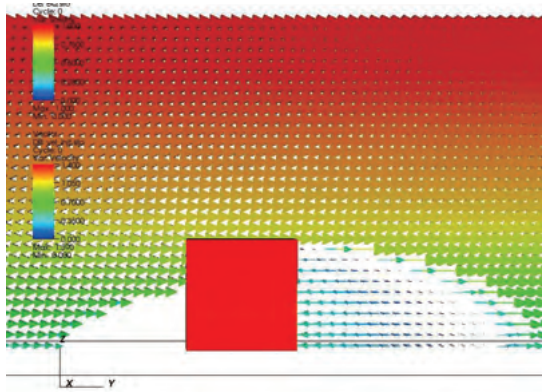
Initial at $z = 0.05$



Mass-conserving at $z = 0.05$



Initial at $x = 0.5$



Mass-conserving at $x = 0.5$

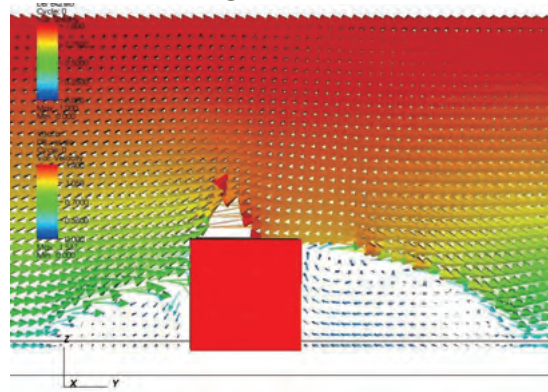


Figure 2.12: Sections of the velocity fields before and after applying the MC calculation.

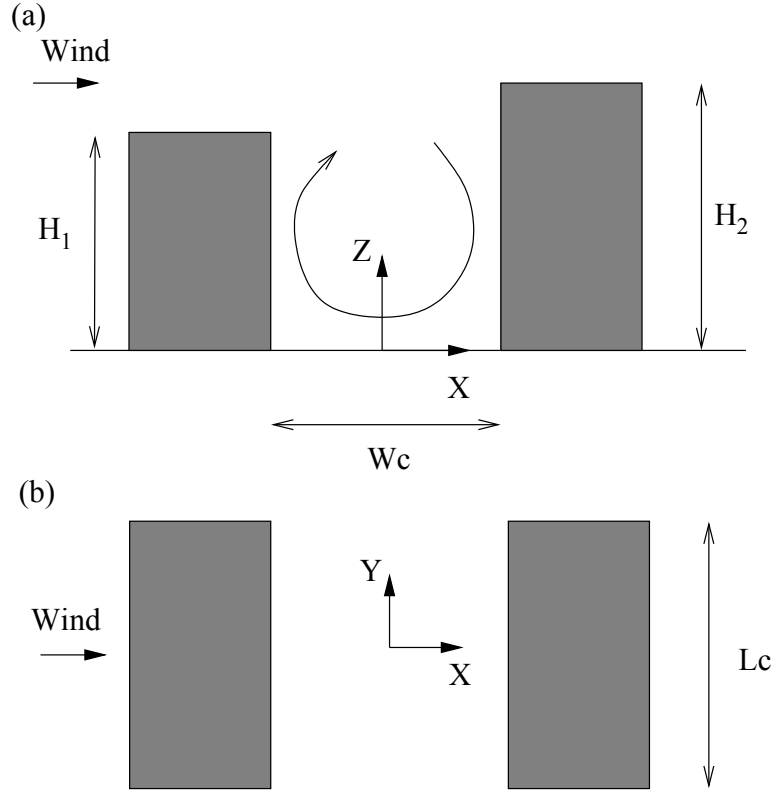


Figure 2.13: Step-up street canyon: side (a) and plan (b) views.

For general building configurations, the street canyon is formed by parts of the walls that face each other with respect to the wind direction (see Fig. 2.15).

If $H_1 \leq H_2$, or the canyon is of step-up type, the street-canyon flow in $Z \leq H_c$ can be approximated by the Hotchkiss–Harlow equations (Hotchkiss & Harlow 1973):

$$\begin{aligned}
 U_X/U_H &= (1 - \beta)^{-1} [\gamma(1 + k\zeta) - \beta(1 - k\zeta)/\gamma] \cos kX, \\
 U_Z/U_H &= k\zeta(1 - \beta)^{-1} [\gamma - \beta/\gamma] \sin kX, \quad (2.51) \\
 k &= \pi/W_c, \quad \beta = \exp(-2kH_c), \quad \gamma = \exp(k\zeta), \quad \zeta = Z - H_c,
 \end{aligned}$$

where U_X is the cross-canyon and U_Z is the vertical velocity component, and $U_H = U_n(z = H_c)$. The component U_Y has the same value as the ambient flow.

For $H_1 > H_2$ and $L_c = W_c = H_1$, Uehara *et al.* (2001) shows that the flow is considerably different from the vortical motion represented by (2.51) but is dominated by nearly uni-directional flow from the downwind to the upwind wall. Their wind-tunnel measurement can be approximated by

$$\begin{aligned}
 \frac{U_X}{U_H} &= -0.4\alpha_c^{0.5} \left(1 - \frac{Z}{H_c}\right) \frac{4\left(\frac{Z}{H_c} + 0.8\alpha_c\right)}{(1 + 0.8\alpha_c)^2} \cos\left(\pi \frac{X}{W_c}\right), \\
 \frac{U_Z}{U_H} &= \frac{0.2}{0.72}\alpha_c^{0.15} \frac{Z}{H_c} \left(1.4 - \frac{Z}{H_c}\right) \cos\left(\pi \frac{X}{W_c}\right), \quad (2.52)
 \end{aligned}$$

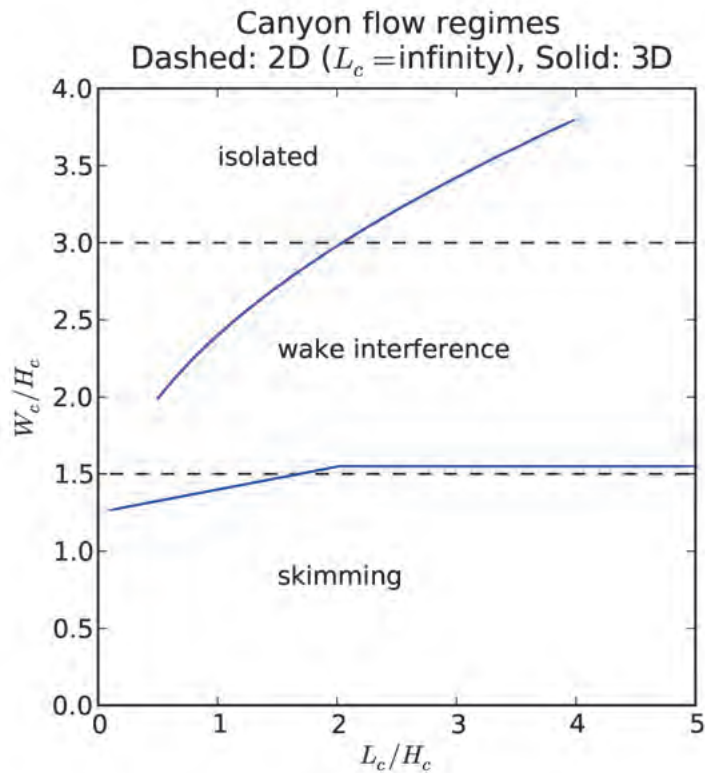


Figure 2.14: Dependence of the flow regimes on the building geometry. H_c : height of the facing buildings, W_c : separation between the buildings, L_c : length along the street axis. It is assumed that the wind is normal to the street axis, buildings have the same height, and the facing walls of the buildings have the same area. 2D case is from Oke (1987) cited by Harman *et al.* (2004) and 3D case is from Oke (1988) cited by Kaplan & Dinar (1996).

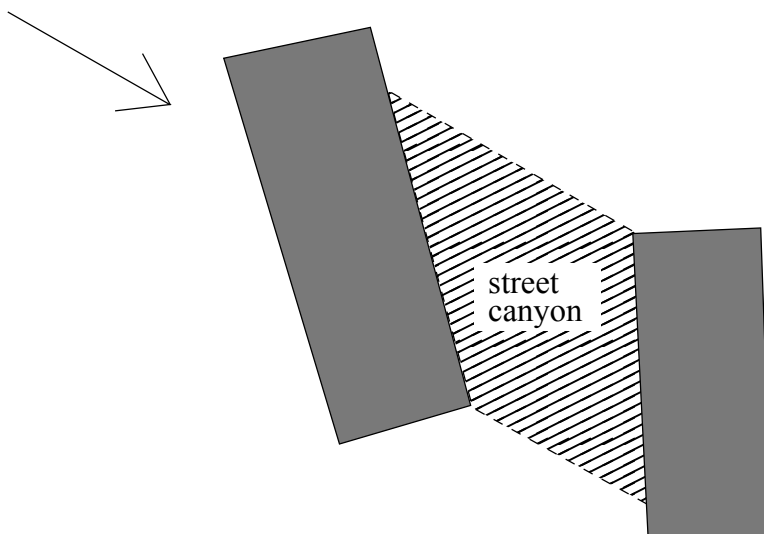


Figure 2.15: Plan view of a street-canyon zone when the wind and buildings are not aligned.

where $\alpha_c = (H_0 - H_1)/W_c$. Because our model is intended to be used mostly for Japanese urban areas where relatively narrow street canyons ($L_c \sim W_c$) are norm, we adopt (2.52) for $H_1 > H_2$ for any values of L_c and W_c satisfying the street-canyon criterion (2.49). For street canyons with $L_c \gg W_c$ as often found in European cities, different specification methods should be employed.

Fig. 2.16 shows an example of an even canyon ($H_1 = H_2$). We observe that the initial and the mass-conserving velocity fields are not much different because the Hotchkiss–Harlow formula (2.51) satisfy the mass-conserving equation $\partial U_X/\partial X + \partial U_Y/\partial Y = 0$. Fig. 2.17 shows the case with a step-down canyon ($H_1 > H_2$). We observe significant modification of the velocity field due to the MC procedure. This large difference occurs because equation (2.52) is not mass-conserving and is an approximation only to the centerline ($Y = 0$) velocity field. A more comprehensive formulation would be necessary to improve the model performance.

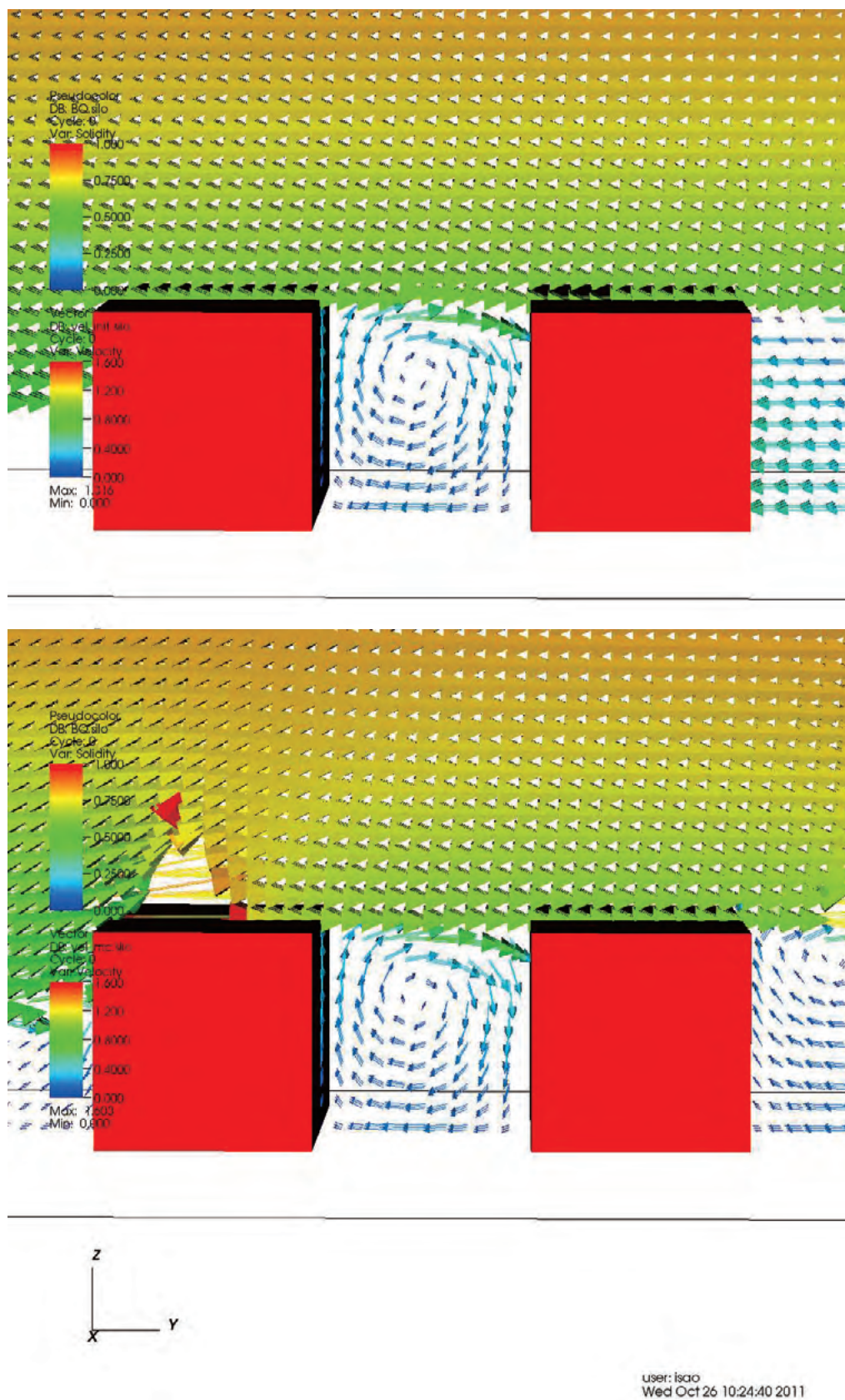


Figure 2.16: Initial (a) and mass-conserving (b) velocity fields for an even street canyon.

2.3 AD method

The concentration field C is calculated by solving the AD equation

$$\frac{\partial C}{\partial t} + \mathbf{U} \cdot \nabla C = \nabla \cdot (\mathbf{K} : \nabla C) + q, \quad (2.53)$$

where \mathbf{U} is the mass-conserving velocity field obtained by the MC method, $\mathbf{K} = (K_x, K_y, K_z)$ is the eddy diffusivity, and q is the rate of emission. The term involving C on the right-hand side of (2.53) is expanded as

$$\nabla \cdot (\mathbf{K} : \nabla C) = \frac{\partial}{\partial x} \left(K_x \frac{\partial C}{\partial x} \right) + \frac{\partial}{\partial y} \left(K_y \frac{\partial C}{\partial y} \right) + \frac{\partial}{\partial z} \left(K_z \frac{\partial C}{\partial z} \right). \quad (2.54)$$

The equation (2.53) is proceeded in time until C reaches a sufficiently steady state. The steady problem without the term $\partial C / \partial t$ could be treated directly, but as mentioned in Hoffman (1992) (p514) and experienced by ourselves, the stability of available numerical methods is too poor to be used in a model intended for arbitrary geometries. The boundary condition is

$$C = 0 \quad \text{on upwind domain boundaries,} \quad (2.55)$$

$$\partial C / \partial n = 0 \quad \text{on other boundaries and on solid walls.} \quad (2.56)$$

In practice, the point where the concentration is needed can fall inside solid cells intentionally if the point coordinates are given at the residential address, or unintentionally due to positioning errors of the point itself or the obstacle shape. In such a case, the solution to (2.53) gives $C = 0$. To avoid such an undesirable result, MCAD employs harmonic interpolation inside obstacles, *i.e.*

$$\nabla^2 C = 0 \quad (2.57)$$

is solved inside each obstacle with the solution of (2.53) as the boundary condition on the obstacle walls. Equation (2.57) also represent diffusion without advection and emission source, which is the case inside buildings. This procedure is effective when there are tens of thousands of sample points as is the case with large-scale epidemiological studies, and manual adjustment of these points is not feasible.

In Kaplan & Dinar (1996), C was calculated by LSM because it assures high accuracy near emission sources. The choice of AD in MCAD is motivated by the following considerations:

- AD is numerically far less costly than LSM.
- AD is relatively insensitive whereas LSM is sensitive to the grid resolution. When the objective is moderate accuracy at low numerical cost, lower grid resolution is preferred.
- In complex geometries with distributed emission sources, the number of fluid particles that need to be discharged in LSM becomes prohibitively large in order to make sure that the particles reach all the possible spaces between buildings.

LSM has, of course, important advantages over AD, *e.g.* accuracy near emission sources, back-tracing capability, and straight-forward extension to problems involving chemical reactions, but in the foreseeable future where air pollution will need urgent remedy, there is a strong need for numerically light models even without these attractive features.

The eddy diffusivity \mathbf{K} is specified as follows. In the ambient and the open-area zones where direct effect of individual buildings is negligible, the horizontal components (K_x, K_y) are derived from the velocity fluctuation spectra using the classical diffusion theory and the vertical component K_z by the mixing-length theory. In other zones, \mathbf{K} is given in a rather crude manner as proportional to a relevant length scale times a velocity scale with the proportionality constant being a free adjustable parameter.

(i) Ambient and (ii) in-between tall buildings

In this subsection, the wind is assumed in the x direction for simplicity.

In the horizontal direction, we may assume that the turbulent velocity field is homogeneous at each height. Hence, using the classical diffusion theory by Taylor (1921) and Ogura (1957), the diffusivity can be written as

$$K_{x,y}(t) = \frac{z}{U_n} \int_0^\infty S_{u,v}^L(f) \frac{\sin 2\pi f \hat{t}}{2\pi f} \left\{ 1 - \frac{\sin^2 \pi f \hat{T}_A}{(\pi f \hat{T}_A)^2} \right\} df, \quad (2.58)$$

where $S_u^L(f)$ and $S_v^L(f)$ are the Lagrangian spectra (defined in $f > 0$) of the velocity fluctuations in the x and y directions, respectively, $f = nz/U_n$ is the non-dimensional frequency, n is the dimensional frequency, and the dimensional flight time t and the observation duration T_A are non-dimensionalized by

$$\frac{t}{\hat{t}} = \frac{T_A}{\hat{T}_A} = \frac{z}{U_n}. \quad (2.59)$$

Although Ogura's formula (2.58) has later been revised by Eckman (1994) whose formula involves both the Eulerian and the Lagrangian spectra, the difference between Ogura's and Eckman's formulas is insignificant for relatively large T_A in typical cases (one hour for outdoor measurement and virtually infinity for wind-tunnel measurement). Because Ogura's linear formula is suited for decomposing $S_{u,v}^L(f)$ into different frequency ranges and, for example, replacing high-frequency component with building-generated turbulence contribution, we adopt it for the current model. Frequency decomposition of the spectra will be discussed in §4.

Note that, in (2.58), $K_{x,y}$ are defined as a function of the flight time t . Conversion to functions of the downwind distance d_s from the emission source is done by

$$t = \frac{d_s}{\frac{1}{z-z_s} \int_{z_s}^z U_n dz}, \quad (2.60)$$

where z_s is the height of the emission source. Because d_s depends on the source position (x_s, y_s, z_s) and the concerned point (x, y, z) , $K_{x,y}$ are functions of

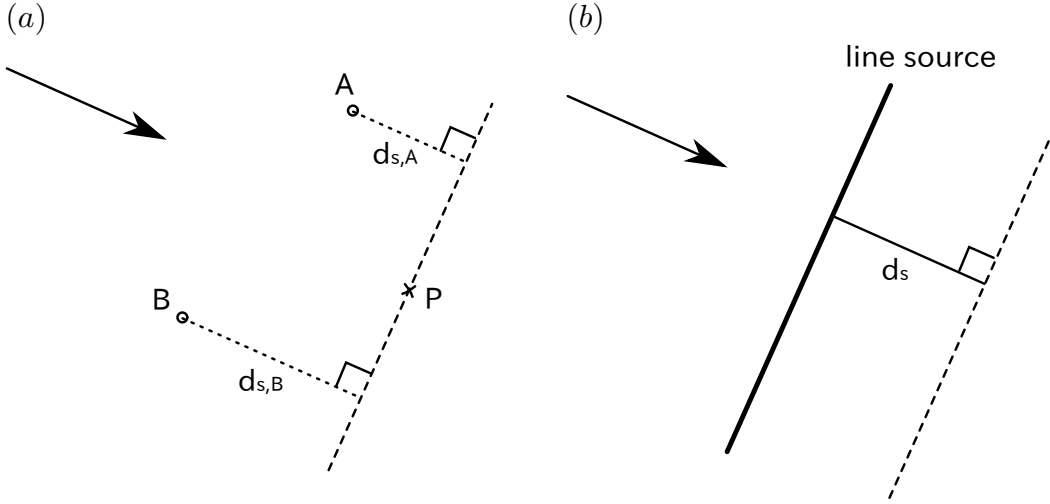


Figure 2.18: Downwind distance d_s from sources. In (a), downwind distances to the target point P are shown for two sources A and B. At a given point, the downwind distances $d_{s,A}$ and $d_{s,B}$ are different in general. In (b), the downwind distance d_s from the line source is uniquely determined at given locations.

both (x_x, y_s, z_s) and (x, y, z) . Hence, if there are multiple sources, $K_{x,y}$ takes different values for different sources, implying that the AD equation must be solved for individual sources and the concentration field be obtained as a sum of individual results. Fig. 2.18(a) illustrates different downwind distances to the target point P from two point sources A and B. For a straight 2D line source, because d_s takes the same value along lines parallel to the line source, the values of K_x and K_y can be calculated uniquely in space, and the AD equation is solved just once. Fig. 2.18(b) shows a line (dotted) which has downwind distance d_s from a line source (bold solid). This d_s is the only downwind distance that the points on the dotted line have.

Because the Lagrangian spectra $S_{u,v}^L$ in (2.58) are of the fluctuation following fluid particles, they are difficult to be measured and there has not been sufficiently many observations for reliable universal formulas to be established. On the other hand, the Eulerian spectra $S_{u,v}^E$ based on the fluctuation at a fixed point are easier to measure and there are reliable universal formulas. To convert from Eulerian to Lagrangian spectra, we adopt an empirical method by Hay & Pasquill (1959) and Hanna (1981b), *i.e.*

$$S_{u,v}^L(f) = \beta S_{u,v}^E(\beta f), \quad (2.61)$$

where $\beta = \gamma U_n / \sigma_{u,v}$ and $\sigma_{u,v}$ are the standard deviations of the velocity fluctuations given by

$$\sigma_{u,v} = \int_0^\infty S_{u,v}^E(f) \left\{ 1 - \frac{\sin^2 \pi f \hat{T}_A}{(\pi f \hat{T}_A)^2} \right\} df. \quad (2.62)$$

For the constant γ , we use 0.55 proposed by Degrazia & Anfossi (1998). Note that (2.61) is valid in relatively high f , or in the inertial sub-range of turbulence.

A well-established set of the Eulerian spectral formulas is the Kaimal spectra (Kaimal & Finnigan 1994)

$$S_u^E(f) = \frac{102u_*^2}{(1 + 33f)^{5/3}}, \quad (2.63)$$

$$S_v^E(f) = \frac{17u_*^2}{(1 + 9.5f)^{5/3}}. \quad (2.64)$$

These formulas were established based on observations over relatively smooth flat terrain, but by replacing u_*^2 with the local momentum flux $-\overline{uw}$, they are found to agree fairly well with observations above urban area (Al-Jiboori *et al.* 2002). In MCAD, we neglect the vertical variation of $-\overline{uw}$ and use u_*^2 for any terrain. The spectra (2.63)(2.64) are valid for fluctuations of timescales less than a few minutes. Particularly, the crosswind component S_v needs to be modified for outdoor long-time averages where low-frequency meandering makes a substantial contribution, or for wind-tunnel experiments where, on the contrary, the low-frequency fluctuations are suppressed due to the finite width of the test section.

In the vertical direction, K_z is given by the mixing-length theory, *i.e.*

$$K_z = \frac{1}{Sc_t} l_m^2 \frac{\partial U_n}{\partial z} = \frac{1}{Sc_t} \kappa u_* (z - d), \quad (2.65)$$

where $l_m = \kappa(z - d)$ is the mixing length above urban canopy and $Sc_t = 0.7$ is the turbulent Schmidt number (Robins 1978). Near the emission source, (2.65) needs to be modified (Reid 1979). At sufficiently downwind point from the source, K_z can be written as

$$K_z = \sigma_w^2 T_L, \quad (2.66)$$

where σ_w is the standard deviation of vertical velocity fluctuation and T_L is some timescale. In homogeneous turbulence, T_L is equal to the Lagrangian timescale, but in the inhomogeneous case of turbulence near the ground, T_L is different from the Lagrangian timescale. Comparing (2.65) and (2.66), we find

$$T_L = \frac{\kappa u_* (z - d)}{\sigma_w^2 Sc_t}. \quad (2.67)$$

Assuming that the Lagrangian correlation function is $\exp(-t/T_L)$, the theory for homogeneous turbulence leads to

$$K_z = \sigma_w^2 T_L \left\{ 1 - \exp\left(-\frac{t}{T_L}\right) \right\}. \quad (2.68)$$

Hence, K_z tends to $\sigma_w^2 t$ near the emission source, which is the correct behavior not represented by the time-independent (2.65). Regarding (2.68) as an interpolation formula between the near-source $K_z \sim \sigma_w^2 t$ and the far-downwind $K_z \sim \sigma_w^2 T_L$, we adopt it for inhomogeneous turbulence near the ground.

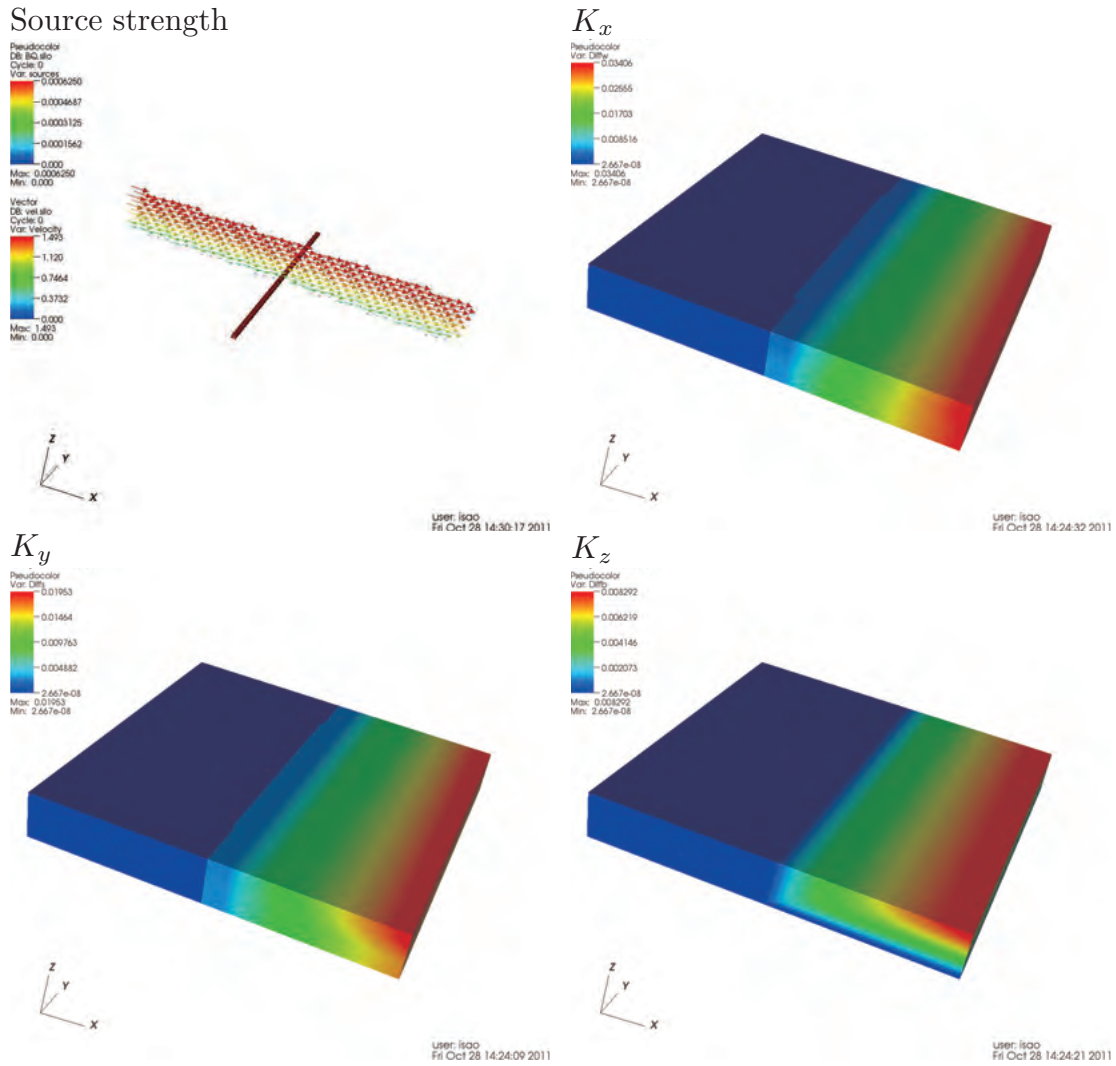


Figure 2.19: Distributions of eddy diffusivity K_x , K_y , and K_z for a line source.

For σ_w , we use the same formula as in ADMS (CERC 2007)

$$\sigma_w = 1.3u_* \left(1 - 0.8 \frac{z}{h}\right), \quad (2.69)$$

where h is the boundary-layer thickness. For outdoor diffusion, we set $h = 600$ m as a typical value in neutral atmosphere, and for wind-tunnel diffusion, h takes the value determined by measuring the vertical velocity profile.

Fig. 2.19 shows the distributions of K_x , K_y , and K_z downwind of a line source. We observe that K_z exhibit clear dependence on both x (downwind direction) and z , where as K_x and K_y are relatively insensitive to z . Note that the region where K_y begins to depend on z corresponds to the point where the integral (2.58) begins to saturate.

(iii) Far-wake of tall buildings

In this zone, the characteristic velocity and length are the velocity defect u' and the effective building width W_{eff} , respectively. We assume that the far-wake

turbulence adds eddy diffusivity to the ambient value. Assuming that all the components have equal values, the additional eddy diffusivity \mathbf{K}' due to the i 'th tall building can be written as

$$K'_x = K'_y = K'_z = A_{\text{far-wake}} W_{\text{eff},i} u'_i, \quad (2.70)$$

where $A_{\text{far-wake}}$ is a model parameter. When there are multiple tall buildings, the characteristic velocity is the sum $\sum_i u'_i$ and the length scale should be $\max\{W_{\text{eff},i}\}$ because, in turbulent diffusion for practical averaging periods which are sufficiently longer than the turnover time of the eddies of size $\max\{W_{\text{eff},i}\}$, the major contribution to diffusion is that by such large eddies. Hence, \mathbf{K}' becomes

$$K'_x = K'_y = K'_z = A_{\text{far-wake}} \max\{W_{\text{eff},i}\} \sum_i u'_i. \quad (2.71)$$

Fig. 2.20 shows a distribution of K'_y downwind of a tall building among an array of lower buildings. The spread of the far-wake zone is clearly observed here.

(iv) Urban canopy

In the horizontal direction, the relevant length scale is the mean building width L and the velocity scale is the wind speed $U_n(z)$ at each height. Therefore, we have

$$K_x = K_y = A_{\text{canopy}} L U_n(z). \quad (2.72)$$

In the vertical direction, we set

$$K_z = \frac{1}{Sc_{t,\text{canopy}}} \{\kappa(\bar{H} - d)\}^2 \frac{U_n(\bar{H})}{\bar{H}}. \quad (2.73)$$

Although the mixing-length theory implies

$$K_z = \frac{1}{Sc_{t,\text{canopy}}} l_m^2 \frac{\partial U_n}{\partial z}, \quad (2.74)$$

where l_m is given by (2.28), the behavior $l_m \sim \kappa z$ near the ground results in mathematically singular behavior. Hence, assuming that the largest eddies make a major contribution, equation (2.73) is adopted instead.

(v) Above open areas

In the IBL over open areas, \mathbf{K} is obtained by replacing u_* with u_{*2} in (2.63) (2.64) and (2.68)(2.67) for the ambient zone.

(vi) Around elevated obstacles

In all the zones (near-wake, displacement, side-bubble and far-wake), the relevant length is the vertical width D of the obstacle. The relevant velocity in the near-wake, displacement and side-bubble zones is the ambient velocity at the mid-height z_m of the obstacle. In the far-wake zone, similarly to the far-wake zone of tall buildings, the relevant velocity is the difference between the velocity specified by (2.37) and the ambient velocity at $z = z_m$, and the

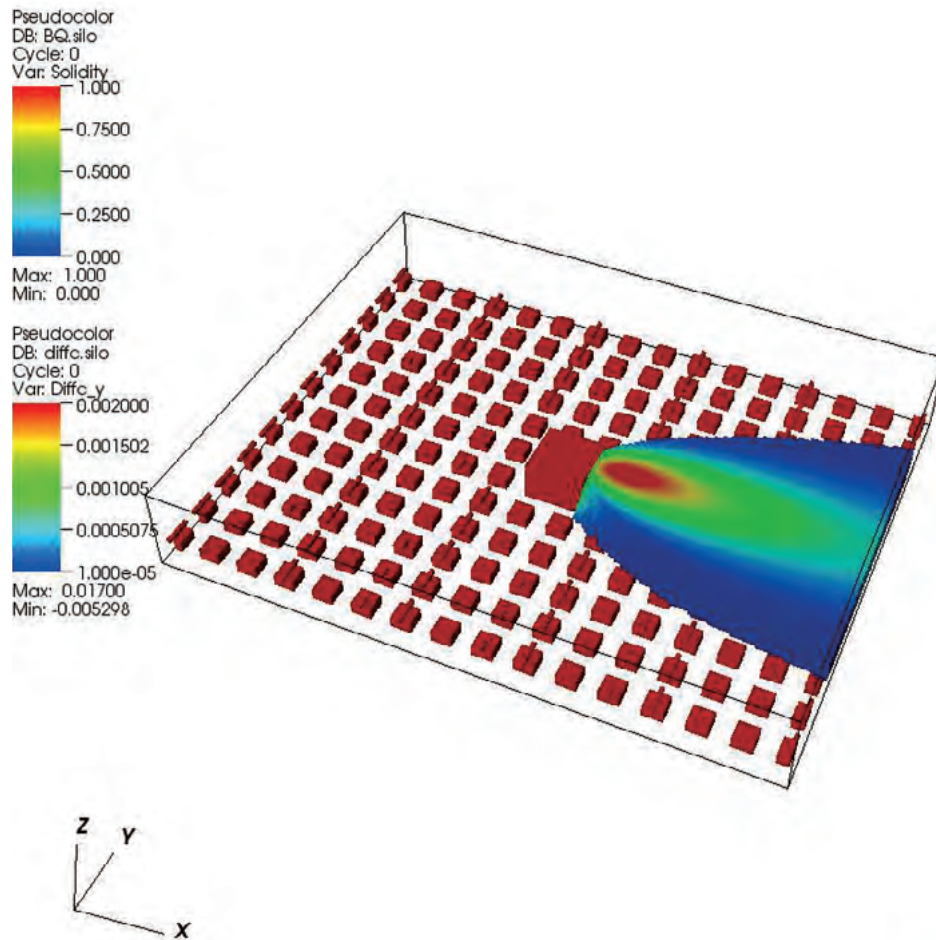


Figure 2.20: Additional eddy diffusivity K'_y downwind of a tall building. The diffusivity field is sliced at the height of the tall building.

eddy diffusivity \mathbf{K}' is added to the ambient value. Therefore, assuming all the components have equal values in all the zones, which is not strictly correct but is sufficient in the current crude modeling, the eddy diffusivity becomes

$$\begin{aligned} \text{Near-wake zone} & \quad K_x = K_y = K_z = A_{\text{near-wake}} DU_n(z_m) \\ \text{Displacement zone} & \quad K_x = K_y = K_z = A_{\text{displacement}} DU_n(z_m) \\ \text{Far-wake zone} & \quad K'_x = K'_y = K'_z = A_{\text{far-wake}} D(U_n(z_m) - U_0) \end{aligned}$$

where U_0 is given by (2.37).

(vii) Around surface-mounted obstacles

In addition to the near-wake and displacement zones for MC calculation, we consider wake-diffusion zone immediately outside the near-wake zone. As described in Leuzzi & Monti (1998), turbulent intensity is considerably higher in the wake-diffusion zone than in the ambient.

In the near-wake zone, tracer-particle visualization reveals sporadic rapid flow toward the leeside wall, which is considered to make significant contribution to diffusion. Hence, the relevant length scale is the mean horizontal dimension $\sqrt{L_R W_{\text{eff}}}$ of the near-wake zone, and the relevant velocity is the reverse flow speed U_X given by (2.46). Assuming all the components have equal values, we set

$$K_x = K_y = K_z = A_{\text{near-wake}} \sqrt{L_R W_{\text{eff}}} |U_X|. \quad (2.75)$$

In the displacement zone, the dominant motion is the vertical eddy depicted in Fig. 2.8(a). Hence, the relevant length is the mean vertical dimension $\sqrt{0.6HL'_F}$ of the zone, where L'_F is given by (2.39) and (2.43). Because the eddy strength is determined by the velocity at $z = 0.6H$, the relevant velocity is $U_n(0.6H)$. Again, assuming isotropy, we set

$$K_x = K_y = K_z = A_{\text{displacement}} \sqrt{0.6HL'_F} U_n(0.6H). \quad (2.76)$$

For the wake-diffusion zone, we first define the zone shape (see Fig. 2.22). The inner boundary of the zone is the outer boundary of the near-wake zone given by (2.42). The outer boundary of the wake-diffusion zone is specified by

$$\frac{X_m^2}{a^2 \left(1 - \frac{Z^2}{c^2}\right)} + \frac{Y^2}{b^2} \leq 1, \quad Z > 0, \quad X_m > 0, \quad (2.77)$$

where X_m is the downwind distance from the center of area of the horizontal section of the obstacle, and the ellipsoid dimensions are given by

$$a = \frac{1}{2} L_{\text{eff}} + 1.5 L_R, \quad (2.78)$$

$$b = \frac{1}{2} W_{\text{eff}} + 0.2 L_{\text{eff}}, \quad (2.79)$$

$$c = H + 0.2 L_{\text{eff}}. \quad (2.80)$$

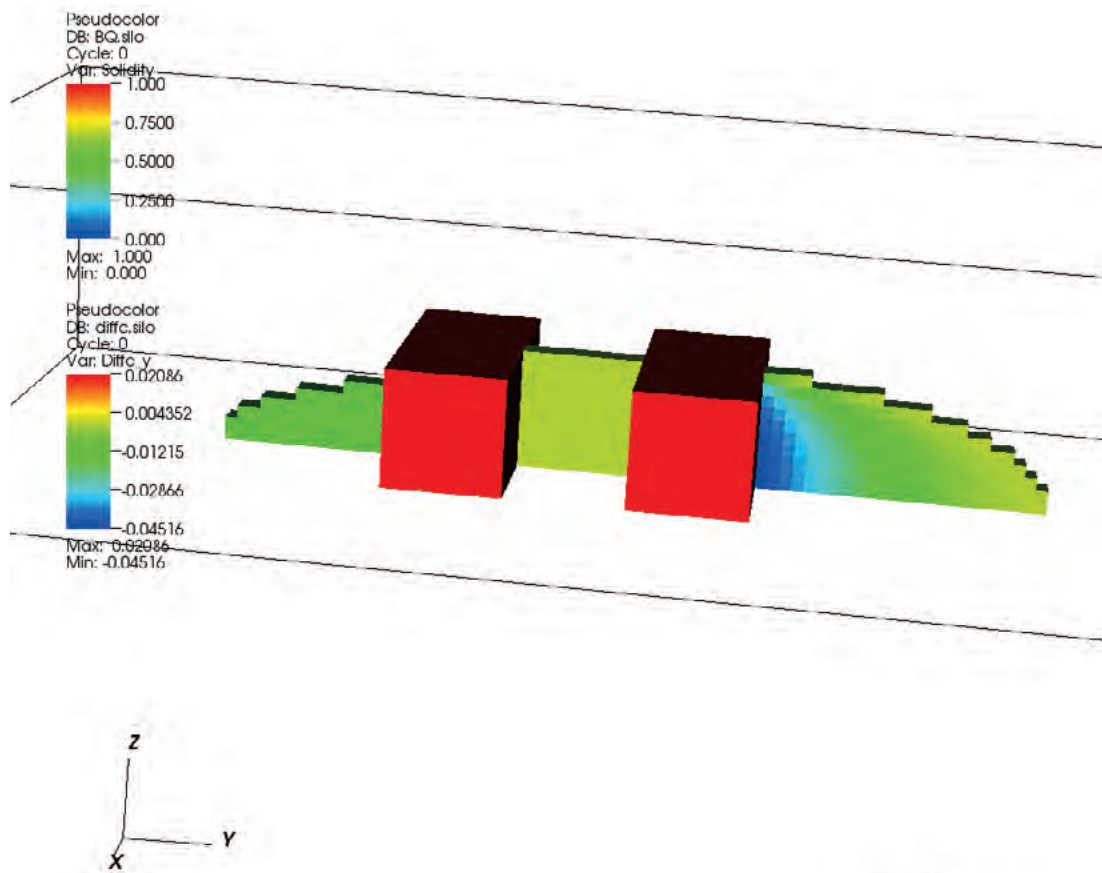


Figure 2.21: Distribution of K_y in the displacement and the near-wake zones of canyon-forming buildings. A slice at the middle of the building width is shown.

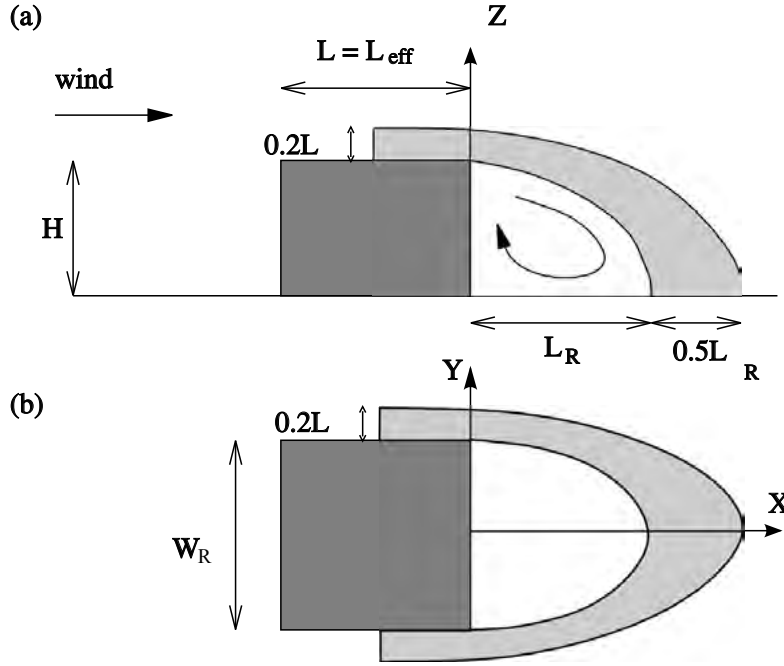


Figure 2.22: Wake-diffusion zone of a surface-mounted obstacle: side (a) and (b) plan views. The region immediately outside of the near-wake zone is the wake-diffusion zone.

The coefficients 1.5 and 0.2 in the above equations are determined subjectively from the results of turbulence intensity measurement (Snyder & Lawson 1993) described in Leuzzi & Monti (1998).

The wake-diffusion zone is introduced because the measurement result of Snyder & Lawson (1993) clearly shows regions of substantially high turbulence intensity outside the near-wake zone defined in our model. Considering the approximate nature of the model, the wake-diffusion zone may not be necessary, but the zone is defined here anticipating future development.

The relevant length is the zone thickness $0.2L_{\text{eff}}$ and the relevant velocity is $U_n(z)$ at each height. The turbulence in the zone is considered to add eddy diffusivity to the ambient value. Hence, we set the additional \mathbf{K}' as

$$K'_x = K'_y = K'_z = A_{\text{wake-diffusion}}(0.2L_{\text{eff}})U_n(z). \quad (2.81)$$

(viii) Street canyon

In the street canyon, turbulent fluctuations occur around the overall eddy expressed by the Hotchkiss–Harlow equation (2.51) or the upwind flow given by (2.52). Hence, in the XZ plane (see Fig. 2.13), the relevant length is the distance d_c to the nearest solid wall and the relevant velocity is the local magnitude of the mean flow. Hence, in the local coordinate directions, we set

$$K_X = K_Z = A_{\text{cross-canyon}}d_c\sqrt{U_X^2 + U_Z^2}, \quad (2.82)$$

where U_X and U_Z are given by (2.51) or (2.52).

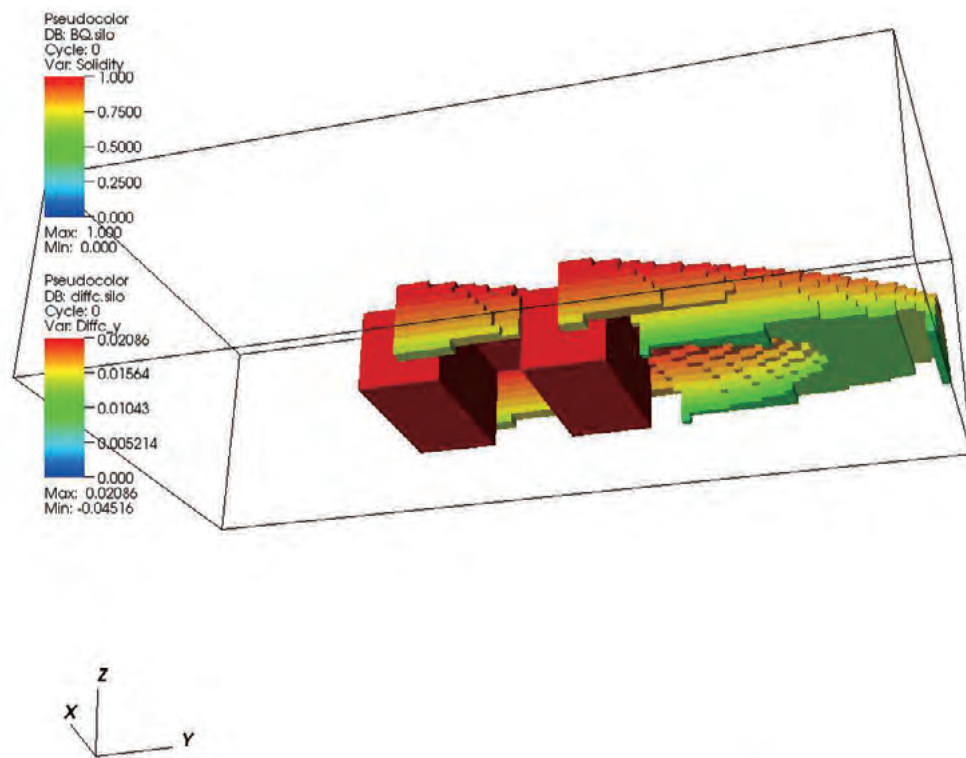


Figure 2.23: Distribution of K_y in the wake diffusion zones of canyon-forming buildings. To illustrate the zone shape, the domain is viewed from the bottom side.

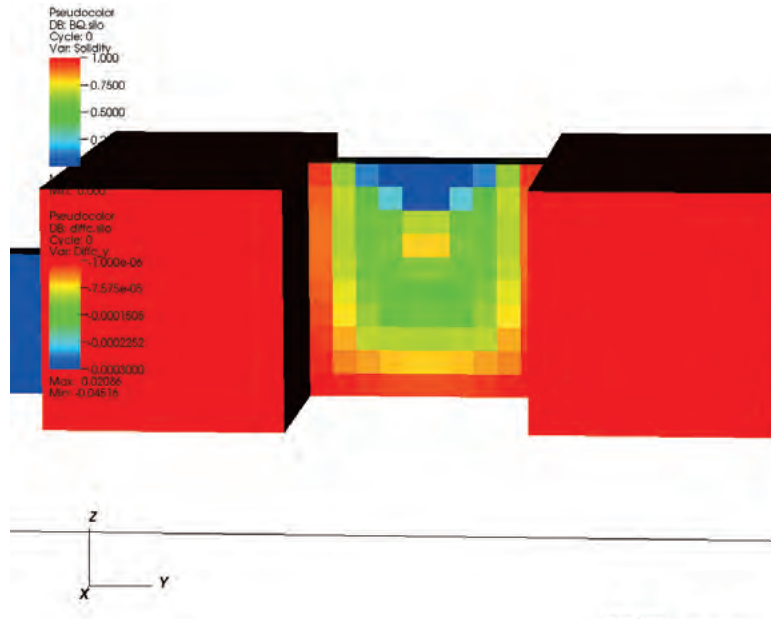


Figure 2.24: Eddy diffusivity K_y in a street canyon. A slice at the middle of the along-canyon direction is shown. In MCAD, eddy diffusivity in special zones where the ambient value is replaced with the zone value is recorded as negative value.

In the Y direction, horizontal eddies of size comparable to the canyon width W_c contribute to diffusion. Hence, we set

$$K_Y = A_{\text{along-canyon}} W_c \sqrt{U_X^2 + U_Z^2}. \quad (2.83)$$

Conversion to the domain coordinates is done by

$$K_x = |K_X \sin \phi + K_Y \cos \phi|, \quad (2.84)$$

$$K_y = |-K_X \cos \phi + K_Y \sin \phi|, \quad (2.85)$$

$$K_z = K_Z, \quad (2.86)$$

where ϕ is the angle the canyon axis (Y axis) makes with the domain axis x .

Fig. 2.24 shows the distribution of K_y in a street canyon. The magnitude is mostly controlled by the distance d_c to the nearest wall. Note that $-K_y$ is drawn on the figure.

2.4 Model implementation

In the computational code, MCAD consists of three major components `mcad_grd`, `mcad_mc3`, and `mcad_ad3`. The first component `mcad_grd` reads the geometrical information of obstacles and emission sources, and generates a numerical grid. The second component `mcad_mc3` divides the domain into various zones in which initial velocity fields and the eddy diffusivity (except in the ambient

zone) are specified, and the mass-conserving velocity field is calculated based on the variational principle. The last component `mcad_ad3` calculates the ambient eddy diffusivity from the given spectral form, and solves the advection-diffusion equation for the concentration field. All the components are coded in GNU C, for which there are many freely available libraries of numerical geometry used extensively in the model. At the time of this publication, MCAD runs on Linux PC only. The source code together with example problems and a user guide can be downloaded at

<https://sourceforge.net/projects/mcad/>

Chapter 3

Comparison with wind-tunnel experiments

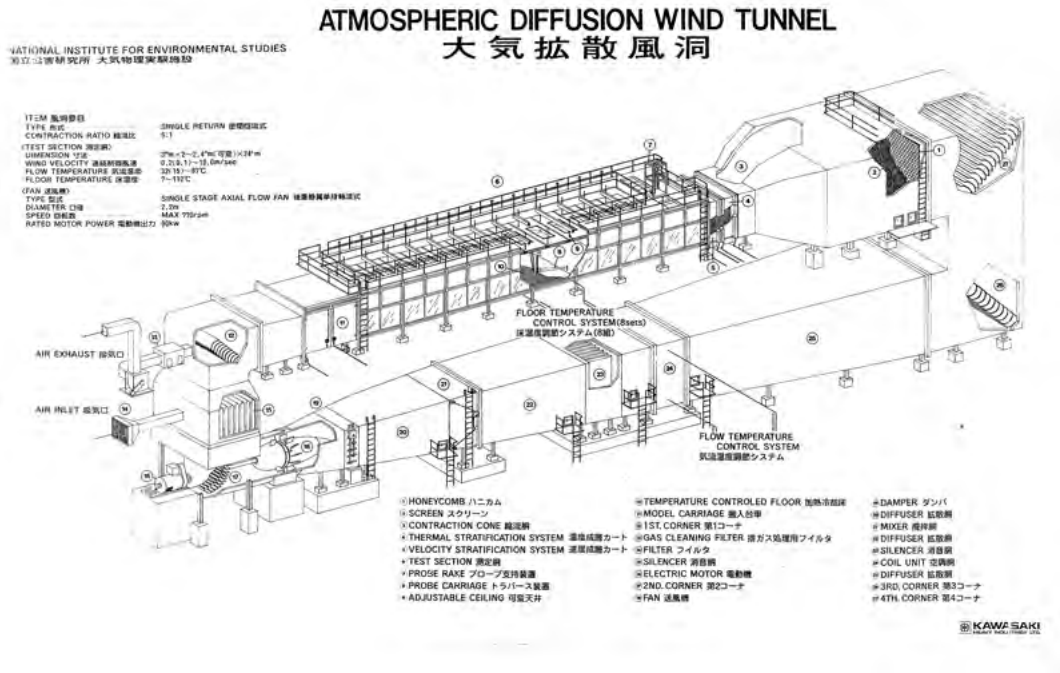


Figure 3.1: Overview of the wind tunnel

3.1 Experimental method

All the experiments were conducted in the Atmospheric Diffusion Wind Tunnel (Ogawa *et al.* 1981) at National Institute for Environmental Studies in Japan. The wind tunnel is vertical closed-circuit type (Fig. 3.1). The test section is 2.6 m wide, 2.2 m high and 24 m long, and the measurements were done around the mid-length. From the test-section entrance to the studied models, roughness elements simulating urban condition were placed on the floor. The roughness elements consisted of a castellated fence (0.18 m high) and five Counihan-type spires (0.9 m high) near the entrance, and Styrofoam blocks (10 cm square at 25% plan area ratio Uehara *et al.* (1993)) or comb-shaped aluminum angled plates (2 cm high, 5 cm wide at 20 cm intervals Kanda *et al.* (2011)) on the floor downwind of the spires (Fig. 3.2).

The wind speed U_∞ at the entrance was either 1.5 or 3.5 m s⁻¹. The criterion (Robins 2003) for fully turbulent boundary layer was satisfied with 1.5 m s⁻¹ (Kanda *et al.* 2011). The velocity spectra obtained from laser Doppler anemometry measurements agreed well with the Kaimal spectra (2.63) and (2.64) except in the low-frequency part of the v spectrum. In the low-frequency part, the measured v spectrum could be fitted well to (2.64) times a Butterworth filter $1/(1 + (f_c/f)^{1/4})$ where the cut-off frequency f_c is $z/2.6$ accounting for the lack of fluctuation modes larger than the wind-tunnel width 2.6 m.

The tracer gas for the diffusion experiments was a mixture of ethane and

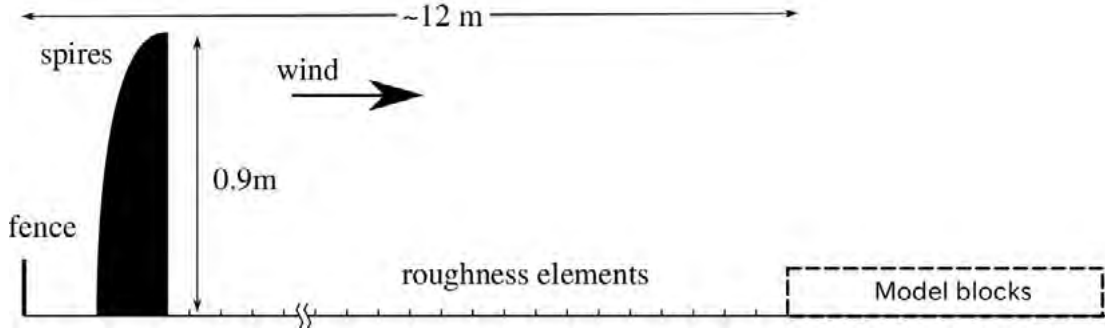


Figure 3.2: Side view of the wind-tunnel test section

nitrogen. It was emitted from a hole on the wind-tunnel floor or from pinholes along pipes of diameter 6 or 8 mm. The concentration of the tracer gas was measured by drawing the air through sampling rakes and leading it to a flame ionization detector calibrated with standard gas.

In the following, coordinates are defined such that x is in the windward, y in the crosswind direction and z in the vertical with the origin on the wind-tunnel floor.

3.2 Model parameters

MCAD has many parameters that can only be determined empirically. For the test cases presented here, the following set of parameter values was found to result in balanced agreement with the experiments.

$$\begin{aligned} A_{\text{near-wake}} &= 0.2, & A_{\text{displacement}} &= 0.05, & A_{\text{wake-diffusion}} &= 0.5, & (3.1) \\ A_{\text{far-wake}} &= 0.05, & A_{\text{canopy}} &= 0.2, & Sc_{t,\text{canopy}} &= 1.0, \\ A_{\text{cross-canyon}} &= 0.01, & A_{\text{along-canyon}} &= 0.2. \end{aligned}$$

$Sc_{t,\text{canopy}}$ was determined by assuming that molecular diffusion is negligible in the urban canopy, and other parameters by trial and error. Note that MCAD results are not very sensitive to the above values; change by one in the last digit of each of the above parameter values does not cause difference in the resulting concentration by more than about 20%.

3.3 Point source and uniform roughness

As shown in Fig. 3.3, tracer gas was emitted from a 13-mm-diameter hole on the wind-tunnel floor. The vertical velocity of the emission was made sufficiently smaller than the wind speed. On the floor from about 1 m upwind to 2 m downwind of this hole, parallelepiped wooden blocks were arranged in a staggered formation. Each block's horizontal section was square with side length $L = 50$ mm and height H ranging in 24, 48, 72 and 96 mm. The block array

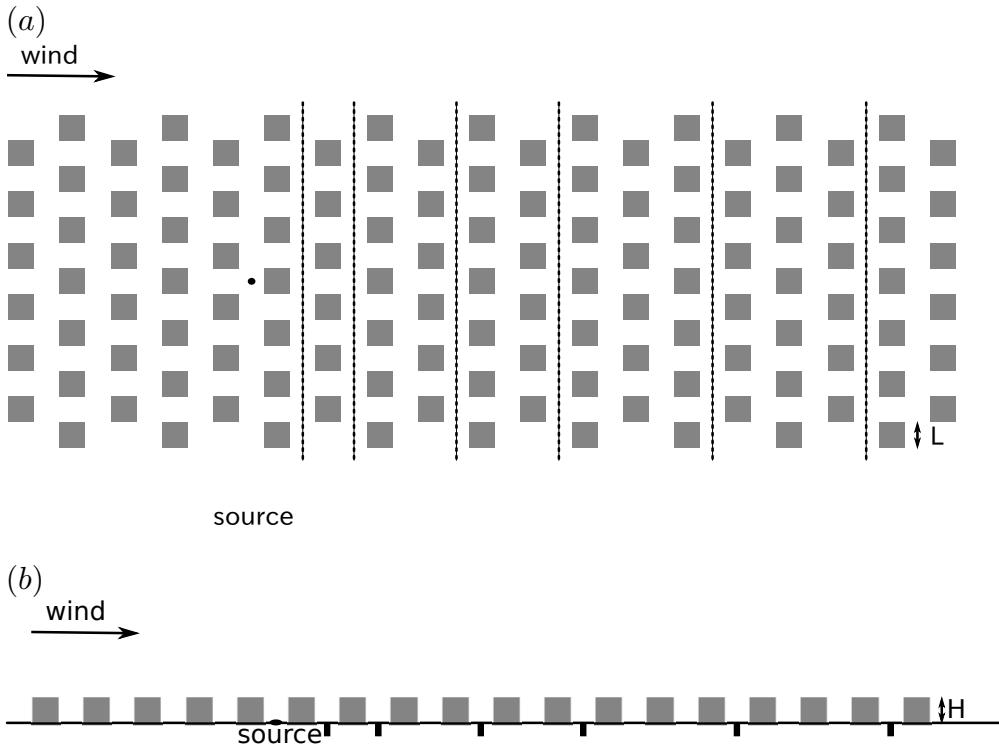


Figure 3.3: Plan (a) and side (b) views of the wind-tunnel point-source diffusion experiments. The filled circle indicates the source of the tracer gas. The tick marks in (b) and dashed lines in (a) indicate the downwind locations where the concentration was measured.

simulates an urban canopy. The plan area ratio is denoted as λ_p . The entrance wind speed U_∞ was 3.5 m s^{-1} . A full description of the experiment and physical analysis is given in Kanda & Yamao (2011).

In the MCAD calculation, the near-wake, displacement, and wake-diffusion zones are defined around each block and the remaining space in $z < H$ is treated as the urban-canopy zone. The region in $z > H$ is classified as the ambient zone. The numerical grid was uniformly spaced at 10 mm interval. This relatively coarse grid is employed to demonstrate the advantage of adopting the mass-conservation principle for velocity calculation. The calculation time was 34 s on a Linux PC with Inter Core 2 Quad Q6600 with sufficient memory that the swap space is not used at all.

Comparison with MCAD simulation is done in crosswind (y) concentration profiles at $z = 5 \text{ mm}$ at selected downwind locations. The origin of (x, y) is defined at the emission source. Fig. 3.4 shows the results with $\lambda_p = 25\%$ and various H values, and Fig. 3.5 with $H = 48 \text{ mm}$ and various λ_p values. The normalized concentration C_n is defined by $C_n = CU_H L^2 / Q$, where Q is the emission rate of ethane, U_H is the wind speed at $z = H$, and C is the measured ethane concentration. The asymmetry of the concentration profiles in the wind-tunnel experiment (circle marks) is due to inevitable setup errors and that in MCAD (solid curves) to the numerical grid that barely resolves the blocks. In

Fig. 3.4, we observe that MCAD reproduces the experiments well for $H = 24$ and 48 mm, but for $H = 72$ and 96 mm, over-estimation near the source and under-estimation far downwind is evident. Here, the poor performance is actually artificial because MCAD parameters were chosen to produce ‘balanced’ performance under typical Japanese urban conditions $H/L = 0.5 \sim 1.0$ and $\lambda_p \sim 25\%$. Note that the behavior far downwind (the rightmost columns in Fig. 3.4) that the concentration decreases with increasing H is correctly reproduced by MCAD although in a little excessive manner.

The large errors near the source exhibit the limitation of the scheme of MCAD. The crude zone definition of MCAD may be responsible, but it should be noted that the initial velocity field for MC in the zones around the blocks comes from wind-tunnel experiments for a block in open flat surface (Rockle 1990), not among similar blocks as in this case. MCAD could be modified to reproduce the experiments for large H , but in the absence of well-established experimental results, it was decided that compromise with the current performance is better than making MCAD further complicated.

The errors in the far downwind region are caused by the error in the near-source region and also in the modeling of the canopy and ambient zones. The latter is related to the estimation of the roughness length z_0 of the urban canopy. MCAD adopts the formula by Macdonald *et al.* (1998), but there are reports suggesting that z_0 by this formula is overestimation (Hagishima *et al.* 2009; Leonardi & Castro 2010; Kanda & Yamao 2011). All these authors suggest that the measured or calculated velocity profiles lead to half as small z_0 as Macdonald *et al.*’s. When the z_0 values are halved, the MCAD results actually agree better with the experiments (including in the near-source region) except for slight deterioration for $H = 24$ mm and $\lambda_p = 25\%$. Representative results are shown in Fig. 3.6. However, we shall retain Macdonald *et al.*’s formula as that representing the real building-block roughness that is usually non-uniform and has larger z_0 than uniform wind-tunnel roughness. Good performance of Macdonald *et al.*’s formula for field observations is demonstrated by Grimmond & Oke (1999).

Fig. 3.7 shows the result of MC+LSM with the same LSM model as Kaplan & Dinar (1996) for $H = 48$ mm. Elastic reflection is assumed at solid surfaces. The agreement with the experiment is comparable to the current MC+AD model. The jagged appearance is due to insufficient number of tracked particles (66000), and does not imply inferiority of LSM. However, to achieve the shown level of agreement, the numerical grid size had to be halved from that for MCAD and a considerably large number of particles had to be tracked, requiring computation time about three orders of magnitude larger than MCAD when run under the same machine condition (no parallel computation employed).

3.4 Line source and simple geometries

The experiments presented in this section were conducted to investigate the diffusion behavior around a road intersection (Uehara *et al.* 1993). Fig. 3.8

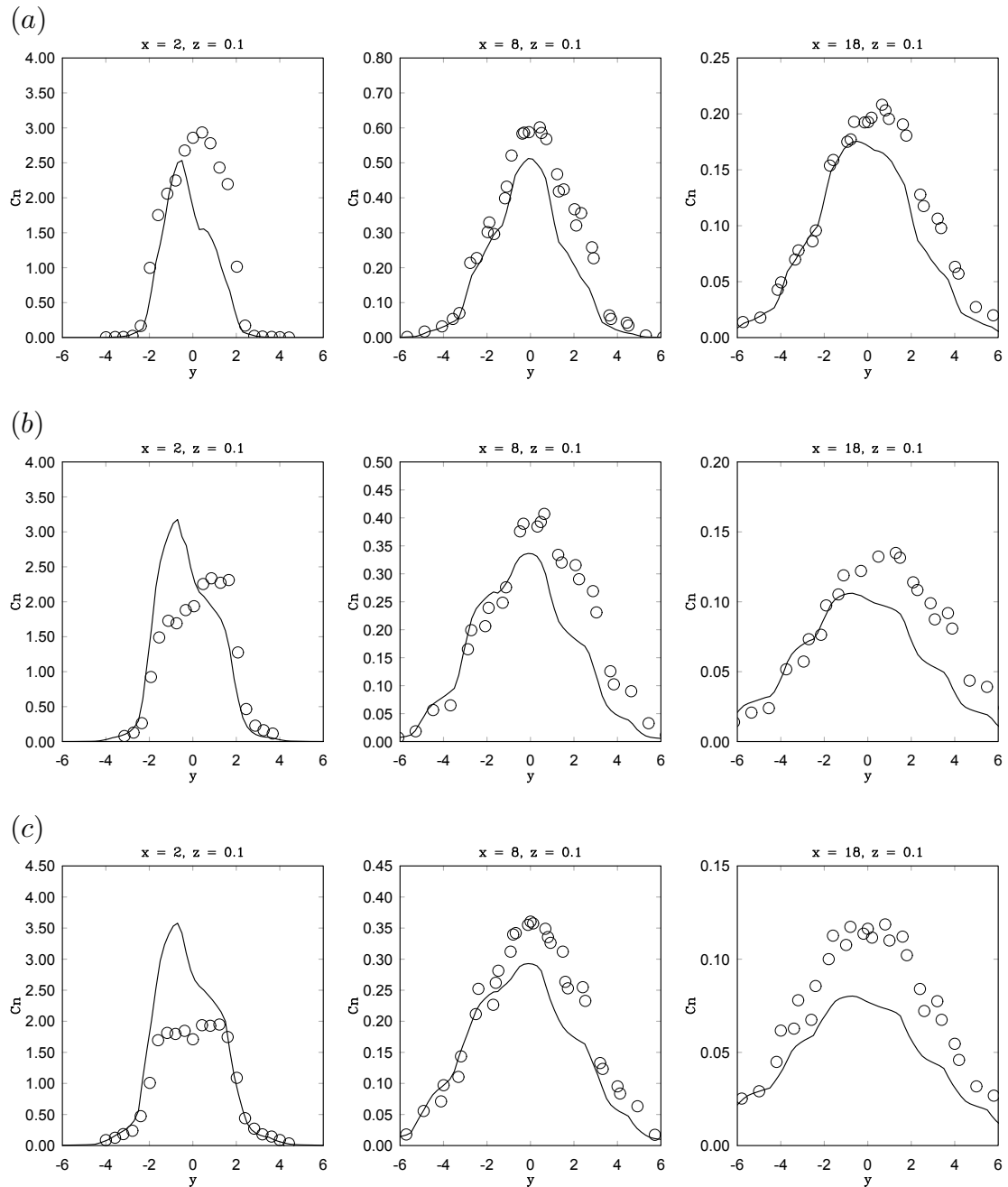


Figure 3.4: Comparison between the wind-tunnel results (open circles) and the MCAD prediction (solid lines) for the point-source diffusion experiments. The plan area ratio λ_p is 25%. The block height H (mm) is 24 (a), 48 (b), 72 (c) and 96 (d). The coordinate values are normalized by the block side length L .

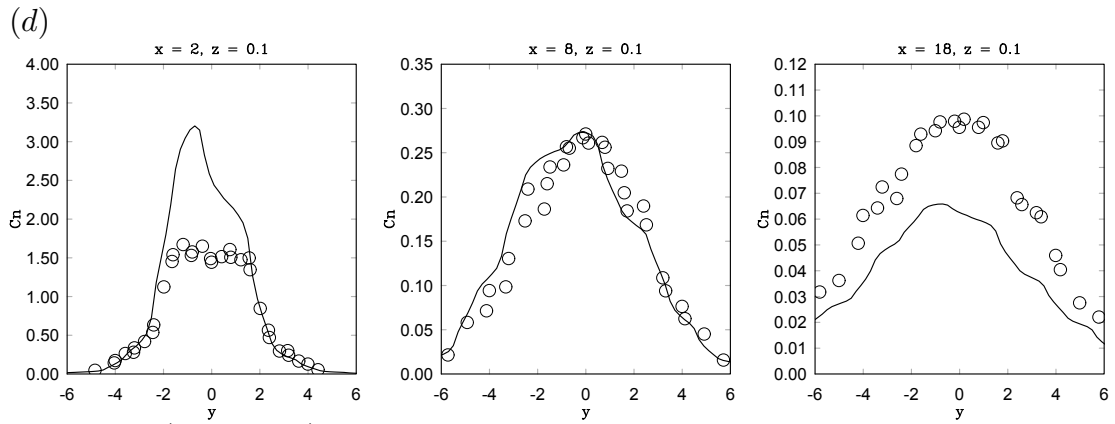


Figure 3.4 (continued)

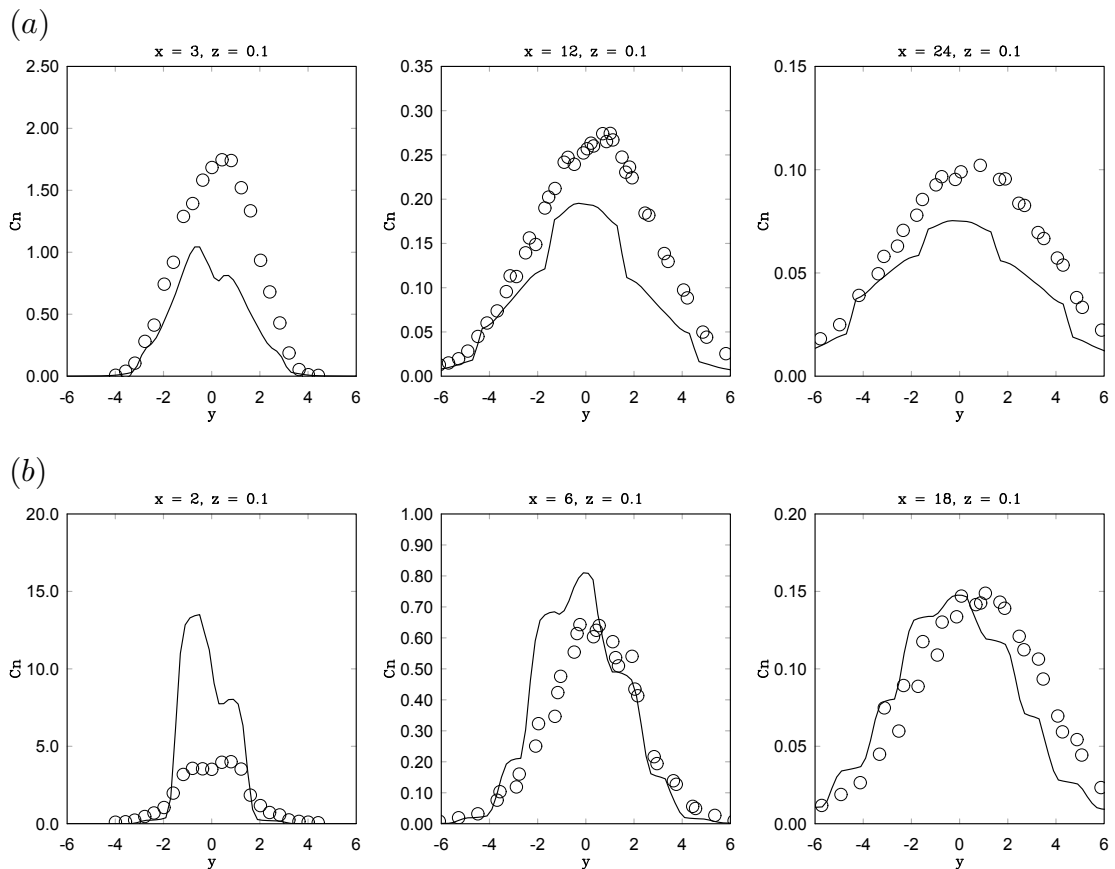


Figure 3.5: Comparison between the wind-tunnel results (open circles) and the MCAD prediction (solid lines) for the point-source diffusion experiments. The block height H is 48 mm. The plan area ratio λ_p (%) is 11 (a) and 44 (b).

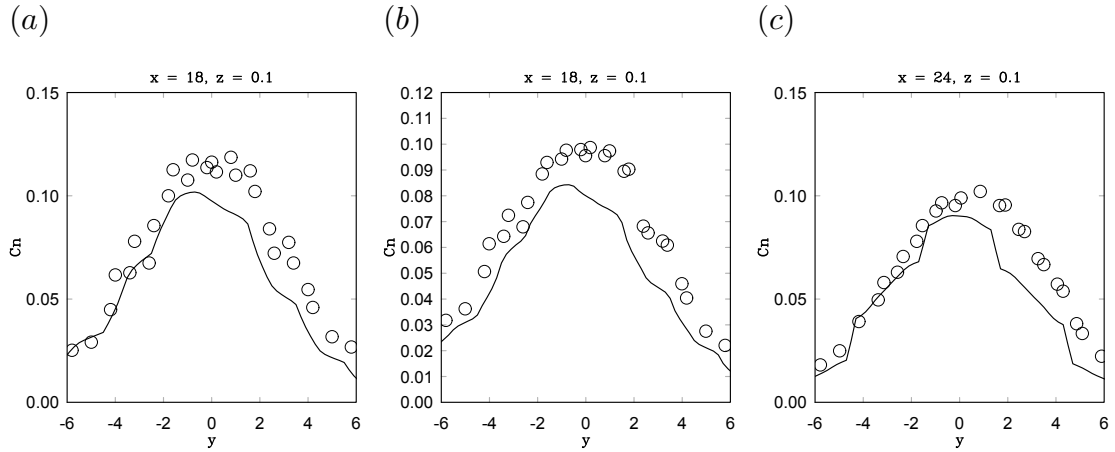


Figure 3.6: Improved agreement when the roughness length z_0 is halved from the default (cf. Figs.3.4 and 3.5). (a) $\lambda_p = 25\%$, $H = 72$ mm, (b) $\lambda_p = 25\%$, $H = 96$ mm, (c) $\lambda_p = 44\%$, $H = 48$ mm.

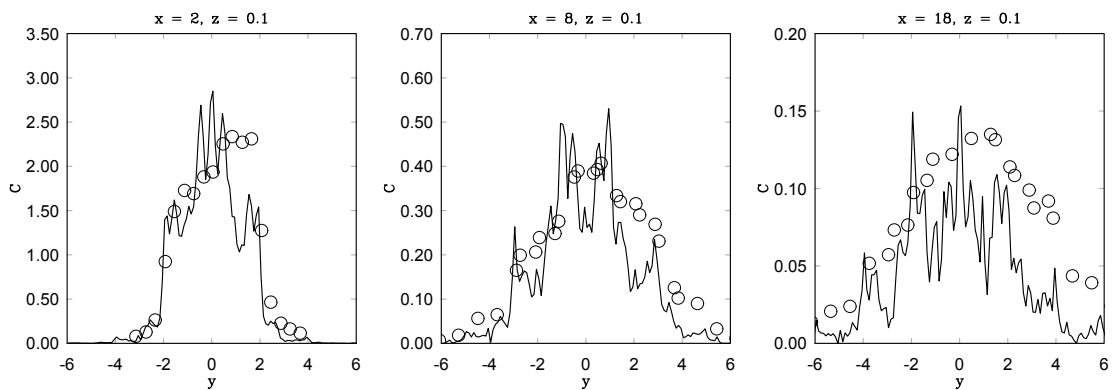


Figure 3.7: Comparison with Kaplan and Dinar's MC+LSM model for the case in Fig. 3.4(b)

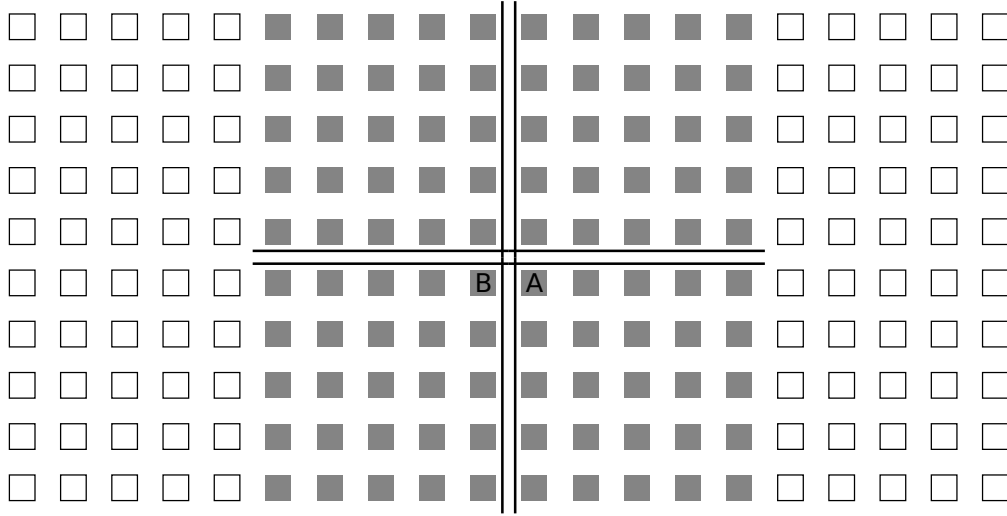


Figure 3.8: Plan view of the wind-tunnel line-source diffusion experiments. The thick lines indicate the emission source when opposite-direction lanes were considered (separate-lane configuration). The blocks have a square section with side length $L = 100$ mm. The white squares have height $H = 50$ mm, the non-inscribed gray ones $H = 100$ mm, and the inscribed gray ones (A and B) $H = 100$ or 300 mm.

shows the plan view of the measurement area. The origin of (x, y) is defined at the center of the intersection. The crossing roads were simulated by line sources along x and y . The line sources were made of 8- mm diameter pipes with downward-facing pinholes from which the tracer gas was emitted. The emission distribution was almost uniform along the pipes with variation within $\pm 20\%$ of the mean (Kanda *et al.* 2011). For experiments focusing on the close neighborhood of the roads, two line sources representing opposite-direction lanes were used (separate-lane configuration). Fig. 3.8 shows this configuration. For broader-scope measurements, one line source per road was placed along the centerline (combined-lane configuration).

The surrounding buildings were made of square-section Styrofoam blocks with side length $L = 100$ mm and various height H . The blocks were arranged in an inline formation with spacing L between the blocks. The test area where the height H was varied is a $2 \text{ m} \times 2 \text{ m}$ square area around the intersection. Outside this area, blocks with height 50 mm were placed in the same formation as in the test area. More than 150 geometries were investigated in Uehara *et al.* (1993), but only representative ones are presented here. The entrance wind speed U_∞ was 1.5 m s^{-1} . The concentration is normalized as $C_n = CU_H L / Q_L$ where Q_L is the emission rate per road length.

In the MCAD calculation, uniform numerical grid with 20 mm spacing was employed. The results were not much different when a finer 10 mm grid was employed. The results with 20 mm grid are presented below to demonstrate the cost effectiveness of MCAD.

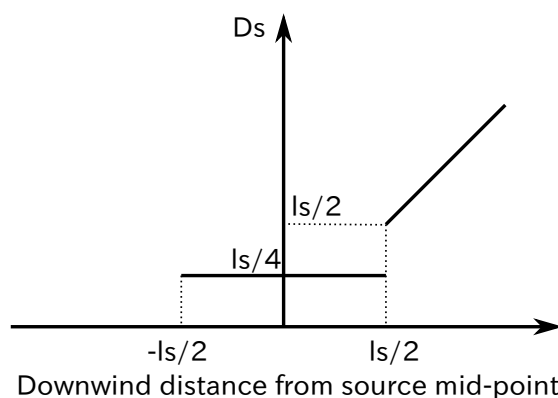


Figure 3.9: Definition of D_s when the source is parallel to the wind direction.

3.4.1 Oblique wind

In this set of experiments, dependence on the wind direction was investigated. The block height H was 100 mm in the test area. The wind direction θ was varied in 0° and 45° by the ordinary mathematical angle definition ($\theta = 0$ in the x direction). The sources were in the combined-lane configuration, and the concentration was measured at $z = H/4$ along the centerline between the blocks.

When $\theta = 0$, one of the line sources is parallel to the wind. Because MCAD specifies the ambient eddy diffusivity as a function of downwind distance D_s (distance measured along the flow direction) from the source, special treatment is required for wind-parallel sources. First, the source is divided into short segments, then for each segment, D_s is measured from the mid-point of the segment. When the concerned point is near the source, or more specifically, lies inside the region bounded by the wind-normal lines through the ends of the source segment, D_s is fixed at $l_s/4$ where l_s is the length of the segment. Fig. 3.9 shows D_s as a function of the real downwind distance from the mid-point of the segment. The segment length is set 0.4 m in this case, *i.e.* the 2 m-long line source is divided into 5 segments. In real cases, a source is seldom exactly parallel to the wind direction. For application to real cities, a source is regarded parallel to the wind if the angle between the wind and the source line is less than a given threshold value, say, 15° . In MCAD, this procedure is conducted automatically based on the given segment length and the threshold angle.

Fig. 3.10(a) and (b) show the concentration contours of the experiment and MCAD, respectively. The overall feature is well reproduced by MCAD, but there are apparent discrepancies. To clarify the difference, Fig. 3.10(c) shows the concentration profiles along x at $y = 4L$. Agreement for $\theta = 0$ is fair, but for $\theta = 22.5^\circ$ and 45° , the concentration magnitude and the profile shape deviate considerably from the experiments. Comparison at $y = 2L$ is similar (not shown). Due to these discrepancies particularly near the source, the correlation plots between the experiment and MCAD (Fig. 3.10d) are quite unsatisfactory for $\theta = 45^\circ$. Similarly poor performance resulted with $\theta = 22.5^\circ$.

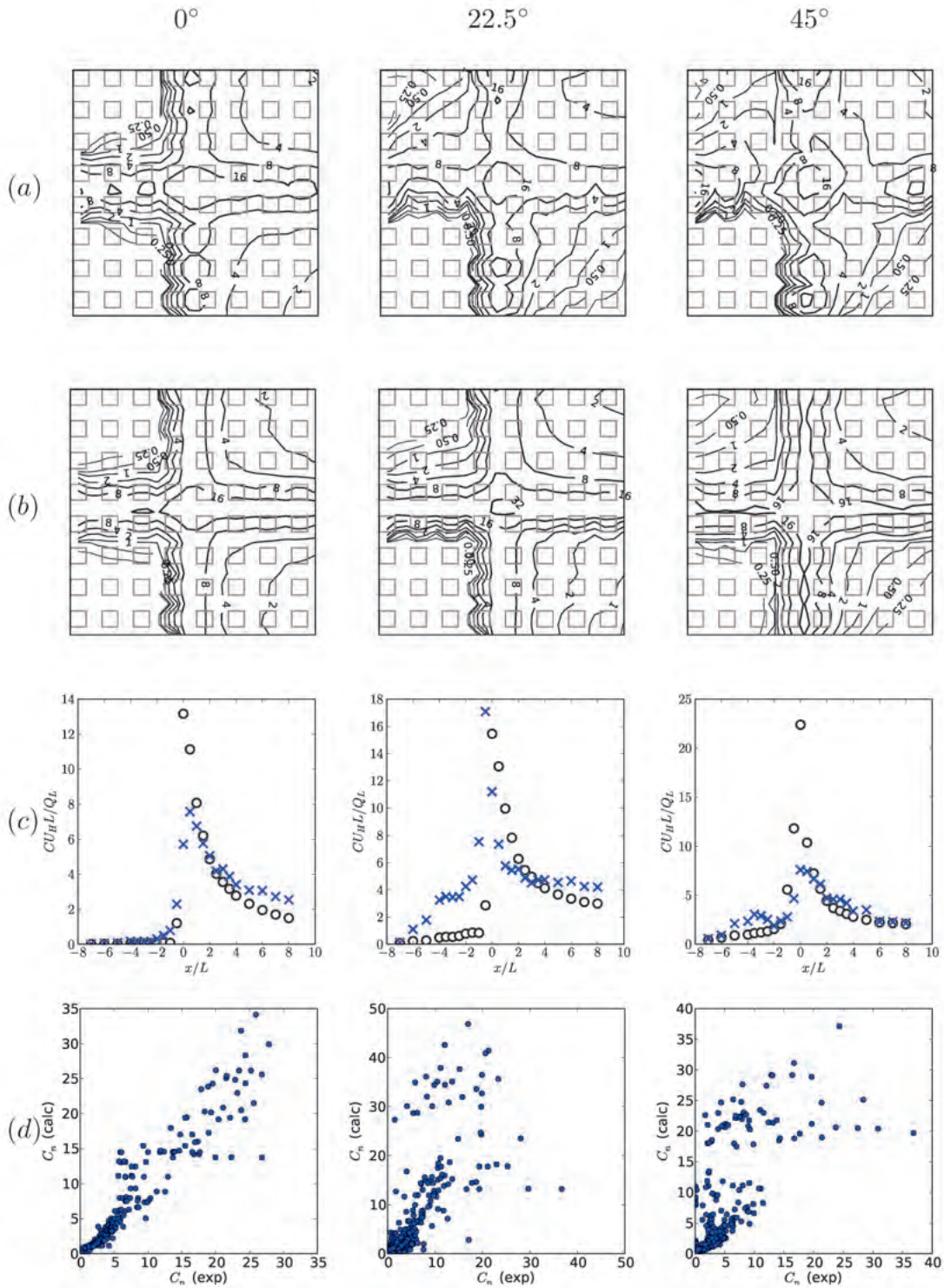


Figure 3.10: Results of line-source diffusion for various wind directions. (a,b) Concentration contours of wind-tunnel experiments and MCAD calculation, respectively. (c) Concentration profiles along x at $y = 4L$. Cross is experiment and circle is MCAD. (d) Correlation between the experiments (horizontal axis) and MCAD calculation (vertical axis).

The poor performance for $\theta \neq 0$ is related to the crude specification of the zones around the blocks. MCAD adopts the Rockle method (Rockle 1990) which, for oblique wind direction, defines an ellipsoidal displacement zone on each of the windward sides of a block and an ellipsoidal wake zone spanning the two leeward sides. This method can be regarded as an engineering technique to produce results that may not be correct but not far from the true solution. However, knowledge about the true solution has not yet been organized as well as in the $\theta = 0$ case. MCAD could thus be improved if wind-angle dependence were well established.

3.4.2 Street canyon

This set of experiments investigated the diffusion behavior in street canyons. If a street canyon is in the skimming-flow regime (Kaplan & Dinar 1996), a quasi-steady eddy occupying the street canyon is generated by the canyon-top wind. Because this eddy recirculates the pollutant inside the street canyon, the concentration in a street canyon becomes higher than if the street canyon does not exist. Also, because the wind direction near the ground is opposite to that above the street canyon, the pollutant is first carried toward the upwind building which, without the street canyon, would be little exposed to the pollutant.

For $H = 100$ mm and $\theta = 0^\circ$, the space between the blocks aligned in the wind direction (*e.g.* the space between A and B blocks in Fig. 3.8) becomes a street canyon in the skimming-flow regime. To obtain detailed concentration distribution, measurement was done along 6 lines parallel to the sources in each-direction street at $z = H/4, H/2, 3H/4$ and H .

Fig. 3.11 shows the concentration profiles in the x direction inside a street canyon ($y = L \pm L/10$) and outside ($y = 2L \pm L/10$) at $z = H/4$ (a), $H/2$ (b), $3H/4$ (c), and H (d). Note that the discrepancies between the pairs of MCAD prediction is due to the use of coarse grid and interpolation. Agreement between the experiment and MCAD calculation is good except at $z = H/4$ and $y = 2L$. We observe that, within street canyons ($y = L$), the concentration is higher on the leeward (smaller x) of the blocks due to the near-ground wind directed opposite to the imposed ambient wind.

The poor performance at $z = H/4$ and $y = 2L$ is related to the velocity field outside street canyons. The region around $y = 2L$ in $z < H$ is classified as the canopy zone where the mean velocity field is specified by the Coceal–Belcher method (Coceal & Belcher 2004). Because the Coceal–Belcher velocity field is horizontally uniform and the variation near individual blocks is neglected, there can be large errors that can affect the concentration field especially near the emission source. Such a problem does not occur if there is well-defined wind above the source as inside street canyons or if the concerned point is separated from the source by a long distance or by solid obstacles as in the case of §3.3.

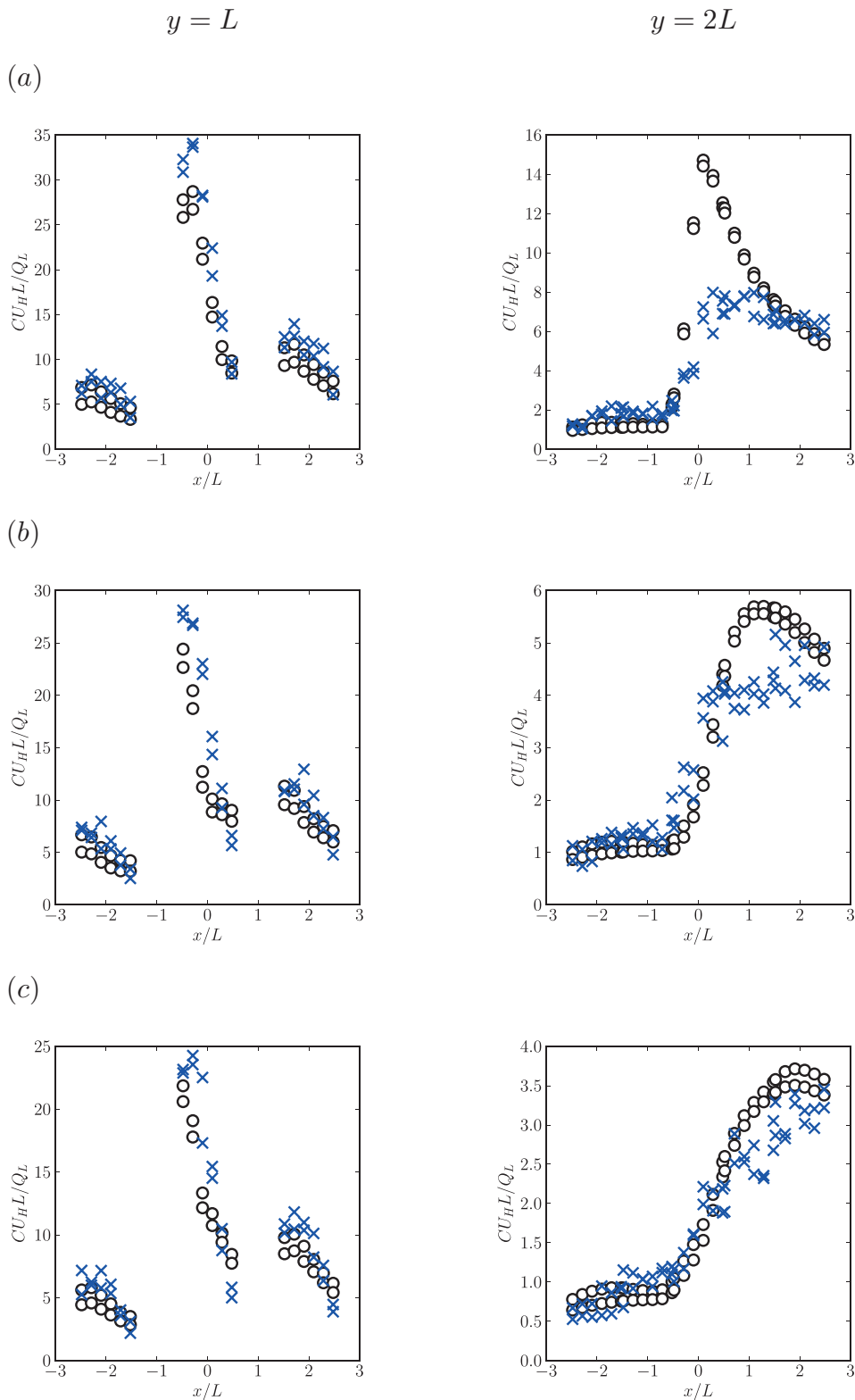


Figure 3.11: Concentration profiles along x at $z = H/4$ (a), $z = H/2$ (b), $z = 3H/4$ (c), and $z = H$ (d) inside a street canyon ($y = L$) and outside ($y = 2L$). Cross is experiment and circle is MCAD. Measurement and MCAD calculation (interpolation of the grid values) were actually done at $y = L \pm L/10$ and $y = 2L \pm L/10$. The values at these lines are plotted as those at $y = L$ and $y = 2L$, respectively.

(d)

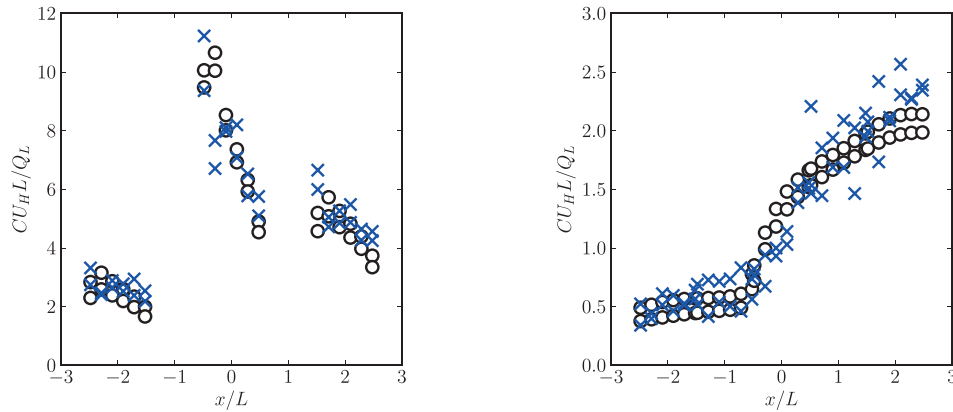


Figure 3.11 (continued)

3.4.3 Tall buildings

This set of experiments investigated the effect of tall buildings near the intersection. Among many configurations studied, we present one case where the block A in Fig. 3.8 was 3 times taller than the surrounding. In MCAD, buildings taller than 2.5 times the mean building height are classified as ‘tall buildings’, and the velocity field in their wake is specified by the formula of Taylor & Salmon (1993). In the experiments, however, only the neighborhood of the tall buildings was measured in detail. Therefore, it is not the adequacy of the far-wake zone peculiar to tall buildings but that of the zones attached to buildings much taller than the surrounding urban canopy that is evaluated here.

The line sources were in the separate-lane configuration, and the concentration was measured along 6 lines parallel to the sources in each street at $z = 25$ mm (1/4 of the height of blocks other than A).

Fig. 3.12 shows the concentration contours of the experiments (a) and the MCAD calculation (b). For reference, the results when A had the same height as the surrounding are shown together. The low concentration around the tall building (Fig. 3.12a A) attributable to enhanced wind speed and turbulence intensity has also been reported in Pascheke *et al.* (2008). We observe that the contours of the experiments (Fig. 3.12a) are considerably deformed around tall buildings whereas MCAD results (Fig. 3.12b) are little affected by the tall buildings. Consequently, the correlation between MCAD and the experimental results is quite poor when A is tall (Fig. 3.12c). The correlation for the reference case (Fig. 3.12c right) is not good either at large values, but it is due to the near-source inaccuracy discussed in the previous subsection. Similarly poor performance resulted when the block B (see Fig. 3.8) was three times taller than others.

The difference in the effect of tall buildings comes from the priority settings of the zones. In MCAD, the canyon zones in front and rear of the tall buildings have higher priority than near-wake or displacement zones. Because the velocity field near the ground in a canyon zone given by the Hotchkiss–Harlow formula

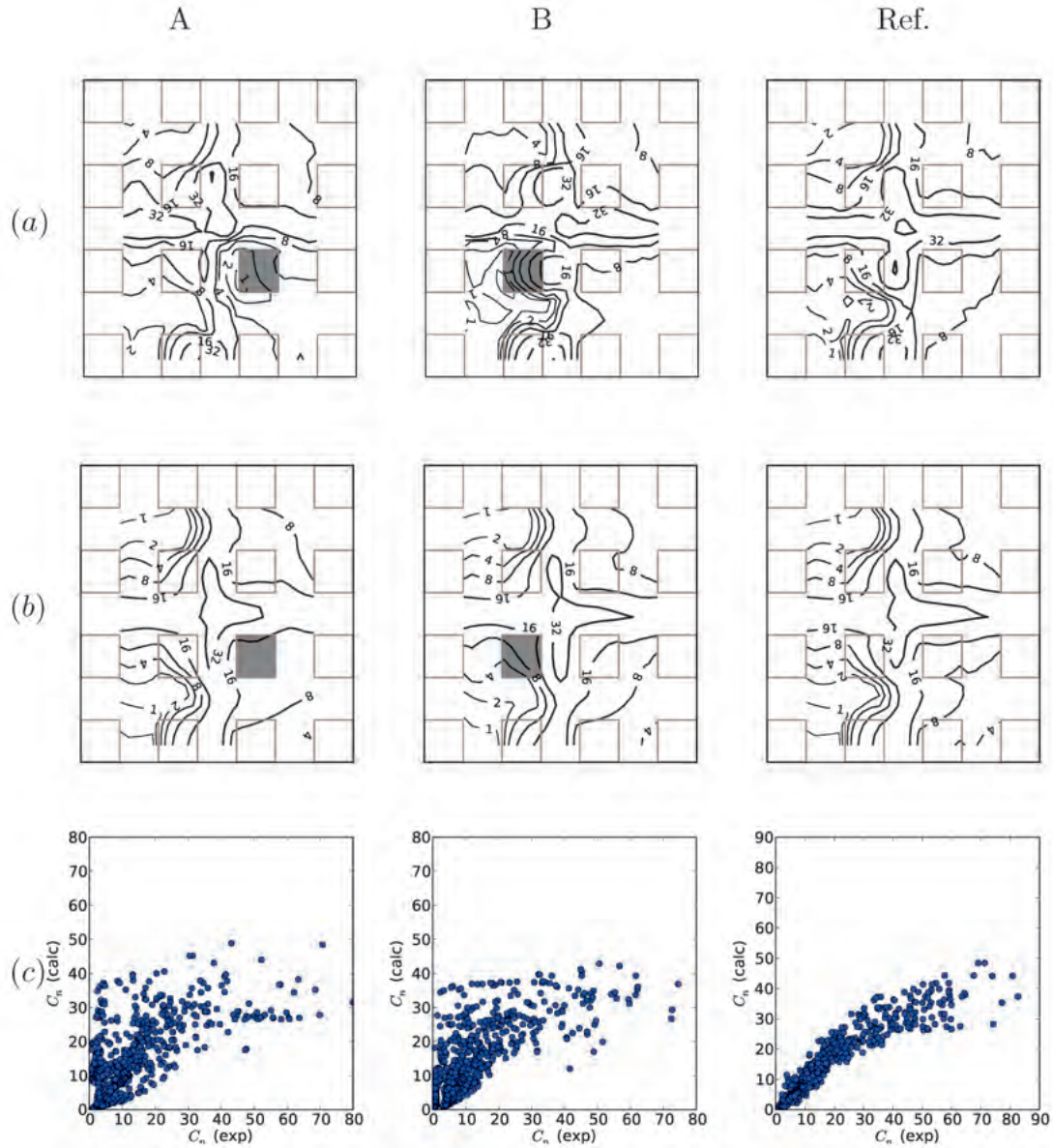


Figure 3.12: Results of line-source diffusion when the height of building A or B is varied. In columns A and B, the respective building (shaded by gray) is three times taller than the surrounding. In column Ref., A and B has the same height as the surrounding. (a, b) Concentration contours of wind-tunnel experiments and MCAD calculation, respectively. (c) Correlation between the experiments and MCAD calculation.

(Hotchkiss & Harlow 1973) or Uehara *et al.*'s experiments (Uehara *et al.* 2001) is not much affected by the difference in the height of the canyon-forming buildings, the resulting concentration field is almost unchanged. In reality, however, the velocity field in and around a street canyon when facing buildings have different heights and the building width is comparable to the canyon width should be far more complex than the Hotchkiss–Harlow formula or the formula derived from Uehara *et al.* (2001). Particularly, lateral flows induced by convergence or divergence at the ground level in the near-wake or displacement zone, respectively, around tall buildings are not properly modeled by MCAD.

Although Uehara *et al.*' reports detailed velocity measurement results for various height combinations, the number of measured points were still insufficient and the overall velocity field could not be readily summarized into a general formula. Uehara *et al.*'s experiments, however, provide valuable validation data for fluid-dynamical numerical simulations, which could be used for establishing formulas involving flow both in and out of street canyons for various configurations.

The poor performance in this case does not necessarily mean that MCAD is not useful in complex geometries of real urban areas. In some urban areas in Europe or North America, tall buildings are relatively wide such that the Hotchkiss–Harlow formula is valid. In Tokyo or London, as will be shown in the next section, tall buildings do not usually form street canyons. Therefore, MCAD can produce reliable results for many urban settings. However, in places like 'Setagayapost' described in the next section, where tall buildings do form narrow street canyons, MCAD results should be viewed with caution. Complexity of urban velocity field is also demonstrated by wind-tunnel observation of Carpentieri *et al.* (2009).

3.5 Real cities

3.5.1 City models

Diffusion from roads at five Japanese urban sites was studied by wind-tunnel models at a reduction ratio of 1/300. The five sites have trunk roads with high exhaust emission rate from diesel vehicles. The wind-tunnel models cover 600 m-diameter area with the center on the trunk roads. For each site, eight compass-point wind directions were realized by rotating the model around the center. The approach flow was made turbulent by the same method as in §3.3. The average building height was about 10 m by the real scale, which is about 33 mm in the reduced scale. Hence, the wind-tunnel models correspond to the intermediate of $H = 24$ and 48 mm cases in §3.3. Only the emission from the trunk roads was simulated by line sources similar to those used in §3.4, and emission from other narrower roads was neglected. The emission rate along the trunk roads was made approximately uniform although the real emission rate has variations due to deceleration and acceleration of vehicles at traffic signals. Modification of the emission distribution due to traffic signals is described in

§4.2. More detailed description of the experiment and comparison with field monitoring data are given in Kanda *et al.* (2011).

Table 3.1: Features of the studied sites.

Site	Hachimanyama	Itaka	Kadoma	Ashiya	Setagayapost
Prefecture	Tokyo	Aichi	Osaka	Hyogo	Tokyo
Latitude ^a	35°39'54.0"	35°10'42.0"	34°44'36.4"	34°43'47.6"	35°38'24.7"
Longitude ^a	139°36'49.8"	137° 0' 7.8"	135°34'53.5"	135°18'53.2"	139°40' 6.3"
Surface road	Loop 8	Route 302	Osaka Central Loop	Route 43	Route 246
Express way	–	Higashimeihan (underground)	Kinki (elevated)	Hanshin (elevated)	Metropolitan (elevated)
Noise barrier	–	○	–	○	–
λ_p	0.24	0.22	0.44	0.35	0.46
\overline{H} (m)	10.0	8.9	7.7	9.2	12.2

^a value at the center of the wind-tunnel model

The characteristics of the five sites are listed in Table 3.1. The sites cover a wide range of plan area ratio λ_p (0.22~0.46) and average building height \bar{H} (8.9~12.2 m). In Japan where expressways are often built parallel to surface roads, various road structures exist. In Hachimanyama, the only trunk road is a surface one. In Ashiya, Kadoma and Setagayapost, elevated expressways run parallel to the surface road, and in Itaka, an expressway runs underground between the opposite-direction lanes of the surface road. In Setagayapost, there is also a bypass road at the mid-height of the surface road and the elevated expressway. Diffusion experiments were conducted separately for different height roads. Further complicating the geometry, in Ashiya and Itaka, there are 5-meter tall noise barriers along the curb of the surface roads to confine traffic noise as well as pollutants inside the roads.

Note that Setagayapost was not analyzed in Kanda *et al.* (2011) because the relatively busy side streets and the traffic signals made comparison with the field monitoring data difficult. However, for comparison between wind-tunnel experiments and the MCAD calculation, such a problem does not occur because the source distribution is known.

There is restriction to the wind direction due to the chosen measurement method. In the experiments, the concentration field was measured by sucking air through a sampling rake with 11 pipes of diameter 3 mm and length 470 mm. The spacing between the pipes was 120 mm. The sampling rake was held by a structure fixed on the city model such that the spanwise direction of the sampling rake was parallel to the trunk roads. The spacing between the sampling pipes was wide enough not to pose considerable blockage to the oncoming wind when the wind direction was not close to parallel to the trunk roads. However, for wind directions close to parallel to the trunk roads, the effective pipe spacing becomes narrow and the blockage is non-negligible. Actually, smoke visualization revealed that the flow was bent toward the spanwise direction of the rake, making the flow parallel to the trunk road even when the wind is only near-parallel. Of the eight wind directions experimented in the wind tunnel, two had trunk roads within 22.5° (16-compass-point angle division) from the wind direction. In the following, these two wind directions are excluded from comparison between the experiments and the MCAD calculation.

In Itaka and Kadoma, special treatment is necessary because the trunk roads are not straight (see Fig. 3.17*b,c*). As with the line source parallel to the wind direction, curved sources need to be divided into short segments so that the downwind distance D_s is uniquely determined for each segment. Because MCAD is implemented such that sources are specified as a set of linear segments, a curved source is already given as a set of short segments (see Fig. 3.15*a*). The MCAD calculation could be done by solving the AD equation with the eddy diffusivity defined for each segment and summing the results for all the segments, but if the angle difference between the segments is so small that the calculated D_s is almost the same, the additional numerical cost is futile. Hence, to reduce the numerical cost, the original segments are combined into groups each of which form an approximately straight line. The criterion for grouping is that the member nodes are within 20 m from the straight line defined as the least-

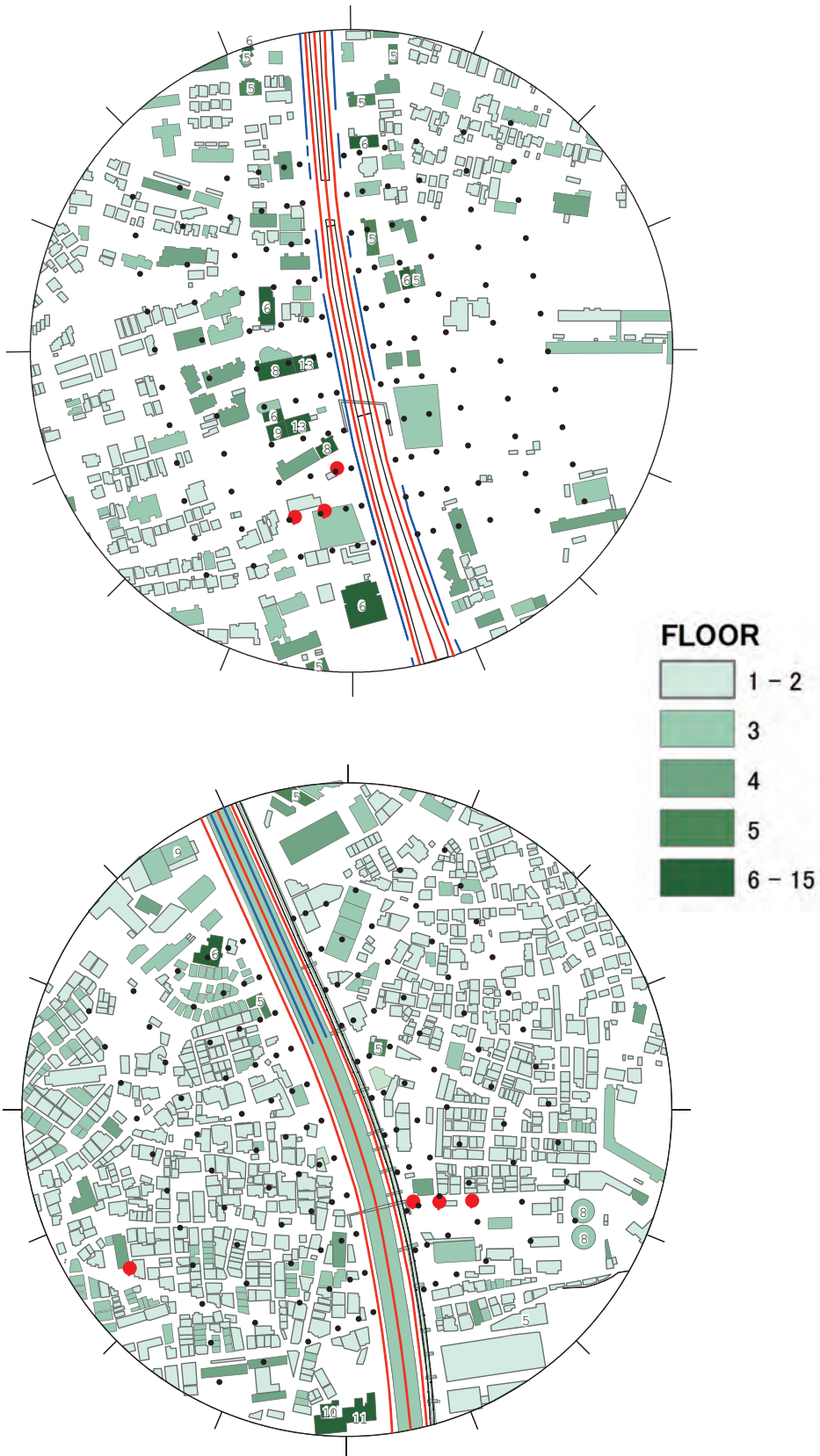


Figure 3.13 (continued)

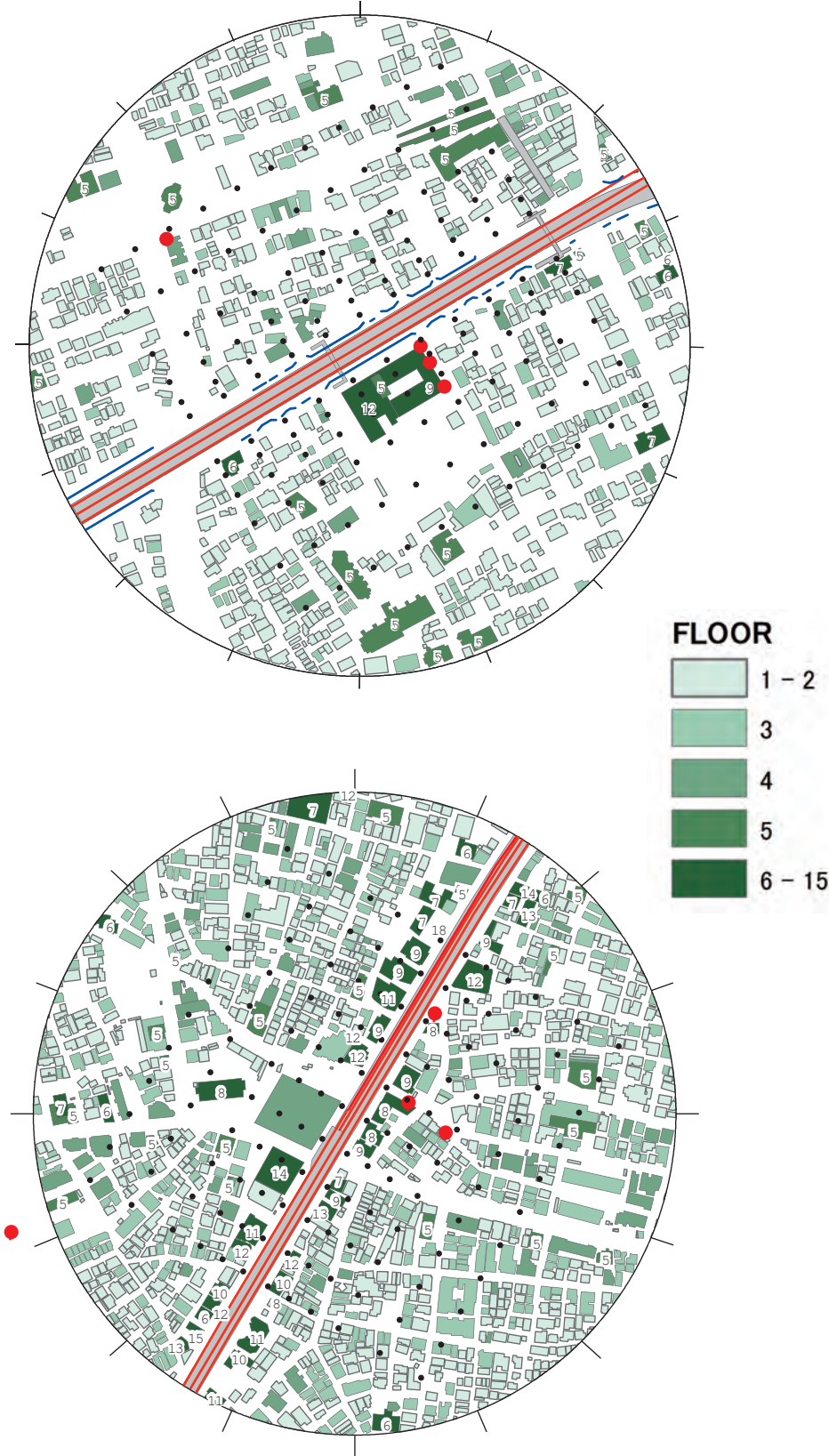


Figure 3.13 (continued)

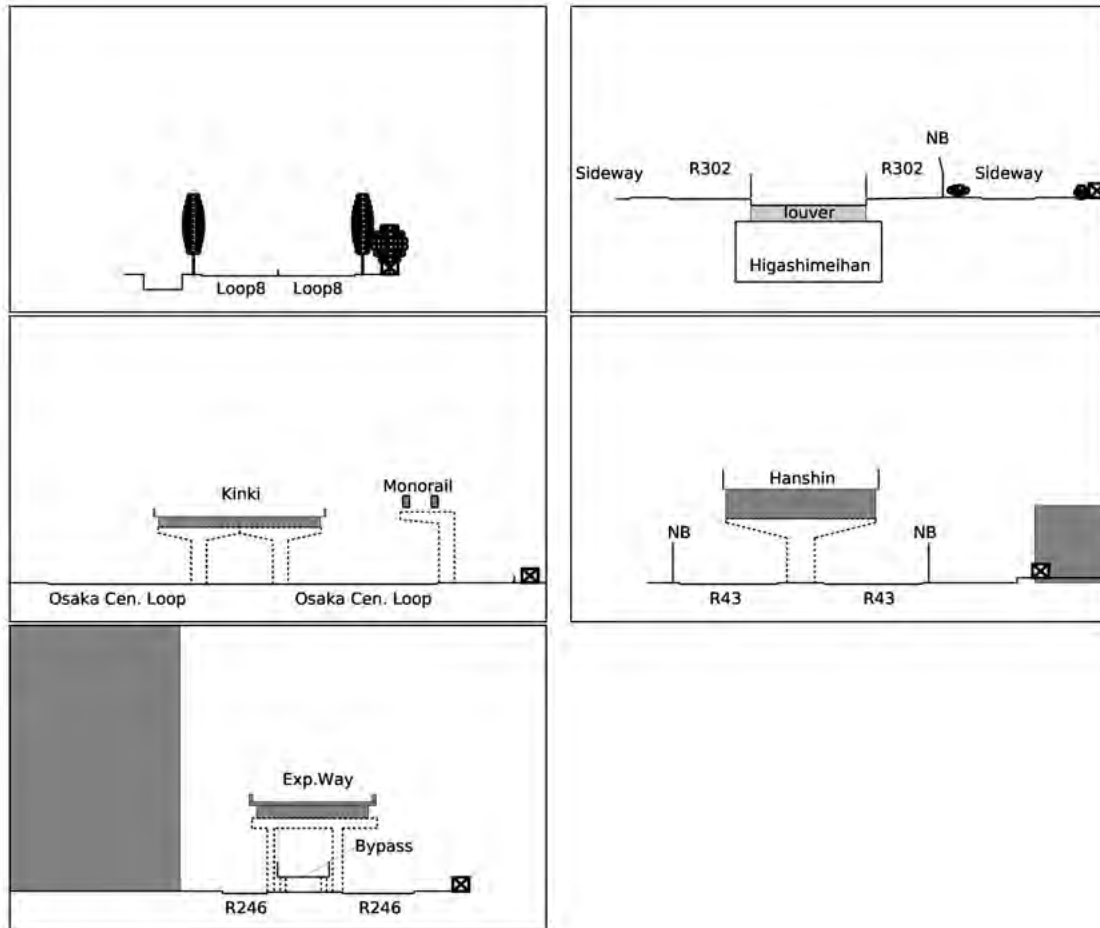


Figure 3.14: Vertical sections of the city models. The frame width is 70 m. The solid squares indicate the locations of the monitoring station nearest to the trunk roads. All the vertical sections are oriented such that these near-road stations are on the right side of the road. The gray blocks next to the roads represent buildings. If structures (for example, columns of the elevated roads) do not coincide with the section line, they are indicated by dotted lines; otherwise, they are indicated by gray polygons. The clusters of dark circles indicate tree leaves. Trees are drawn only when they extend for a substantial distance along the roadside.

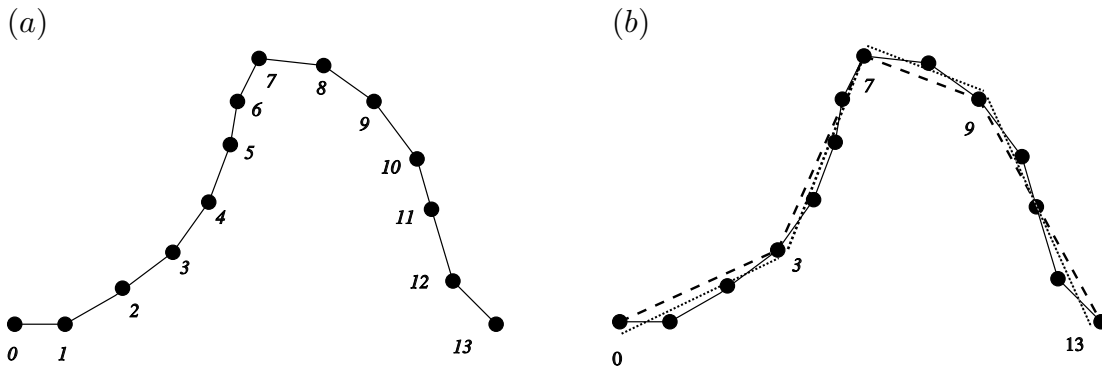


Figure 3.15: Regrouping of a curved source. A source represented by 14 nodes is grouped into 4 segments, each of which is approximated by a regression line (dotted line).

squares regression line.

The grouping procedure is explained by a source shown in Fig. 3.15. The source is specified by the 14 nodes indicated by filled circles. From the node 0, temporary lines are drawn to the nodes with increasing number ($0 \rightarrow 1$, $0 \rightarrow 2$, $0 \rightarrow 3$, ...) until the maximum distance between the line and the intermediate nodes exceed a specified threshold value. Then, the node (node 3 in Fig.3.15) immediately before this event occurs is selected as the end node of the first group. The procedure is repeated with the node 3 as the starting end, and continued until the last node 13 is reached. In Fig. 3.15(b), the original source nodes are grouped into 0-3, 3-7, 7-9, and 9-13. In Fig. 3.15(b), all the intermediate nodes are within a given threshold distance from the dashed lines. The approximate straight lines used to calculate D_s and eddy diffusivity are defined as the least-squares regression lines (indicated by dotted lines in Fig. 3.15b) through the nodes in the groups. For the city models, the threshold distance is set at 20 m by the real scale.

MCAD calculation was conducted with uniform numerical grid with 10 mm spacing. Structures thinner than 10 mm (3 m by the real scale) but non-negligible for diffusion behavior, *e.g.* noise barriers, were expanded to the grid size. Fig. 3.16 shows a bird's-eye view of Ashiya. Almost the same amount of computational time was spent on geometrical manipulation of zones as on iterative solution of the AD equation. Typical calculation time for one wind direction and one source group was 5 min if compiled as a C code on a PC with Intel Core2Duo and 2GB RAM.

3.5.2 Results and comparison with a Gaussian-plume model

Fig. 3.17 shows concentration contours at $z = 6$ mm (1.8 m by the real scale) for the wind-tunnel experiments and the MCAD calculation. The concentration is normalized as $C_n = C/Q_L$ where U_H or \overline{H} are not used in order to show the difference in the overall concentration level due to the different building configurations. Only one wind-direction (indicated by arrows) and surface-road emis-

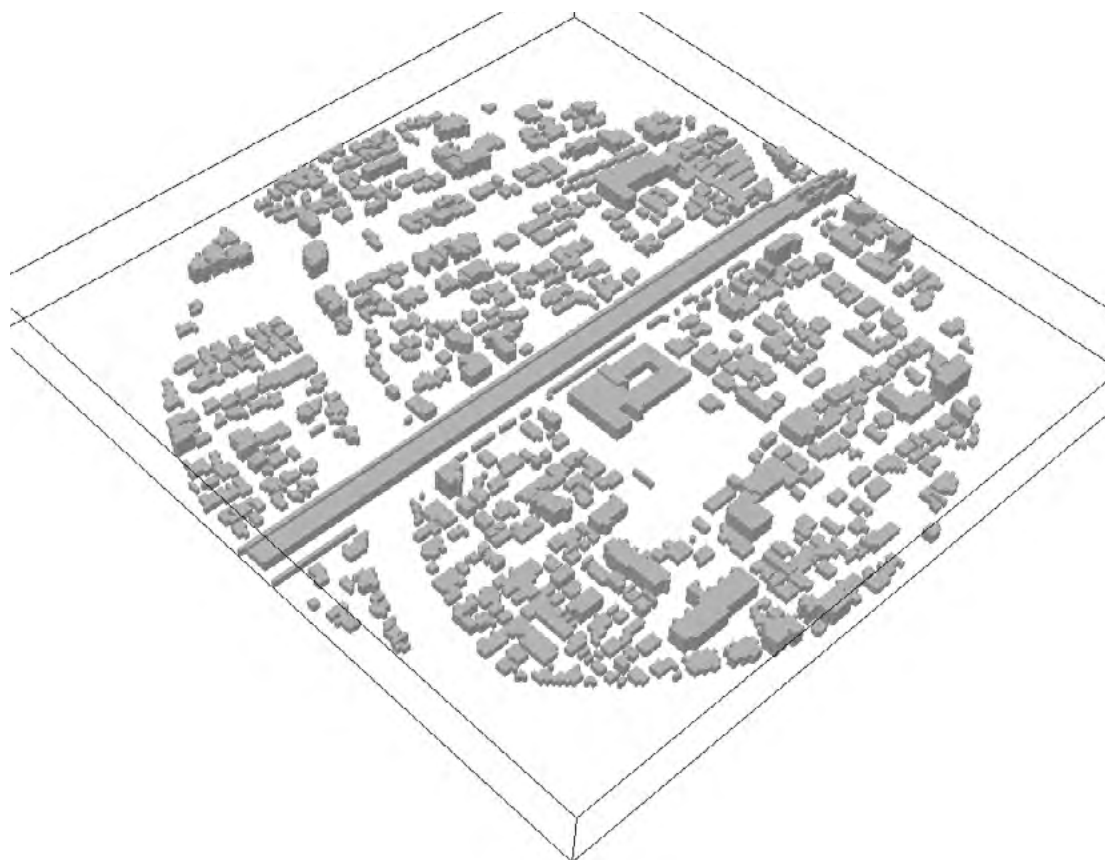


Figure 3.16: Bird's-eye view of MCAD grid of Ashiya. The grid was visualized by VisIt of the Lawrence Livermore National Laboratory.

sion case is shown for each site. We observe that some qualitative features are properly reproduced by MCAD. The concentration variation generated by the presence or absence of roadside buildings is approximately similar to the experiments. Especially noteworthy are the non-zero concentration regions upwind of the sources generated by tall roadside buildings, which cannot be reproduced by conventional Gaussian-plume models. However, close examination at each measurement point reveals considerable discrepancies often greater than 100%. The discrepancies are prominent near the sources.

As expected from the result in §3.4, MCAD is not a satisfactory tool when prediction at a small number of points is of concern. Hence, it should not be used in, for example, deciding where to install permanent air monitoring stations. For such purposes, MCAD's status is not much different from conventional Gaussian-plume models.

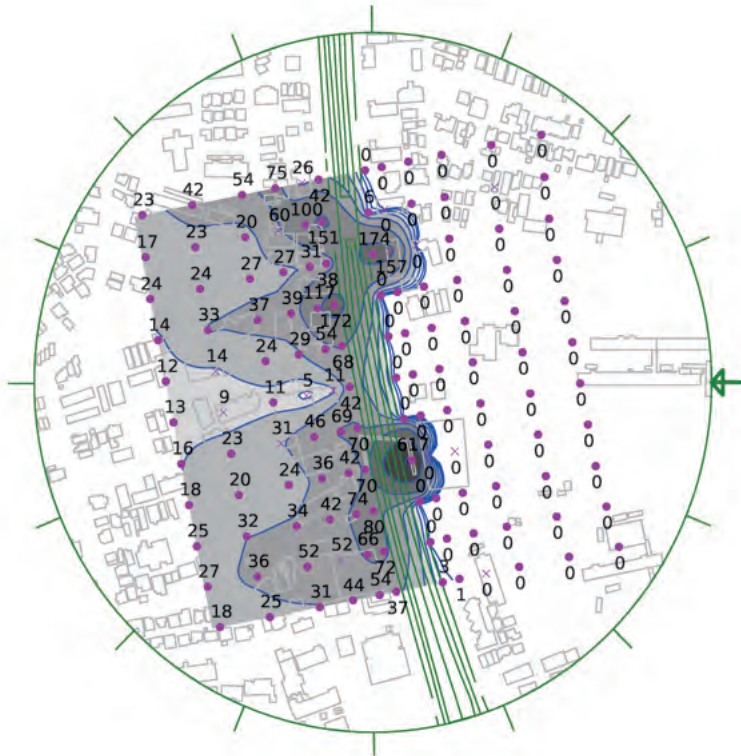
There are, however, cases where MCAD could be meaningful. For example, in epidemiological studies with a large number of samples, statistical performance matters and a small number of erroneous predictions are acceptable although systematic bias needs to be made as small as possible. This is one reason why conventional Gaussian-plume models continue to be employed in epidemiological studies or environmental assessment although lack of feasible alternative may be another reason.

Here, we compare the proposed model with a Gaussian-plume model in terms of statistical measures. The following quantities discussed by Chang & Hanna (2004) are considered.

Fractional Bias:	$FB = \frac{\overline{C_e - C_m}}{0.5(\overline{C_e + C_m})},$
Geometric Mean Bias:	$MG = \exp(\overline{\ln C_e - \ln C_m}),$
Normalized Mean Square Error:	$NMSE = \frac{\overline{(C_e - C_m)^2}}{\overline{C_e C_m}},$
Geometric Variance:	$VG = \exp(\overline{(\ln C_m - \ln C_e)^2}),$
Factor of Two:	$FAC2 = \text{Probability of } \left\{ 0.5 \leq \frac{C_m}{C_e} \leq 2 \right\},$
Correlation coefficient:	$R = \frac{\overline{(C_m - \overline{C_m})(C_e - \overline{C_e})}}{\sqrt{\overline{(C_m - \overline{C_m})^2}} \sqrt{\overline{(C_e - \overline{C_e})^2}}},$

where C_e and C_m denote the experimental and the MCAD calculation values, respectively, and the overbars indicate averages over all the measurement points. FB and MG represent systematic bias, and NMSE and VG involve both systematic bias and random scatter. A perfect model has $FB = NMSE = 0$ and $MG = VG = FAC2 = R = 1$. The logarithmic measures MG and VG are suited for cases where concentration varies by many orders of magnitude. Because zero values contribute unduly to MG and VG (zero values at points upwind of a source make $\ln C$ minus infinity), concentration (when normalized by the emission rate) smaller than unity is forced into unity in calculating MG and VG, *i.e.* low concentration points are excluded from the evaluation. Chang & Hanna (2004) suggested that a 'good' performing model should satisfy the

Experiment



MCAD

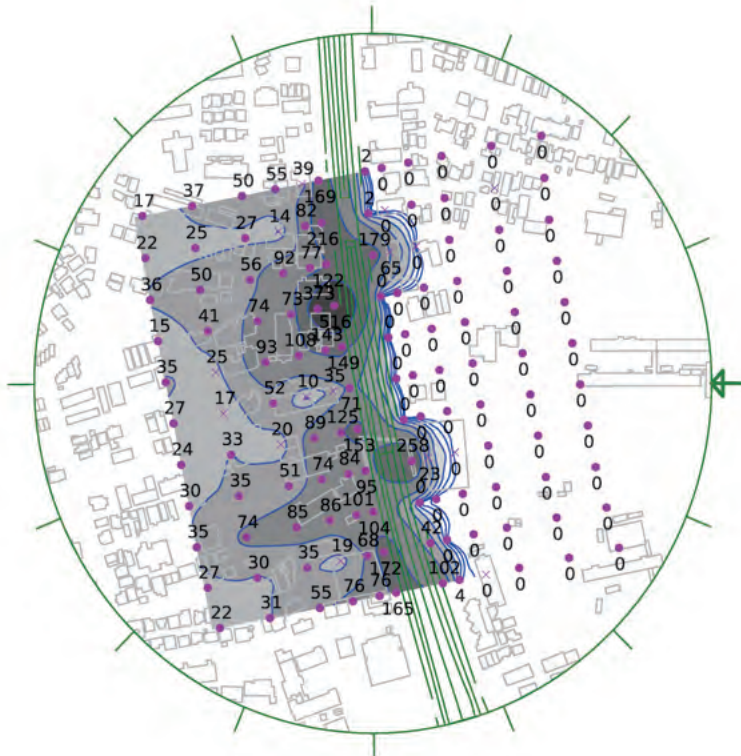
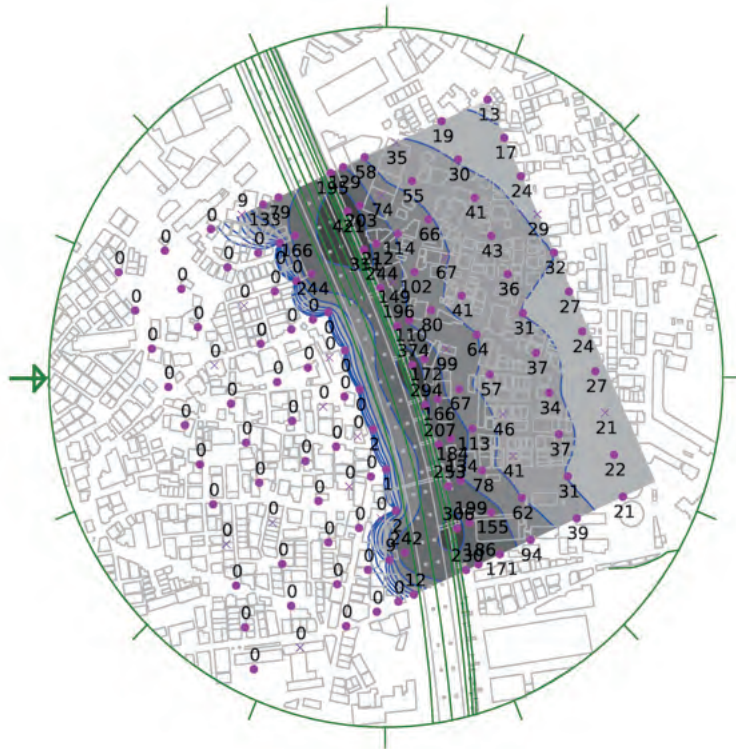


Figure 3.17 (continued) Itaka

Experiment



MCAD

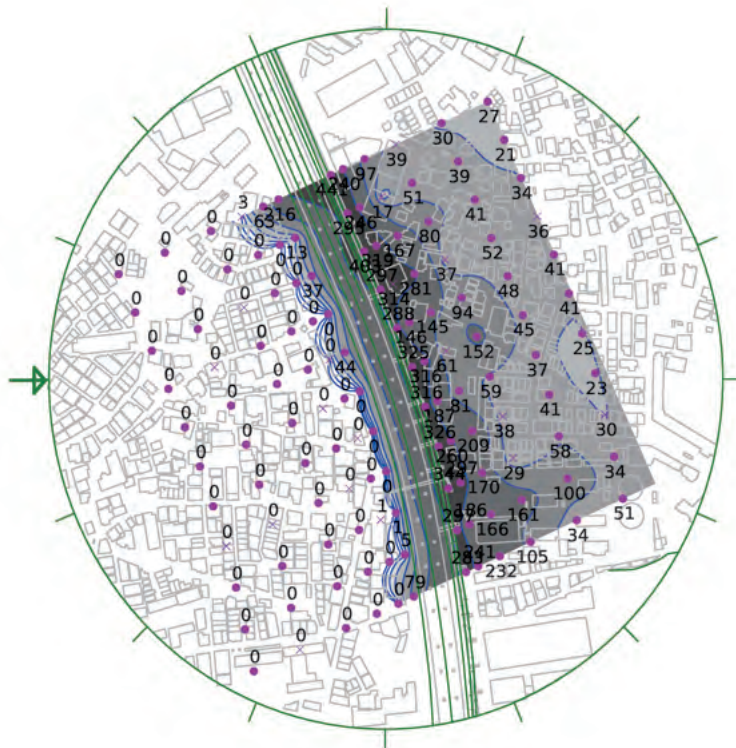
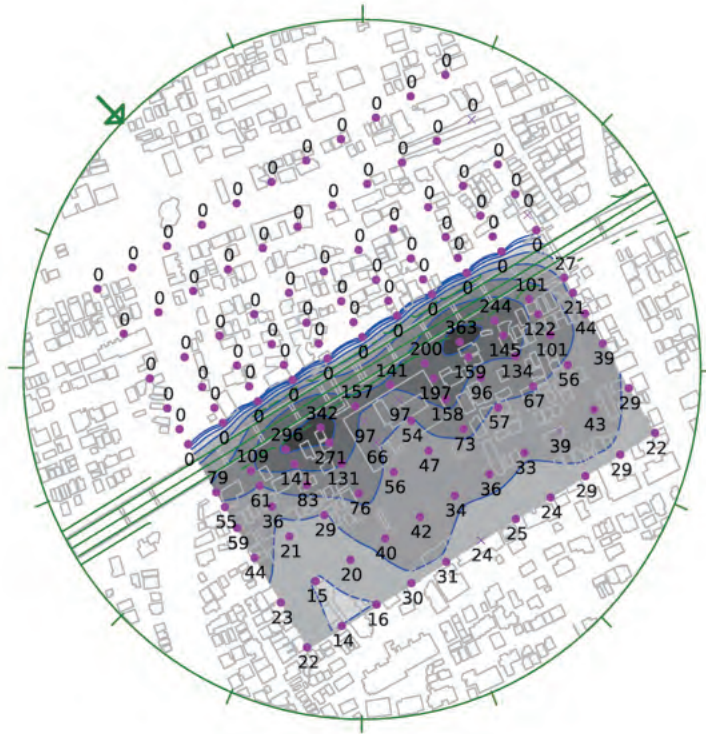


Figure 3.17 (continued) Kadoma

Experiment



MCAD

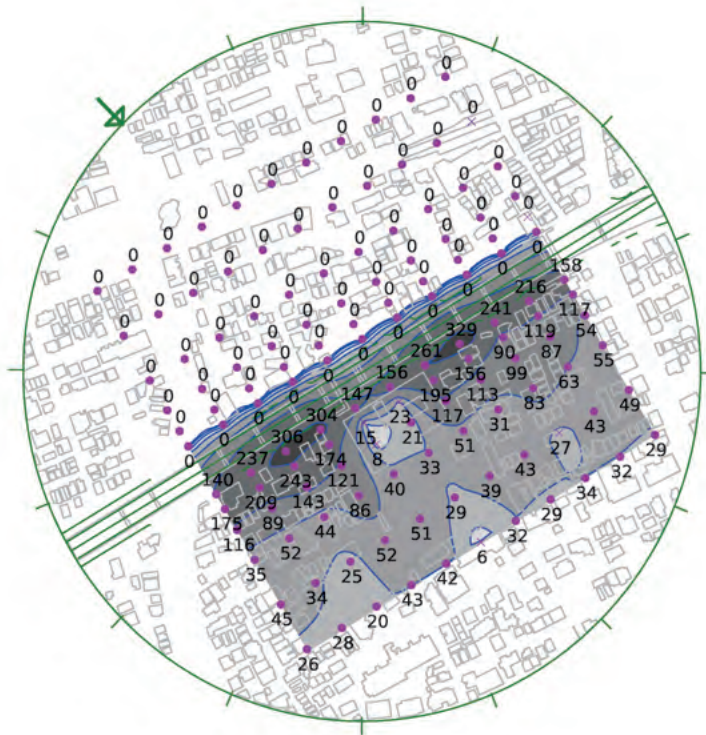
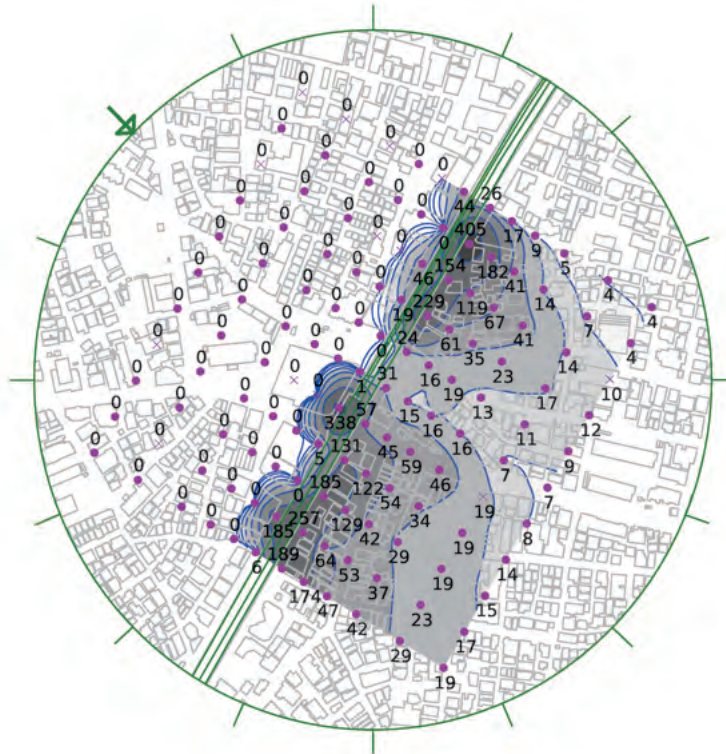


Figure 3.17 (continued) Ashiya

Experiment



MCAD

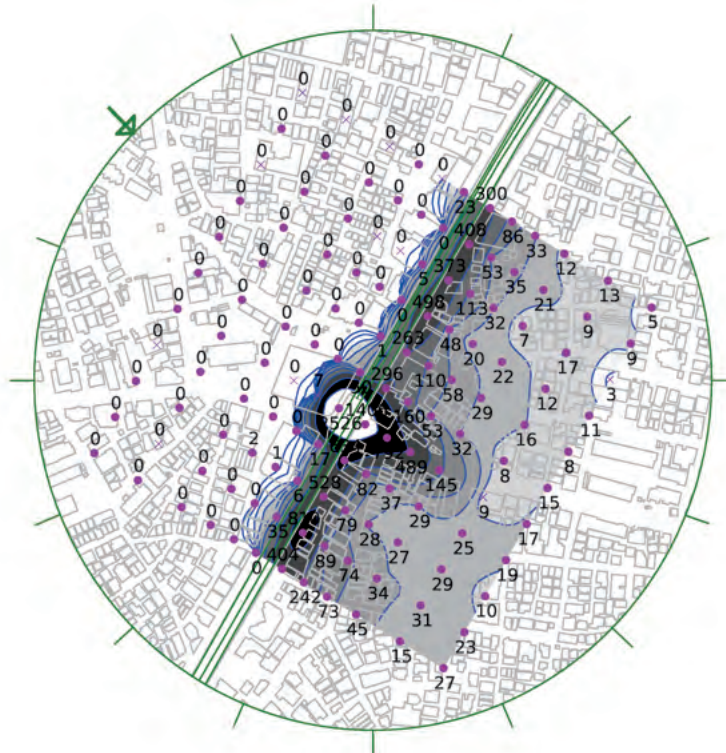


Figure 3.17 (continued) Setagayapost. The white region surrounded by gray shades has higher concentration than the gray region.

following conditions.

$$|\text{FB}| < 0.3, \quad 0.7 < \text{MG} < 1.3, \quad \text{NMSE} < 4, \quad \text{VG} < 1.6, \quad \text{FAC2} > 0.5. \quad (3.2)$$

Note that Chang and Hanna suggested this criterion for prediction of relatively long-range field diffusion experiments where weather condition is not as definitely known as in wind-tunnel experiments. Hence, if the plume widths are considerably larger than the surface obstacles as is the case with long-range diffusion problems, a ‘good’ performing model should satisfy (3.2) with a wide margin when applied to wind-tunnel experiments. However, for a short-range problem where the plume widths are comparable to the surface obstacles, the criteria (3.2) may be too severe.

The Gaussian-plume model employed here follows the guideline by the Japanese Environmental Agency (2000). The concentration C is calculated by

$$C = \frac{Q}{2\pi\sigma_y\sigma_zU_{10}} \exp\left(-\frac{y^2}{2\sigma_y^2}\right) \left\{ \exp\left(-\frac{(z-H_e)^2}{2\sigma_z^2}\right) + \exp\left(-\frac{(z+H_e)^2}{2\sigma_z^2}\right) \right\}, \quad (3.3)$$

where Q is the emission rate, U_{10} the wind speed at $z = 10$ m (real scale), H_e is the height of the source, and σ_y and σ_z are the horizontal and vertical plume widths, respectively. The plume widths are defined as initial values plus the values given as a function of downwind distance (Briggs 1973). The vertical initial plume width σ_{z0} is set following the guideline (Japan Environment Agency 2000) as

$$\sigma_{z0} = \begin{cases} 1.5 \text{ m} & \text{surface road,} \\ 4.0 \text{ m} & \text{elevated road,} \end{cases}$$

except for Itaka where σ_{z0} was set 10 m in order to make the prediction close to the experimental result. This adjustment was necessitated by the almost continuous noise barriers along the road in Itaka. For Ashiya, another site with noise barriers, such an adjustment was not necessary because there were many openings at junctions with side streets. For real roads, σ_{y0} is set equal to half the road width, but in the current case with narrow pipes as sources and almost uniform emission profile, we set $\sigma_{y0} = 0$. A calculation result corresponding to Fig. 3.17(a) is shown in Fig. 3.18. Because buildings have no effect on the concentration field, the contours are parallel to the road.

The statistical quantities are calculated with all the 220 measurement points in the wind-tunnel model (132 points at $z = 6$ mm shown in Fig. 3.17 and 88 points at $z = 40, 80, 160$ mm) for 6 wind directions for each road at each site. Note that the vertical profiles were measured at $z = 6, 40$ and 80 mm along the 4th row from the trunk road, and at $z = 6, 80,$ and 160 mm along the 6th row from the trunk road. Fig. 3.19 shows the result of linear measures FB, NMSE, FAC2 and R for surface-road emission in Hachimanyama (cf. Fig. 3.17a and Fig. 3.18 for the wind-direction ESE). The dashed lines represent the bounds of the criteria (3.2). Despite the expected ease of satisfying the criteria, there are points outside the criterion bounds. We also observe that the performance

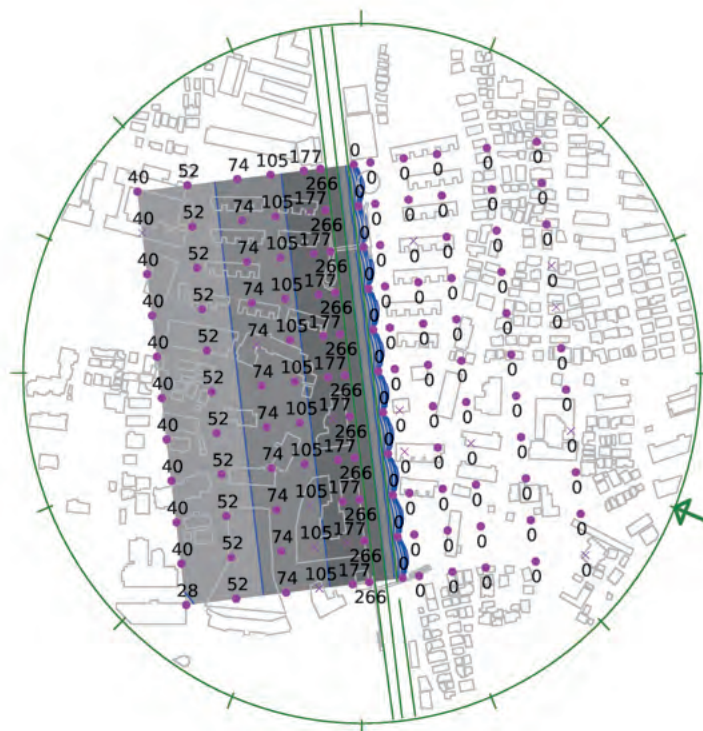


Figure 3.18: Concentration contours at $z = 6$ mm for Hachimanyama calculated by a Gaussian-plume model.

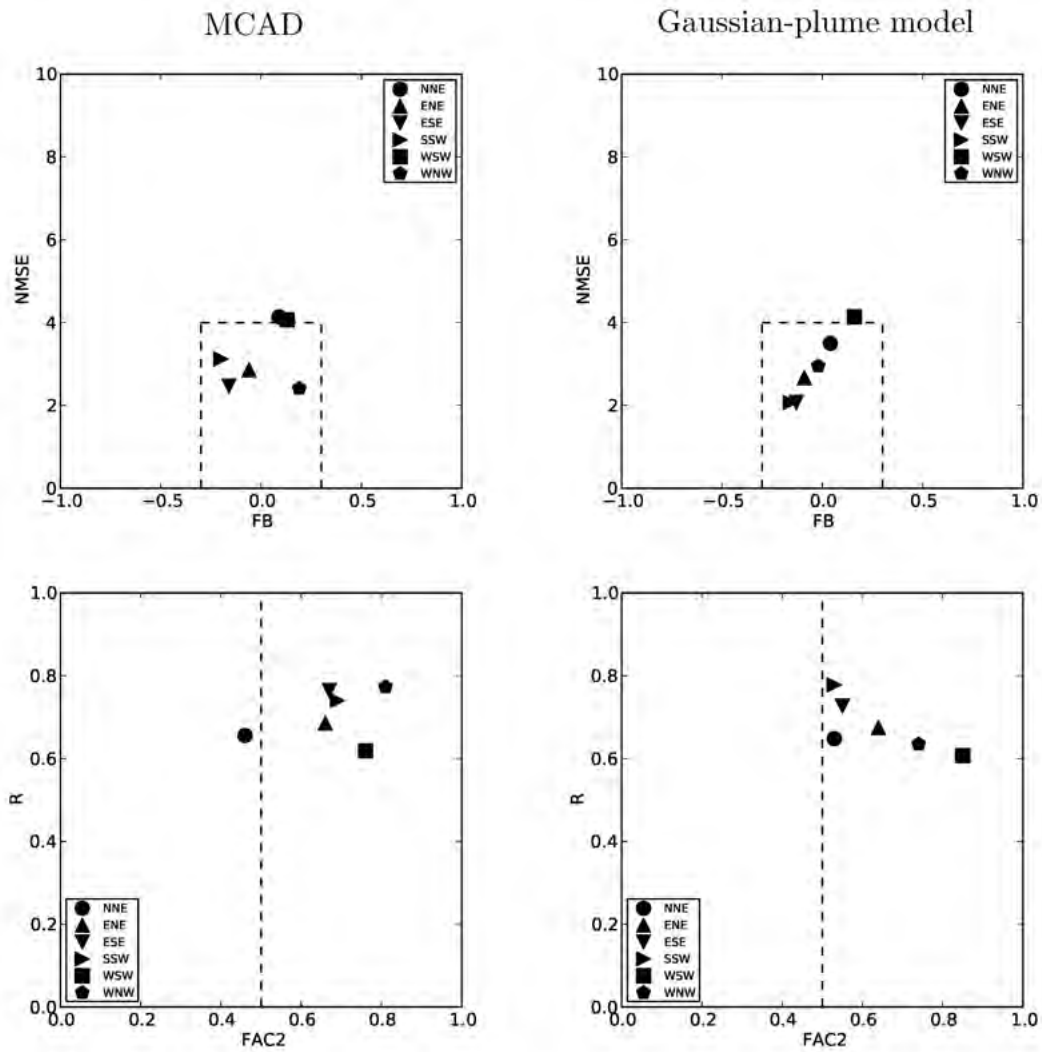


Figure 3.19: Linear statistical measures evaluated for surface-road emission of Hachimanyama.

of MCAD and that of the Gaussian-plume model are not much different. With varied degree of criterion satisfaction, similar results are true to all the other cases. It should, however, be emphasized that MCAD performs reasonably well without the intentional adjustment of σ_{z0} in Itaka for the Gaussian-plume model. Such an adjustment is often done in applying Gaussian-plume models in the real world; MCAD here is compared with the optimized Gaussian-plume model.

The linear measures, however, over-evaluate the discrepancies at high concentration. Atmospheric diffusion as represented by the Gaussian-plume model (3.3) generates exponentially decaying concentration in the downwind and lateral directions. Hence, in evaluating the performance near the road, logarithmic measures MG and VG are more suitable.

Fig. 3.20 shows MG and VG for all the sites with surface-road emission.

Evaluation by MG and VG turns out to be stringent; in most cases, the criteria (3.2) are not satisfied particularly with respect to VG. Especially, the performance for Setagayapost is very poor (note that the VG scale is logarithmic). This is due to the roadside tall buildings that form street canyons as discussed in §3.4. Although both MCAD and the Gaussian-plume model perform poorly, we observe that MCAD is distinctly better than the Gaussian-plume model, reflecting the ability of MCAD to reproduce the complex concentration distribution near the trunk roads as contrasted in Fig. 3.17 and Fig. 3.18. For elevated roads (not shown), the difference between MCAD and the Gaussian-plume model is not so clear because the effect of roadside buildings is less significant.

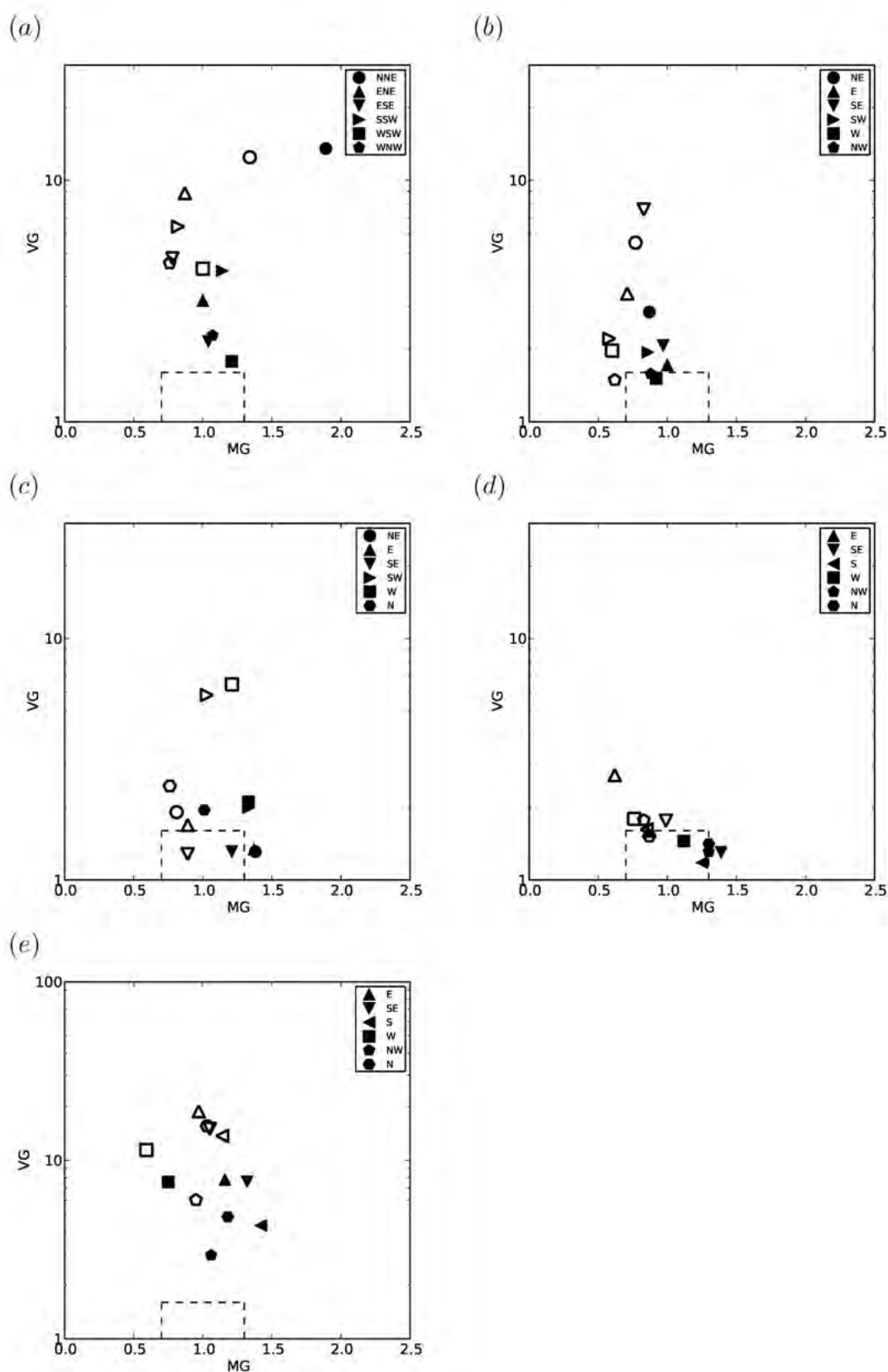


Figure 3.20: Logarithmic statistical measures evaluated for surface-road emission: Hachimanyama (a), Itaka (b), Kadoma (c), Ashiya (d) and Setagayapost (e). Filled markers represent MCAD and open ones the Gaussian-plume model.

Chapter 4

Extension to real-world situations

4.1 Hourly average concentration

4.1.1 Introduction

Variability of wind direction has substantial effects on air-pollutant concentration (Pasquill, 1974). Air pollutant concentration is usually reported as averages for 30–60 min because salient factors such as pollutant emission rate, wind condition, or atmospheric stability varies on similar timescales. Over such an averaging period, wind-direction fluctuations of timescale from about 10 min to a few hours, often called meandering, disperse the pollutants considerably in the horizontal direction.

This dispersing effect poses a problem on the side of pollution prediction. Widely accepted pollution prediction models for spatial scales up to a few kilometers are usually based on field diffusion experiments whose averaging period is at most 10 min (there are models based on longer-period observations, but they cannot be said to have been validated well with practical examples). For example, the Pasquill–Gifford–Turner chart, or its analytical representation the Briggs formulas, is for 3-min average, and the predicted horizontal width σ_y of the pollutant plume is considerably smaller than that expected of a 30–60-min averaged plume. The problem becomes more serious for lower wind speed conditions because the relative strength of the meandering component becomes larger.

Conventional prediction models solve this problem by separating the effect of the meandering component from that of faster fluctuations. For example, a regulatory model in Japan (Japan Environment Agency, 2000) calculates hourly-averaged concentration as the average of the results of the Briggs formula over a $2\pi/16$ -radian sector centered at the 10-min averaged wind direction for windy conditions ($U_{10} \geq 1$ m s, where U_{10} is the wind speed at 10 m above the ground). For weak-wind conditions ($U_{10} < 1$ m s), the above Japanese model applies the Puff formula with empirically determined parameters. For another example, ADMS (Cambridge Environmental Research Consultants) calculates the horizontal plume width σ_y as the root-mean-square of the widths due to the local turbulence (faster fluctuations) and the meandering. ADMS excludes low-wind conditions ($U_{10} < 0.75$ m s) from the model's applicable range.

Recent building-resolving prediction models are subject to the same problem. For urban areas with complex emission sources and many residences, prediction models that solve relevant dynamical equations numerically in building-resolving meshes have been employed by many researchers (e.g. Eichhorn, 1989; Yoshikawa *et al.*, 2003; Blocken *et al.*, 2008). The scope of these models, however, is currently limited to the effect of small-scale turbulence of at most a few-minute timescale. To predict longer-period average concentrations, which is necessary for model validation with field data, weighted sum of the predicted concentrations for neighboring wind directions is often adopted. The weights are usually determined based on the available wind observation data and gross estimate of the wind-direction fluctuation. In Japan, a frequently employed weight distribution is 1:2:1 for neighboring 16-point compass directions observed

routinely as averages for 10 minutes once an hour. However, with different wind-observation protocols in different countries and in different focus studies, it is not clear how long an average time or how large an angle resolution are appropriate for proper prediction.

This chapter presents a method for predicting both the horizontal plume width σ_y and the horizontal eddy diffusivity K_y ; σ_y is to be compared with conventional model predictions and K_y is to be used above the urban canopy layer in building-resolving prediction models such as MCAD. Of various ways to tackle the meandering problem (e.g. Sharan & Yadav, 1998; Oettl *et al.*, 2001; Oettl *et al.*, 2005), we adopt the classical diffusion theory using velocity fluctuation spectrum. A novel feature is the form of the velocity fluctuation spectrum S_v conceived from the results of low-frequency field observations. It is shown that, without the low-frequency components, the calculated σ_y becomes considerably smaller than that predicted by conventional models. With the classical diffusion theory, concentrations can be predicted as arbitrary-period average for arbitrary wind speed in a seamless manner without introducing separate formulas for particular ranges of averaging period or wind speed.

The scope is limited to neutral stability and dispersion distances up to a few kilometers. The spectral procedure with the derived K_y is intended to be applied in built-up urban areas. In such areas, the effective stability is neutral for most insolation conditions and the spatial length scale is at most a few kilometers. In rural areas where stability condition varies more widely or the concerned length scale is much longer, conventional prediction models work well and there does not seem much need for additional development except for special cases such as near-source prediction, for which LSM provides a solution.

The outline of this section is as follows. §4.1.2 reviews field observations of velocity fluctuations and spectra at low-wind speed or low frequency. §4.1.3 explains the proposed form of the velocity spectrum and the derivations of relevant quantities. §4.1.4 compares the prediction of the spectral method with those by conventional models or field observations. Summary and discussion are presented in §4.1.5.

4.1.2 Review of field observations

Cross-wind velocity fluctuation at low wind speed

In the following, the mean wind speed is denoted by U and the fluctuating components by u and v in the alongwind and crosswind directions, respectively.

At low wind speed, meandering component has a dominant effect on the cross-wind velocity fluctuation $\sigma_v = \sqrt{v'^2}$. Velocity fluctuation has often been studied in the form of wind-direction fluctuation σ_v/U where U is the mean wind speed. Note that U is either the scalar or vector mean value associated with cup/propeller or sonic anemometers, respectively. The scalar mean is denoted by U_a and the vector mean by U_e .¹ In the following, when the averaging method

¹ $U_a = \sqrt{u'^2 + v'^2}$, $U_e = \sqrt{u'^2 + v'^2}$, where $u' = U + u$ and $v' = V + v$ are the instantaneous velocity components.

is unknown or irrelevant, U is shown without a subscript. Note that, for high wind speed, $U_a \sim U_e$, but for small wind speed, $U_a > U_e$ (cf. Castans & Barquero, 1994).

Kristensen & Panofsky (1976) explained observed σ_v/U by the similarity formula. They used the wind data at heights $z = 11$ and 76 m on the tower at Risø in Denmark. Selecting winds coming from the ocean under neutral stability, they found that the 10-min average value agreed well with the similarity formula

$$\frac{\sigma_v}{U_a} = \frac{\sigma_v}{\frac{u_*}{\kappa} \ln \frac{z}{z_0}} = \frac{0.8}{\ln \frac{z}{z_0}}, \quad (4.1)$$

where u_* is the friction velocity, $\kappa = 0.4$ is the von Karman constant, z_0 is the roughness height, and the constant 0.8 is determined by $\sigma_v/u_* = 2$, the neutral stability limit of the similarity formula by Panofsky *et al.* (1977).

As Kristensen & Panofsky (1976) themselves note, observation at low wind speed do not agree with the similarity formula (4.1). For example, Davies & Thomson (1999) found

$$\frac{\sigma_v}{U_e} = \sqrt{\left(\frac{0.8}{\ln \frac{z}{z_0}}\right)^2 + \left(\frac{0.5}{U_e}\right)^2}, \quad (4.2)$$

where U_e needs to be converted into the unit m s^{-1} . They used observation data under stable conditions at the Meteorological Research Unit, Cardington, UK, over a 35-month period. One-hour average values were fitted by equation (4.2) up to $U_e \sim 14 \text{ m s}^{-1}$. The first term in the square root is the similarity form (4.1) and the second term means that σ_v tends to 0.5 m s^{-1} as U_e becomes small. Expressions vary among authors, but the qualitative feature is the same: as U tends to zero, σ_v tends to some non-zero constant, and σ_v/U becomes large unlike equation (4.1) which predicts constant σ_v/U at a given height. Table 4.1 lists the results by various authors.

Table 4.1: Field observation results of σ_v at low wind speed. All units are in SI. In stability, S denotes stable and U unstable. In U range, U_a and U_e indicate the definition of the mean wind speed adopted in each study. U range is shown only for the studies in which the U range for determining σ_v was explicitly defined; for other studies, σ_v was determined from the behavior of σ_v/U as $U \rightarrow 0$.

reference	site	z	stability	U range	z_0	σ_v
Joffe & Laurila (1988)	Bothnian Bay Finland	10	S/U	$U_a \leq 5$	$(1-5) \times 10^{-4}$	0.32
Davies & Thomson (1999)	Cardington UK	21	S	U_e	0.01	≥ 0.5
Leahey <i>et al.</i> (1994)	Kathryn Canada	10	S	$U_e \leq 3$	0.01–0.04	0.29–0.43 ^a
Smith & Abbott (1961)	Porton UK	16	S	U_a	0.03	0.3 ^b
Hanna (1983)	Cinder Cone Butte USA	40	S	–	0.1 ^c	0.5
Agarwal <i>et al.</i> (1995)	South Delhi India	4	S/U	$U_e < 1$	0.78	0.05–0.3
Hanna (1981 <i>a</i>)	Anderson Springs USA	10	S	U_a	1	1.0
Papadopoulos <i>et al.</i> (1992)	Athens Greece	42	S/U	U_a	1.1–1.6	0.6–1.0 ^d

^a The averaging time was 30 min. The reported σ_v was converted to one-hour average value using $\sigma_v \propto T_A^{0.2}$ (Panofsky, 1988).

^b analyzed by Pasquill (1974).

^c an estimate by Apsley & Castro (1997).

^d estimated from Fig. 2 of Papadopoulos *et al.* (1992).

The cause of constant σ_v at small U has not been well understood. Although many authors attribute it to meandering motions under stable stratification, constant σ_v at small U has been observed both under stable and unstable conditions (Kristensen & Panofsky, 1976; Joffre & Laurila, 1988; Papadopoulos *et al.*, 1992; Agarwal *et al.*, 1995). Some differences by stability conditions are noted by these authors, but they are not consistent and the general characteristics of the limiting value has not been clarified. Note that, in Table 4.1, we recognize a gross trend that σ_v at small U increases with z_0 .

It is emphasized here that non-zero σ_v at small U is inconsistent with the conventional similarity formulas that assume $\sigma_v \rightarrow 0$ as $u_* \rightarrow 0$ (*e.g.* Panofsky *et al.*, 1977; Kaimal *et al.*, 1972; Al-Jiboori *et al.*, 2002). Such similarity formulas should be regarded valid only for sufficiently high wind speed, say, $U_{10} \gtrsim 1 \text{ m s}^{-1}$.

Velocity spectrum The frequency-multiplied horizontal velocity spectrum near the ground has three characteristic peaks (Stull, 1988, p32). Note that, unless otherwise mentioned, when we refer to velocity spectrum, it means the spectral energy density multiplied by frequency. The largest peak near 100-h cycle is associated with the passage of fronts and weather systems. A small peak on the high-frequency foothill of the largest peak is associated with diurnal variations: strong wind in the afternoon and weak wind at night. Another peak around 10 sec – 10 min is due to mesoscale turbulent motions. The properties of this mesoscale spectral peak is well understood, and empirical formulas of the spectrum are established for various atmospheric stability conditions. The relatively low energy portion between the diurnal and the mesoscale turbulence peaks is called the spectral gap.

Intuitively, the mesoscale turbulence peak seems most important for dispersion prediction of 30–60-min average up to a few kilometers. However, as will be shown later, the component from the foothill of the diurnal peak to the spectral gap has a dominant role in pollutant dispersion. Particularly at low wind speed, this component does not decay in proportion to the mean wind speed (Anfossi *et al.* 2005) and becomes further dominant. Despite its importance, this ‘low-frequency’ spectrum has not been well understood both because reliable long-term measurement is difficult and because it is associated with various types of complex atmospheric motions such as gravity waves and natural convections. In the following, we review recent findings on the low-frequency spectrum. Since the observations are at fixed locations, the spectra considered here are Eulerian ones denoted by superscript E.

Olesen *et al.* (1984) reviewing previous measurements in stable conditions mentions, “... the horizontal spectra exhibit a low-frequency peak around 10^{-3} Hz ,” but also mention, referring to an unpublished work, “... their spectra continue to increase for decreasing frequencies down to the lowest frequency, 10^{-4} Hz .” Most of the cited authors in Olesen *et al.* considered gravity waves as the main agent behind the low-frequency spectra. In analogy to two-dimensional

turbulence spectrum, Olesen *et al.* proposed a spectral form

$$\frac{f S^E(f)}{u_*^2} \propto \frac{z}{L} \varphi_h f^{-2}, \quad (4.3)$$

where f is the non-dimensional frequency defined by

$$f = n \frac{z}{U}, \quad (4.4)$$

where n is the dimensional frequency, and φ_h is the non-dimensional temperature gradient. Although the tested frequency range was rather narrow ($2 \times 10^{-3} \lesssim f \lesssim 5 \times 10^{-3}$), they found reasonably good agreement with the observed stable horizontal spectra in Kansas and Minnesota.

Richards *et al.* (2000) measured velocity spectra under neutral stability condition. The measurement site was Silsoe Research Institute in Bedfordshire, UK with $z_0 = 0.01$ m. The measurement height was $z = 0.115$ – 10 m and the measurement duration was 20 min. The wind speed U was typically over 3 m s^{-1} . They found that the low-frequency component scales differently from the mesoscale turbulence component. While the mesoscale turbulence component collapsed to a universal form

$$\frac{f S^E(f)}{u_*^2} = \text{func}(f), \quad (4.5)$$

the observed low-frequency component was best described by

$$\frac{f_1 S(f_1)}{U^2} = \text{func}(f_1), \quad (4.6)$$

where $f_1 = n z_0 / u_*$. Hence, the amplitude of the low-frequency fluctuation is proportional to the local mean wind speed $U(z)$ and the frequency is independent of the vertical mixing length $\sim z$, implying that the associated motion is vertically coherent. As an optimal fit to their data for the alongwind component S_u^E , they proposed

$$\frac{f S_u^E(f)}{u_*^2} = \frac{f}{C' \left(\frac{u_*}{U}\right)^3 \frac{z}{z_0} + D' f^\alpha + E' f^{5/3}}, \quad (4.7)$$

where C' , D' , E' and α are constants. This formula, though expressing the low-frequency behavior correctly, should be regarded as a fit to the observation under their particular measurement conditions.

Anfossi *et al.* (2005) measured spectrum at Graz, Austria and at Tisby, about 45 km west of Uppsala, Sweden. The measurement height was 10 m at Graz and 6.8 m at Tisby. The measurement time was 60 min. Both sites had frequent occurrence of weak wind conditions. For $U < 3 \text{ m s}^{-1}$, they observed low-frequency ‘plateau’ both for stable and unstable conditions toward the lower end of their measured frequency range; the magnitude and the location of the

plateau were independent of stability whereas the mesoscale turbulence spectrum was larger for unstable conditions than for stable conditions (see Fig. 4.1b). Although they comment on the persistence of low-frequency spectral magnitude at low U , their data seem merely to follow the empirical spectral form which, in the dimensional form, depends on U like $\sim U$ at low frequencies and $\sim U^{8/3}$ at high frequencies (cf. equation (4.8)). For $U < 3 \text{ m s}^{-1}$, they found that the Eulerian autocorrelation function had negative lobes around $400 \sim 1200 \text{ s}$ for both stable and unstable conditions, which is at odds with previous studies that attributed negative lobes to gravity waves in stable stratification.

4.1.3 Proposed method

Model spectrum

Based on the review of σ_v and spectrum observations, we construct a model spectrum that reproduces non-zero σ_v as U becomes small and extends to sufficiently low frequencies. For brevity, the mesoscale and the inertial-subrange turbulence spectrum is called high-frequency spectrum and that for frequencies in and below the spectral gap low-frequency spectrum. Eulerian spectrum observed at a fixed point is considered.

The high-frequency spectrum has been well-understood, and the empirical formula for neutral stability conditions are given by Kaimal & Finnigan (1994) as

$$\frac{f S_v^E(f)}{u_*^2} = \frac{17f}{(1 + 9.5f)^{5/3}}. \quad (4.8)$$

There are other variations of the spectral formula (Olesen *et al.*, 1984; Tieleman, 1995), but in dispersion prediction where the integrals of the spectra are used, minor differences in the spectral shape does not matter much.

Compared to the high-frequency spectrum, the low-frequency part has not been understood well. In predicting the pollutant concentration as hourly average over a few kilometers, the most relevant fluctuation timescale is $O(10^3)$ s, or $n = O(10^{-3})$ Hz, where authors cited by Olesen *et al.* (1984) observed spectral peaks. Thus, proper modeling of the low-frequency spectrum is critical in pollution prediction. In this frequency region, the relevant motions include internal gravity waves and natural convection.

Internal gravity waves are sustained by stable stratification. Wave spectrum is established by nonlinear interactions of internal gravity waves and collapse of vortical motions. In the stratosphere where stable stratification is persistent and where there are few obstacles, the wave spectral density S^E is observed to follow f^{-3} . This behavior agrees with the dimensional analysis of Lumley (1964) who derived

$$E(k) \sim N^2 k^{-3} \quad \text{for } k \ll k_b, \quad (4.9)$$

where $E(k)$ is the energy density at wavenumber k , N is the buoyancy frequency and $k_b = N^{3/2} \epsilon^{-1/2}$ is the Ozmidov wavenumber where ϵ is the turbulence energy dissipation rate.

Natural convection have various scales depending on the heating condition of the ground. When the atmosphere is unstable, the spectral gap is filled to some uncertain extent by the convective motions such that the peak of the high-frequency spectrum becomes indistinguishable (Kaimal & Finnigan, 1994; Gjerstad *et al.*, 1995; Peltier *et al.*, 1996). At low frequencies $\sim O(10^{-3})$ Hz, however, Anfossi *et al.* (2005) observed similar magnitude of spectral density for both stable and unstable conditions. Hence, the difference due to stability should become small at low frequencies.

We regard neutral condition as an ensemble average state of weakly stable and weakly unstable conditions. The above considerations suggest that, under neutral conditions, the high-frequency tail of the low-frequency spectrum $fS_{v,\text{low}}^E(f)$ behaves like f^{-p} ($p \lesssim 2$). Since this frequency region overlaps with the low-frequency tail of the high-frequency spectrum where $fS_{v,\text{high}}^E(f)$ behaves like f , it is sensible to set $p = 2$. Hence, the frequency dependence is the same as that in equation (4.3) from which only this frequency dependence is adopted in the proposed spectrum.

Defining the amplitude of the low-frequency spectrum is not trivial since the low-frequency spectrum keeps increasing toward the diurnal and weather-system timescales. The spectral form (4.7) by Richards *et al.* (2000) is based on estimating the value, or their constant C' , where the extrapolation of the low-frequency side of the low-frequency spectrum approaches as $f \rightarrow 0$. By this method, it is difficult to relate the constant C' to some physical quantity. Instead, we imagine a hypothetical low-frequency spectrum without the diurnal and the weather-system contributions, thus consisting only of the internal-wave and natural-convection contributions. Then, we can assign a finite magnitude to their total energy. In analogy to the high-frequency spectrum which decreases on the low-frequency side, we postulate a form

$$f_1 S_{1,v,\text{low}}^E(f_1) = \frac{fD}{(1 + b_1 f_1)^3}, \quad (4.10)$$

where dependence on f_1 follows Richards *et al.* (2000). The spectrum has a peak at $f_1 = 1/2b_1$ and integrated energy $D/2b_1$. The artificial removal of the further lower frequency component does not affect the concentration prediction up to a few kilometers since the pollutant traveling time is much less than the inverse of the frequency at the spectral peak of the diurnal variation and, in the calculation of the eddy diffusivity, the part on the low-frequency side of the low-frequency spectrum (4.10) makes negligible contribution.

The coefficient D must reflect the findings by Richards *et al.* (2000) that the magnitude of the low-frequency motions scale as the local mean wind speed $U(z)$ and is independent of the local mixing length. Therefore, we first set

$$D = CU^2. \quad (4.11)$$

Together with the high-frequency part, we observe that the spectral density is proportional to U^2 , and hence $\sigma_v^2 = \int_0^\infty S_v^E(f) df \rightarrow 0$ as $U \rightarrow 0$. In order to

realize constant σ_v as $U \rightarrow 0$ as reviewed in §4.1.2, we add a constant to D , *i.e.*

$$D = B + CU^2. \quad (4.12)$$

Allowing different timescales for the U -dependent and U -independent parts, the spectrum (4.10) becomes

$$f_1 S_{1,v,\text{low}}^E(f_1) = \frac{Bf_1}{(1 + b_1 f_1)^3} + \frac{CU^2 f_1}{(1 + c_1 f_1)^3}. \quad (4.13)$$

This separation of low-frequency components is probably the most questionable part of the spectrum construction. More sophisticated construction, however, does not seem ready (at least, with the author's capacity) with the current knowledge of low-frequency and low-wind-speed behaviors. The above form is proposed as the simplest one that can be fit well to the reported spectra (see §4.1.3). In terms of f , this form is written as

$$f S_{v,\text{low}}^E(f) = f_1 S_{1,v,\text{low}}^E(f_1) = \frac{\frac{U}{z} \frac{z_0}{u_*} B f}{(1 + b f)^3} + \frac{\frac{U}{z} \frac{z_0}{u_*} C U^2 f}{(1 + c f)^3}, \quad (4.14)$$

where

$$b = b_1 \frac{U}{z} \frac{z_0}{u_*}, \quad c = c_1 \frac{U}{z} \frac{z_0}{u_*}. \quad (4.15)$$

We call the first term on the right-hand side as the 'residual' component.

The addition of a constant magnitude could be done to the high-frequency spectrum, but in view of the observation of Anfossi *et al.* (2005) who found persistent low-frequency spectral magnitude at weak wind conditions, it is appropriate to attribute the residual fluctuations exclusively to the low-frequency spectrum.

There are various ways to combine the low-frequency and the high-frequency spectra, such as simple summation, root-mean-square averaging, or reciprocal summation, but conforming to the σ_v formula (4.2), we opt for a simple summation. Hence, our proposed model spectrum becomes

$$f S_v^E(f) = \frac{\frac{U}{z} \frac{z_0}{u_*} B f}{(1 + b f)^3} + \frac{\frac{U}{z} \frac{z_0}{u_*} C U^2 f}{(1 + c f)^3} + \frac{A f u_*^2}{(1 + a f)^{5/3}}, \quad (4.16)$$

where $A = 17$ and $a = 9.5$.

The spectrum (4.16) does not produce negative lobes of the Eulerian autocorrelation function observed by Anfossi *et al.* (2005) at low wind speeds. This is because the proposed f^{-2} spectrum is of the atmosphere saturated with a wide range of frequencies of internal gravity waves whereas the autocorrelation functions observed by Anfossi *et al.* (2005) are likely to be associated with gravity waves generated at particular length scales of the relatively ragged terrain around their observation sites.

It may appear nonsense to define a residual component under neutral stability condition because low wind speed usually occurs under very stable or very

unstable conditions. However, this ‘very stable’ or ‘very unstable’ condition is based on rural terrain whereas neutral stability in this chapter implies that in urban areas where mechanical mixing by buildings renders effective neutrality for a wide range of insolation conditions. Because the timescale of such mechanical mixing is at most a few minutes, the residual component assigned to relatively low frequencies is not influenced by the presence of buildings. The cause of the residual component is presumably the fluctuations due to large-scale terrain variability in elevation or roughness, and hence the residual component can be non-zero when the urban roughness sublayer is neutrally stable but the atmosphere over more than a few kilometer length scale is not neutral.

Horizontal plume width

Horizontal plume width σ_y and relevant quantities are derived from the model spectrum. In the horizontal direction, it may be assumed that the turbulent fluctuation is homogeneous. Then, by the classical diffusion theory (Pasquill, 1974, p128), the crosswind spread σ_y of the plume from a continuous point emission source is given by

$$\sigma_y^2(t, T_A) = t^2 \int_0^\infty S_v^L(f) \frac{\sin^2 \pi f \hat{t}}{(\pi f \hat{t})^2} \left\{ 1 - \frac{\sin^2(\pi f \hat{T}_A)}{(\pi f \hat{T}_A)^2} \right\} df, \quad (4.17)$$

where t is the mean travel time from the source, T_A is the observation time, and $S_v^L(f)$ is the Lagrangian spectral density explained below. The normalized times \hat{t} and \hat{T}_A are defined by

$$\frac{t}{\hat{t}} = \frac{T_A}{\hat{T}_A} = \frac{z}{U}.$$

The wind speed U is assumed to obey the log law

$$U = \frac{u_*}{\kappa} \ln \frac{z - z_d}{z_0}, \quad (4.18)$$

where z_d is the zero-plane displacement, which is assumed zero in the following. The plume width at a downwind distance x from the emission source is obtained as $\sigma_y(x/U, T_A)$.

The Lagrangian spectral density $S_v^L(f)$ is of the velocity fluctuation following fluid parcels. Since large-scale eddies with relatively large velocity carry small-scale eddies, the Eulerian spectral density $S_v^E(f)$ has larger magnitude at high-frequency range than $S_v^L(f)$ does (Tennekes & Lumley, 1972). The relationship between $S_v^E(f)$ and $S_v^L(f)$ is fairly complex, but in practice, the difference is expressed by simple frequency shift (*e.g.* Degrazia & Anfossi, 1998):

$$f S_v^L(f) = \beta f S_v^E(\beta f), \quad (4.19)$$

where $\beta = 0.55U/\sigma_v(T_A)$ and $\sigma_v(T_A)$ is the fluctuation of the crosswind velocity component for a period T_A . Because the frequency shift by (4.19) applies to

relatively high frequencies, only the third term in the model spectrum (4.16) is converted by (4.19).

It is desirable if $\sigma_v(T_A)$ could be calculated as the Lagrangian fluctuation $\sigma_v^L(T_A)$ from $S^L(f)$. However, since the crude nature of the conversion (4.19) does not balance with the elaborate recursive calculation necessitated by such a procedure, we use the Eulerian fluctuation $\sigma_v^E(T_A)$ for $\sigma_v(T_A)$. Hence, we have

$$\sigma_v^2(T_A) = \int_0^\infty S_v^E(f) \left\{ 1 - \frac{\sin^2(\pi f \hat{T}_A)}{(\pi f \hat{T}_A)^2} \right\} df \quad (4.20)$$

Note that $\sigma_v^L = \sigma_v^E$ in homogeneous turbulence, but in general $\sigma_v^L > \sigma_v^E$ (Tennekes & Lumley, 1972).

The coefficients b_1 , c_1 , B and C in the model spectrum (4.16) are determined as follows. First, for guessed values of b_1 , c_1 and C , the value of B is determined by equating the observed σ_v at a low wind speed with that calculated from (4.16). If the observation time is $T_{A,0}$ and the observed velocity fluctuation is $\sigma_{v,0}$, we have

$$\sigma_{v,0}^2 = \int_0^\infty S_{v,0}^E(f) \left\{ 1 - \frac{\sin^2(\pi f \hat{T}_{A,0})}{(\pi f \hat{T}_{A,0})^2} \right\} df, \quad (4.21)$$

where the right-hand side is evaluated at the observation height. Equation (4.21) can be readily integrated numerically, and the value of B is determined. The optimal values of b_1 , c_1 and C are obtained by matching the resulting $S^E(f)$ to the observations of Richards *et al.* (2000) and Anfossi *et al.* (2005). Good agreement is obtained by

$$b_1 = 1 \times 10^2, \quad c_1 = 8 \times 10^3, \quad C = 1 \times 10^3.$$

Fig. 4.1(a) shows the normalized non-dimensional spectrum $f S_v^E(f)/u_*^2$ for $U = 3 \text{ m s}^{-1}$. Plotted together is the model spectrum of Richards *et al.* (2000) for neutral stability and relatively large U . Their observation condition $z = 10$ and $z_0 = 0.01$ is used. For this value of z_0 , we assume $\sigma_{v,0} = 0.3 \text{ m s}^{-1}$ at $U = 1 \text{ m s}^{-1}$ with $T_{A,0} = 3600 \text{ s}$ (see Table 4.1). The model of Richards *et al.* (2000) for the alongwind component S_u^E is given by (4.7) with

$$C' = 0.004, \quad D' = 0.74, \quad E' = 3.7, \quad \alpha = 0.55 + 0.1 \ln \frac{z}{z_0}.$$

The conversion to S_v^E is given by

$$\frac{S_v^E}{S_u^E} = \frac{1}{2} + \frac{1}{\frac{6}{5} + \frac{1}{4}f}. \quad (4.22)$$

The approximate range of validity of their model is $f_1 = (z_0/u_*)(U/z)f \gtrsim 10^{-4}$. In Fig. 4.1(a), the Richards *et al.*'s model is drawn in this valid range. The model spectrum (4.16) agrees well with the Kaimal spectrum at high frequencies and with Richards *et al.*'s model at low frequencies. Similarly good agreement is found for $U > 3 \text{ m s}^{-1}$.

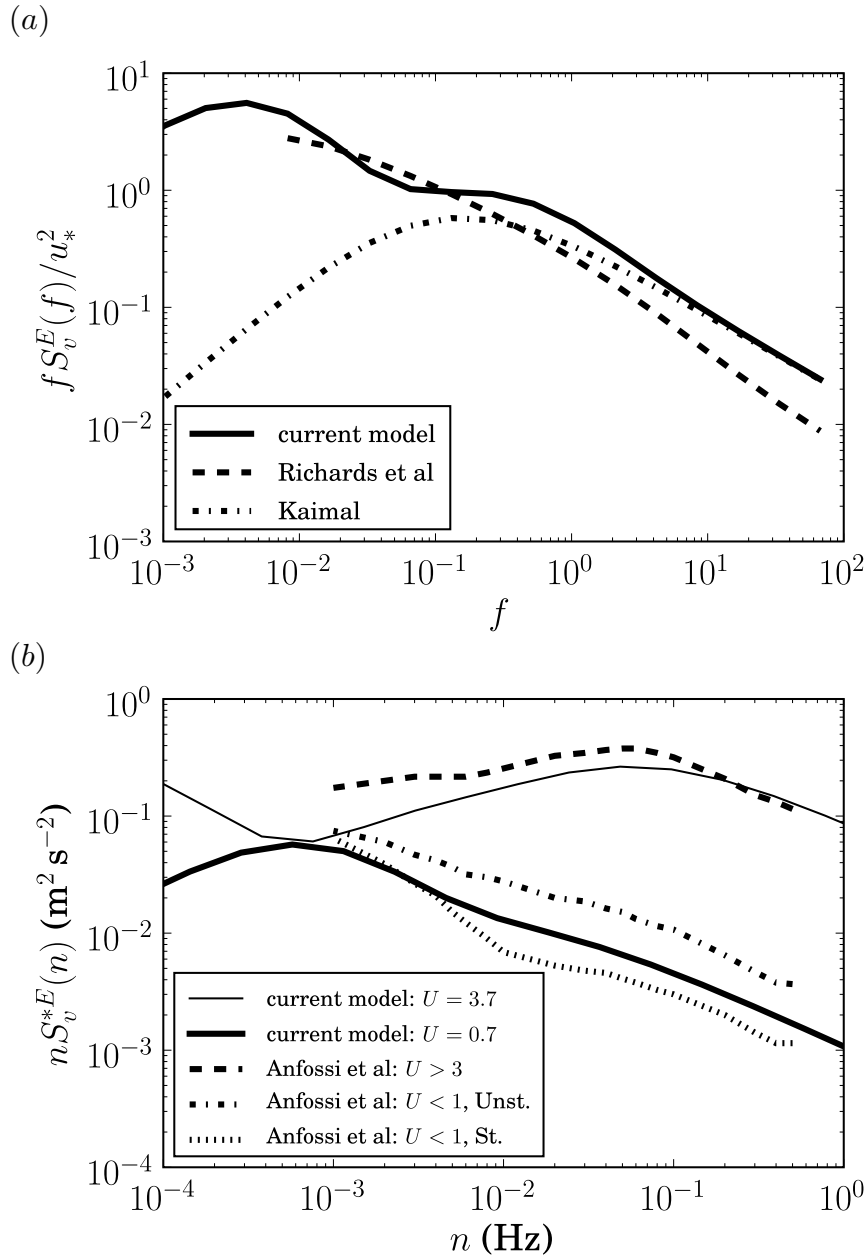


Figure 4.1: Comparison of the model spectrum (4.16) with field observations by Richards *et al.* (2000) (a) and Anfossi *et al.* (2005) (b). In sub-figure (b), Unst. stands for Unstable and St. for Stable.

Fig. 4.1(b) shows the dimensional spectrum $nS_v^{*E}(n)$ where the superscript * denote that the spectral density is defined on the dimensional frequency n . Dimensional expression is used here to compare directly with Fig. 5 of Anfossi *et al.* (2005). Their measurement had $z = 10$ m and $z_0 = 1.1$ m s⁻¹ (this latter value was obtained through personal communication). Considering the relatively ragged surrounding terrain and the nearby residential area, we set $\sigma_{v,0} = 0.5$ m s⁻¹ at $U = 1$ m s⁻¹ with $T_{A,0} = 3600$ s (see Table 4.1). The data of Anfossi *et al.* (2005) are classified into stable calm ($U < 1$ m s⁻¹, $z/L > 0.75$), unstable calm ($U < 1$ m s⁻¹, $z/L < -0.75$), and non-calm ($U > 3$ m s⁻¹). In Fig. 4.1(b), $U = 3.7$ m s⁻¹ is the actual average of Anfossi *et al.* (2005) for $U > 1$ m s⁻¹ (personal communication) and $U = 0.7$ m s⁻¹ is chosen as a representative value for $U < 1$ m s⁻¹. For calm wind, the model spectrum (4.16) falls around the middle of stable and unstable data. The model spectrum almost coincides with the stable curve when $U = 0.5$ m s⁻¹ and with the unstable curve when $U = 1.0$ m s⁻¹ (not plotted), which is consistent with lower and higher wind speed for stable and unstable conditions, respectively. For non-calm wind, the model is a little smaller than the observation. Overall, however, the model spectrum agrees well with Anfossi *et al.*'s observations.

Eddy diffusivity

Eddy diffusivity $K_y(x)$ is calculated as follows. Here, the downwind distance x from the source appears as the argument since the eddy diffusivity is to be used in the Eulerian diffusion equation. For an instantaneous emission or a slender plume (large x) from a continuous source, $K_y(x)$ can be related to σ_y by (Batchelor, 1949)

$$\begin{aligned} K_y(x, T_A) &= \frac{1}{2} \left. \frac{d\sigma_y^2}{dt} \right|_{t=x/U} \\ &= \frac{z}{U} \int_0^\infty S_v^L(f) \frac{\sin 2\pi f \hat{t}}{2\pi f} \left\{ 1 - \frac{\sin^2(\pi f \hat{T}_A)}{(\pi f \hat{T}_A)^2} \right\} df. \end{aligned} \quad (4.23)$$

However, for non-slender plume from a continuous source, no such a simple relationship exists. From the physical point of view, it is after all illogical to describe the inherently Lagrangian problem of turbulent diffusion by the Eulerian concept of eddy diffusivity (Taylor, 1959; Degrazia & Moraes 1992). Nonetheless, the great advantage of calculation speed gain by the Eulerian diffusion equation should be appreciated, and we seek a workaround. A simple approach is to apply (4.23) to non-slender plumes as well. Non-slender plumes occur near the source where the downwind distance is comparable to the plume width. By the homogeneous turbulence theory, the plume width near the source, or when the particle travel time is much less than the Lagrangian timescale, becomes $\sigma_y \sim \sigma_v t$. Introducing a parameter $\gamma = \sigma_v^2/U^2$, we get $\sigma_y = \sqrt{\gamma} U t$. Then, substituting this σ_y into (4.23), we find $K_y = \gamma U x$, the assumption employed by Sharan *et al.* (1996) for a weak-wind dispersion model which compared well

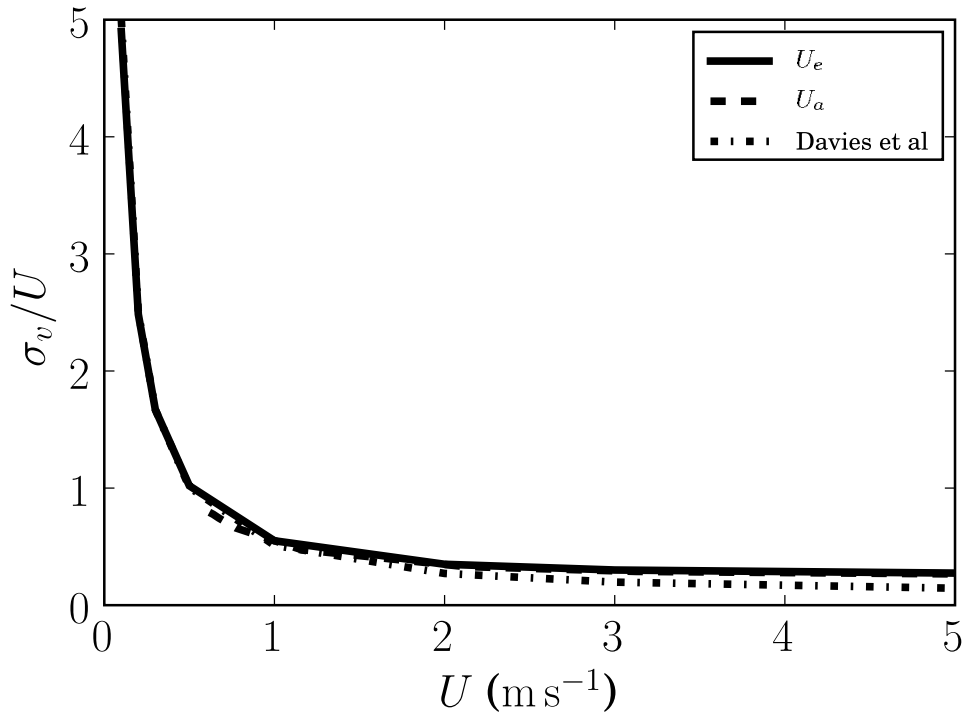


Figure 4.2: Dependence of σ_v on U_e and U_a . The mean velocity U in the model spectrum is regarded the vector mean U_e . The corresponding scalar mean U_a is calculated by the relationship obtained by Castans & Barquero (1994). The model parameters are $z_0 = 0.03$ m, $z = 10$ m, $T_A = 3600$ s and $\sigma_{v,0} = 0.3$ m s⁻¹ at $U = 1$ m s⁻¹ with $T_{A,0} = 3600$ s.

with their observation data. Therefore, equation (4.23) is applied to all stages of plume evolution.

4.1.4 Comparison with field observations

Crosswind velocity fluctuation σ_v

Fig. 4.2 shows σ_v/U for the observation condition of Davies & Thomson (1999): $z = 21$ m, $z_0 = 0.01$ m, $T_A = 3600$ s and $\sigma_{v,0} = 0.55$ m s⁻¹ ($U = 1$ m s⁻¹, $T_{A,0} = 3600$ s). Both U_e and U_a are used for U ; U in the model spectrum is regarded as U_e , and U_a is calculated from U_e by the relationship obtained by Castans & Barquero (1994).

Fig. 4.2 indicates that the difference by exchanging U_a and U_e is negligible, and that the model prediction is almost identical to the observed relationship (4.2) by Davies & Thomson (1999). Although the observation data of Davies & Thomson are from stable atmospheric conditions, similar behavior of σ_v/U was observed for both stable and unstable conditions (Table 4.1) and it is appropriate to assign the same behavior to urban neutral conditions.

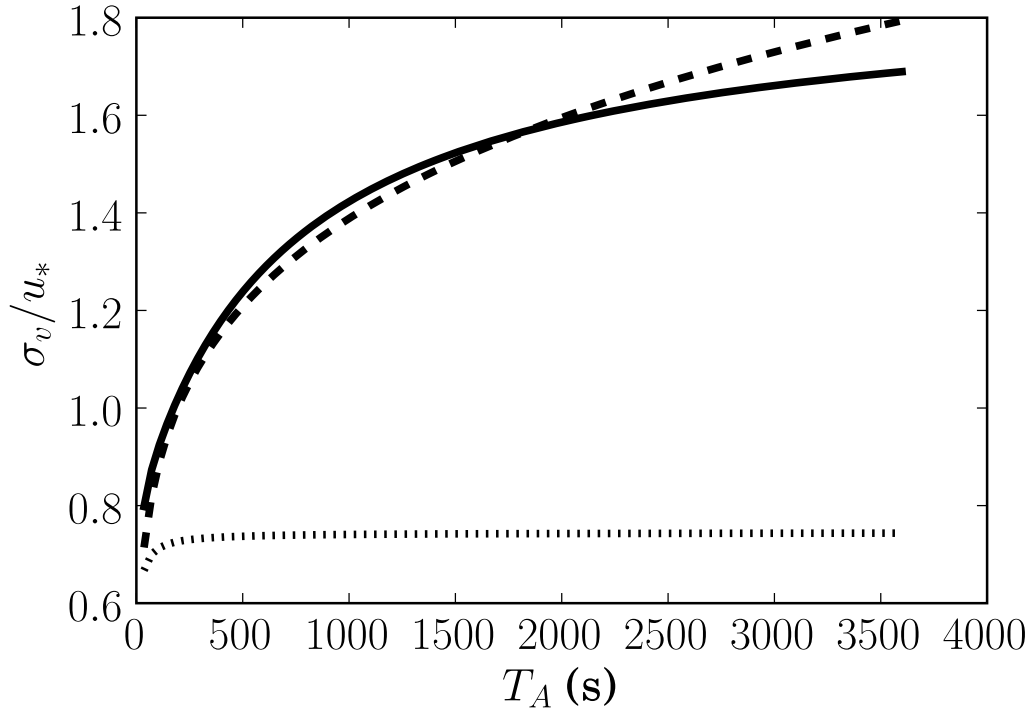


Figure 4.3: Dependence of σ_v on T_A . Dotted curve is for the high-frequency component (the third term in (4.16)) only. The model parameters are $z_0 = 0.03$ m, $z = 10$ m and $\sigma_{v,0} = 0.3$ m s^{-1} at $U = 1$ m s^{-1} with $T_{A,0} = 3600$ s.

Dependence of σ_v on T_A

Dependence of σ_v on T_A is often expressed by a power law $\sigma_v \propto T_A^q$. The exponent q depends on the weather condition, but a popularly used, though not universal, value is $q = 0.2$ (Panofsky, 1988). Fig. 4.3 compares the model-derived σ_v/u_* and the power law with $q = 0.2$ for $U = 3$ m s^{-1} . Plotted together is the model calculation using only the high-frequency part (the third term in (4.16)). The model parameters $z = 10$ m, $z_0 = 0.03$ m, $T_A = 3600$ s and $\sigma_{v,0} = 0.3$ m s^{-1} ($U = 1$ m s^{-1} , $T_{A,0} = 3600$ s) are taken or guessed from the widely used observation data of Smith & Abbott (1961). The model spectrum predicts $T_A^{0.2}$ behavior well. It is noted that, with only the high-frequency part, σ_v saturates in about 10 minutes.

Crosswind plume width σ_y

In the following, where appropriate, comparisons are made with conventional models instead of field observations because well-established conventional models may be regarded as representing many field observations.

Strong wind, $T_A = 180$ s The Pasquill–Gifford–Turner chart, or its analytical expression Briggs’ formula, is adopted in many prediction models (e.g. ISC3 by Environmental Protection Agency). For sufficiently high wind speed, $T_A =$

180 s, $z_0 = 0.03$ m, and neutral stability, the cross wind plume width σ_y is given by

$$\sigma_y(x) = 0.08x(1 + 0.0001x)^{-1/2}. \quad (4.24)$$

Fig. 4.4(a) compares the Briggs formula (4.24) with the prediction by the current model at $z = 1.5$ m and $U = 3 \text{ m s}^{-1}$ assuming $\sigma_{v,0} = 0.3 \text{ m s}^{-1}$ at $U = 1 \text{ m s}^{-1}$ with $T_{A,0} = 3600$ s. The model under-predicts σ_y considerably with the discrepancy growing downwind. This seemingly poor comparison is actually a reasonable one. Equation (4.17) calculates σ_y about the instantaneous plume axis determined in the observation period T_A . This plume axis does not generally coincide with the windward line through the emission source (the center line). In contrast, σ_y of the Briggs formula (4.24) is defined as the plume width about the center line. This notion, however, is valid only when the pollutant travel time is sufficiently smaller than T_A . For $U = 3 \text{ m s}^{-1}$, the 180 s-averaged plume axis is likely to be on the center line only in $x \ll 540$ m. Beyond this x range, the plume axis averaged for $T_A = 180$ s is generally off the center line. Hence, σ_y of the Briggs formula (4.24) should be interpreted as some though not full ensemble average of $T_A = 180$ s observations. Therefore, except near the source, σ_y by the current model should become smaller than that by the Briggs formula.

Strong wind, $T_A = 600$ s Ten-minute average σ_y was measured in Project Prairie Grass (PPG) (Barad, 1958; Hanna *et al.*, 1991). For neutral stability, the measurement conditions were $U > 6 \text{ m s}^{-1}$ at $z = 2$ m and $z_0 = 0.006$ m. The plume width was determined at $z = 1.5$ m. Assuming $\sigma_{v,0} = 0.3 \text{ m s}^{-1}$ at $U = 1 \text{ m s}^{-1}$, $z = 1.5$ m with $T_{A,0} = 3600$ s, the current model and the PPG results are compared in Fig. 4.4(b) for $U = 6 \text{ m s}^{-1}$. Agreement is fairly good.

Strong wind, $T_A = 3600$ s There are various models that predict long-time average plume, but ADMS is one of the most popular ones. In ADMS, σ_y is given by

$$\sigma_y^2 = \sigma_{yt}^2 + \sigma_{yw}^2, \quad (4.25)$$

where σ_{yt} is due to small-scale turbulence and σ_{yw} is due to wind direction variation. Each term is calculated by

$$\sigma_{yt} = \sigma_v t \frac{1}{\sqrt{1 + (15.6)^{1/3} u_* t / h}}, \quad (4.26)$$

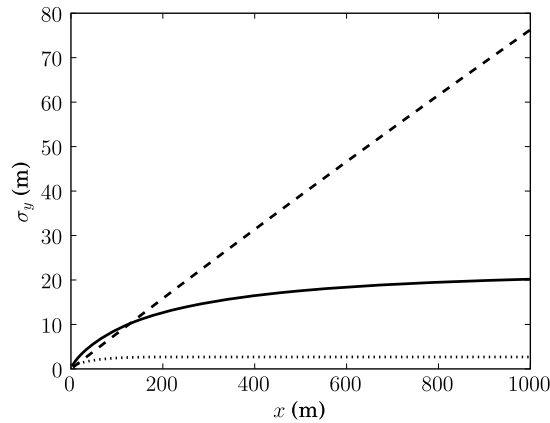
$$\sigma_{yw} = 0.065 x \sqrt{\frac{7(T_A/3600)}{U_{10}}}, \quad (4.27)$$

where h is the boundary-layer height, and σ_v is given by

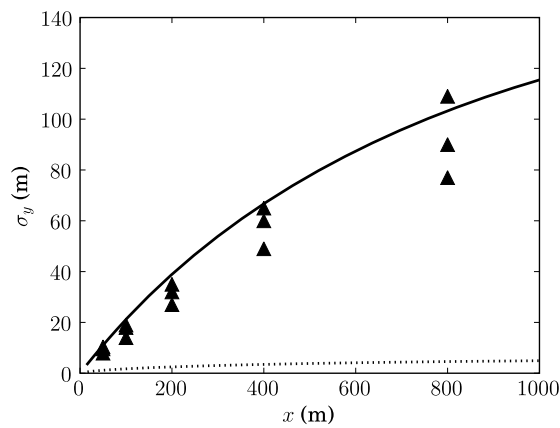
$$\sigma_v = 2.0u_* \left(1 - 0.8 \frac{z}{h}\right). \quad (4.28)$$

We set $h = 600$ m here. The wind speed range for ADMS is $U_{10} \geq 0.75 \text{ m s}^{-1}$.

(a)



(b)



(c)

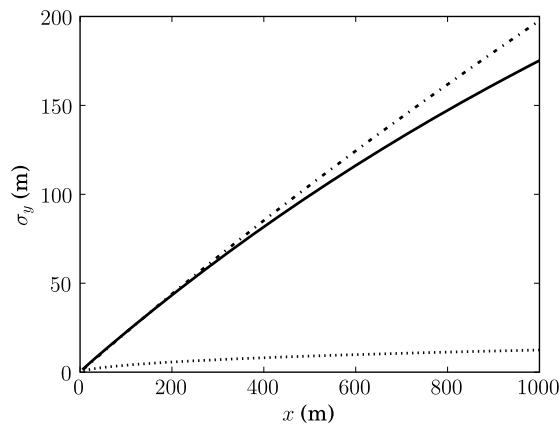


Figure 4.4: Comparison of horizontal plume width σ_y by the current model with that by conventional prediction models or field observation. In all plots, solid and dotted curves are the predictions by the current model (4.17) with the full spectrum (4.16) and with the third term (high-frequency spectrum) of (4.16) only, respectively. See text for the model parameters in each case. (a) $T_A = 180$ s. Dashed curve is the prediction by the Briggs formula. (b) $T_A = 600$ s. Triangle marks are the field observations of Project Prairie Grass. (c) $T_A = 3600$ s. Dashed-dotted curve is the prediction by ADMS.

Fig. 4.4(c) compares ADMS with the current model for a condition $z_0 = 0.03$ m, $z = 1.5$ m, $U = 3$ m s⁻¹, and $\sigma_{v,0} = 0.3$ m s⁻¹ at $U = 1$ m s⁻¹ with $T_{A,0} = 3600$ s. Agreement is good.

Weak wind, $T_A = 3600$ s Prediction in weak-wind condition is usually not guaranteed by conventional models. An exception is the Puff formula adopted in a Japanese regulatory model (Japan Environment Agency). The original Puff formula represents the diffusion of an instantaneously released ‘puff’ of pollutant (Csanady, 1973), and the plume width is given by $\sigma_y = \sqrt{\gamma Ut}$ as mentioned in §4.1.3. Theoretically, the Puff formula applies only to near-source plumes, but in the above Japanese model, it is extended to fairly long distance by specifying appropriate values of γ . For urban Japan with $T_A = 3600$ s, σ_y is given by

$$\tilde{\sigma}_y = \begin{cases} 0.47t & (U_{10} \leq 0.4 \text{ m s}^{-1}) \\ 0.27t & (U_{10} \leq 0.9 \text{ m s}^{-1}) \end{cases}, \quad (4.29)$$

where $t = x/U_{10}$ is the travel time. Note that the linear dependence on U is modified to a step-wise dependence.

Fig. 4.5 compares σ_y by the Japanese Puff model and by the current model assuming $z_0 = 0.8$ m and $\sigma_{v,0} = 0.5$ m s⁻¹ at $U = 1$ m s⁻¹ with $T_{A,0} = 3600$ s. Two representative wind speed values $U = 0.4$ (typical lower limit of propeller anemometers) and 0.7 m s⁻¹ are used. Considering the crude nature of the Puff model, overall agreement in Fig. 4.5 can be said satisfactory.

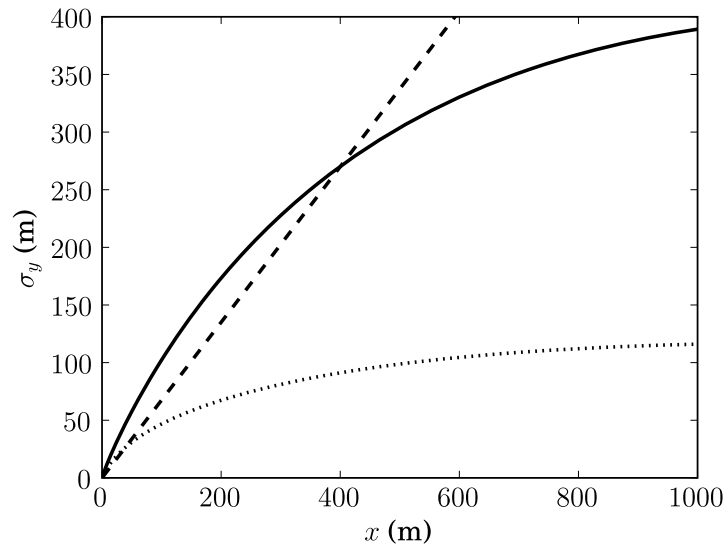
4.1.5 Summary and discussion

This chapter presented a derivation of the horizontal plume width from a continuous point source using the classical diffusion theory with a tentative velocity spectrum. The velocity spectrum agrees approximately with low-frequency field observations and reproduces the observed large wind-direction fluctuations at low wind speed. The calculated plume width agreed fairly well with the predictions by conventional air-pollution models or the results of field experiments for a wide range of observation duration and mean wind speed. The good agreement guarantees that the eddy diffusivity readily derived from the proposed spectrum can be used in prediction models based on the advection–diffusion equation.

The proposed spectrum (4.16) is an exploratory one. There may be numerous criticisms against it; the physical interpretation of the low-frequency terms is too speculative, the values of the parameters b , c and C have too much freedom, the calculated value of B can become negative for small $\sigma_{v,0}$, the two lumps in Fig. 4.1(a) is unrealistic, and so on. The important point, however, is that the plume width under practical conditions cannot be predicted correctly without incorporating low-frequency and low-wind-speed components into the spectrum. The proposed spectrum is at least equipped with these components. To improve the spectrum, more field observation data would be necessary.

It has been known that the low-frequency turbulence is affected strongly by the local characteristics such as terrain variations or land-water configurations.

(a)



(b)

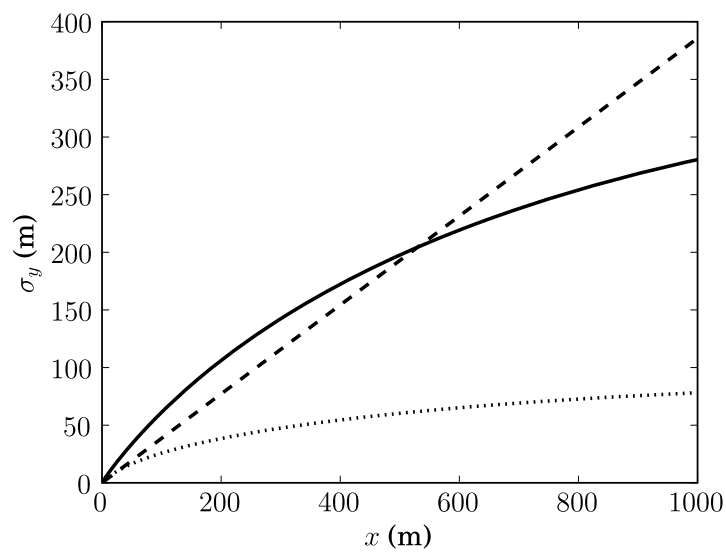


Figure 4.5: Comparison of horizontal plume width σ_y for low wind speed conditions by the current model with that by the Puff model with the Japanese parameters. Solid and dotted curves are the predictions by the current model with the full spectrum (4.16) and with the third term (high-frequency spectrum) of (4.16) only, respectively. Dashed curves are the predictions of the Puff model. (a) $U = 0.4 \text{ ms}^{-1}$, (b) $U = 0.7 \text{ ms}^{-1}$.

Hence, although labeled tentative, seeking a single form of a velocity spectrum may have seemed an irrational attempt. However, from the standpoint of pollution studies where estimation of long-term (for months or years) exposure is often of concern, robust and gross mean is preferred to sensitive and detailed individual samples. Conventional prediction models have been developed with this philosophy, and the structures of such models are deceptively simple despite the complexity of the real weather and terrain conditions. This chapter aims at application in pollution studies, and the proposed spectrum is best described as a spectral representation of the conventional prediction models rather than a deduction from field observations of atmospheric wind.

4.2 Emission along roads with signals

4.2.1 Introduction

In the prediction of atmospheric dispersion of vehicle exhaust pollutants, estimation of the amount of exhaust emission is important since it is proportional to the predicted concentration. If the mean vehicle velocity \bar{V} and the number N_j of the vehicle type j per unit time are given, the mean emission rate \bar{q} per unit length can be estimated by

$$\bar{q} = \sum_j N_j \epsilon_j(\bar{V}), \quad (4.30)$$

where $\epsilon_j(\bar{V})$ is the emission factor for the vehicle type j , which is obtained by driving test vehicles on chassis dynamometers with typical speed variation (mean travel speed \bar{V}) simulating the real traffic condition. This \bar{q} , however, is the average emission over sufficiently long distance in which the driving pattern for the chassis dynamometer tests is realized at least once. Hence, \bar{q} by equation (4.30) is applicable to dispersion prediction of spatial scales of at least a few kilometers. For dispersion prediction for smaller spatial expanses, local features such as traffic signals or toll gates, which cause significant deviation of emission rate from the mean \bar{q} , needs to be taken into account. Such spatial scales coincide with the scope of MCAD, which accounts for the effect of complex building configuration in urban areas. Therefore, the emission input data for MCAD needs to be modified if there are traffic signals or toll gates in the concerned region.

This chapter describes the principles and the detailed procedure of modifying the MCAD input data. The principles, a slight modification from those devised by Environmental Restoration and Conservation Agency of Japan (ERCA; Japan Weather Association (2005)), are explained in §4.2.2. Dependence of the modified emission profile on the input parameters is examined in §4.2.2. A representative emission profile is proposed in §4.2.3. Then, §4.2.4 gives the details of numerical implementation.

4.2.2 Principles

Traffic behavior near signals or toll gates is simulated by the optimal velocity model of the car-following family of traffic simulation methods. The emission enhancement due to acceleration or idling is calculated by the method of ERCA, which is based on on-vehicle emission measurement.

Optimal velocity model

In the optimal velocity model, vehicles are represented by discrete points along the road. The velocity V of a vehicle obeys

$$\frac{dV}{dt} = G \{V_{\text{opt}}(S) - V\}, \quad (4.31)$$

where t is time, G is gain, and $V_{\text{opt}}(S)$ is the optimal velocity when the spacing (head-to-head) to the preceding vehicle is S . Hence, a vehicle accelerates if the current velocity is smaller than the optimal velocity, and vice versa.

The optimal velocity $V_{\text{opt}}(S)$ is determined from the safe distance S when the vehicles are running at V_{opt} . If a vehicle suddenly stops the tire rotation from velocity V , then it takes a distance $V^2/2gf$ to come to a halt, where g is the gravitational acceleration and f is the friction coefficient. Since human reaction to hit the brake is not instantaneous, distance $V\tau$ for the reaction time τ is added. Further adding the head-to-head distance l when the vehicles are stopped, the critical distance becomes

$$S = l + V\tau + V^2/2gf. \quad (4.32)$$

Typical values for G , l , τ and f are

$$G = 1.0, \quad l = 8 \text{ (m)}, \quad \tau = 1 \text{ (s)}, \quad f = 0.7.$$

On trunk roads in urban area, it may be assumed that vehicles run below the legal speed limit V_m . Defining the corresponding spacing S_m by

$$S_m = l + V_m\tau + V_m^2/2gf, \quad (4.33)$$

the optimal velocity of vehicles for a given spacing S becomes

$$V_{\text{opt}}(S) = \begin{cases} gf\tau \left\{ -1 + \sqrt{1 + \frac{2}{gf\tau^2}(S-l)} \right\} & (S < S_m) \\ V_m & (S \geq S_m) \end{cases}, \quad (4.34)$$

where the upper branch is the meaningful solution of equation (4.32). Fig. 4.6 shows $V_{\text{opt}}(S)$ for $V_m = 60$ (km/h), $l = 8$ (m), $\tau = 1$ (s), and $f = 0.7$.

On an infinite one-dimensional road, writing the coordinate and the velocity of the k th vehicle at the time step n as x_k^n and V_k^n , respectively, the optimal velocity model (4.31) can be discretized in time as

$$\frac{V_k^{n+1}}{\Delta t} = G \{V_{\text{opt}}(S_k^n) - V_k^n\}, \quad (4.35)$$

where

$$S_k^n = x_{k-1}^n - x_k^n. \quad (4.36)$$

The vehicle coordinate is incremented by

$$x_k^{n+1} = x_k^n + V_k^n(\Delta t). \quad (4.37)$$

This explicit Euler scheme with error $O(\Delta)t$ is sufficient for the current purpose. Note that the vehicle index k increases toward the tail of the vehicle queue.

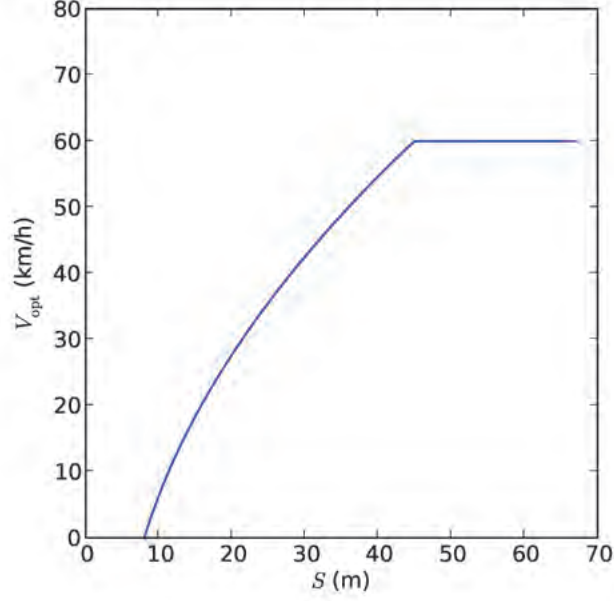


Figure 4.6: Example of optimal velocity.

In the actual numerical simulation, it is convenient to consider a circular route with radius R . Then, the above equations become

$$\frac{V_k^{n+1}}{\Delta t} = G \{V_{\text{opt}}(S) - V_k^n\}, \quad (4.38)$$

$$S_k^n = R \left(\left[\theta_{(k-1)\%K}^n - \theta_k^n \right] \right), \quad (4.39)$$

$$\theta_k^{n+1} = \theta_k^n + \frac{1}{R} V_k^n \Delta t, \quad (4.40)$$

where K is the number of vehicles in the route, and the cyclic angle difference $[\theta]$ is defined by

$$[\theta] = \begin{cases} \theta & (\theta \geq 0) \\ \theta + 2\pi & (\theta < 0) \end{cases}.$$

Note that θ_k^n increases monotonically and that the modulus operator $\%$ is defined as

$$\begin{aligned} 1\%K &= 1, \\ 0\%K &= 0, \\ -1\%K &= K - 1. \end{aligned}$$

A traffic signal is specified by the angle coordinate θ_s ($0 \leq \theta_s < 2\pi$), signal cycle T_c , the time ratio r_t of red state, and the start time T_s of the signal cycle. Assuming that the signal starts at the turn from red to green, the signal state

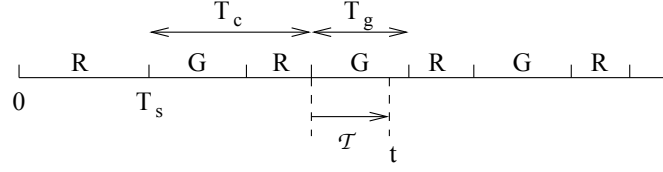


Figure 4.7: Signal sequence. G and R represent green and red signal states, respectively.

at time t is given by

$$\mathcal{T} - T_g \begin{cases} \leq 0 & \text{green} \\ > 0 & \text{red} \end{cases}, \quad (4.41)$$

where

$$\mathcal{T} = (t - T_s) - T_c \text{floor}((t - T_s)/T_c) \quad (4.42)$$

and $T_g = (1 - r_t)T_c$ is the duration of green. Fig. 4.7 shows the signal sequence. If the signal is red and the $(k - 1)\%K$ 'th and the k th vehicles sandwich the signal, the spacing is replaced by

$$S_k^n = R \left[\theta_s - \hat{\theta}_k^n \right], \quad (4.43)$$

where $\hat{\theta} = \theta - 2\pi \text{floor}(\theta/2\pi)$ is the normalized $[0, 2\pi)$ angle. Since the signal location θ_s is fixed, S_k and V_k decreases until the k th vehicle stops.

A toll gate can be represented by a signal with the red ratio $r_t = 1.0$. A toll gate becomes virtually green in a short period after payment is done. To simulate such a behavior, a signal timer is introduced. This timer is incremented if there is a stopped vehicle in front of the gate, and is reset if the timer is over the signal cycle T_c . Here, a vehicle is regarded stopping if the velocity V_k is below a small non-zero value V_{stop} since the reported toll-gate cycle T_c (~ 10 s) usually include the time of gradual approach to the gate. When the timer is reset, the spacing between the preceding vehicle is switched from (4.43) to (4.39), and the vehicle can pass the gate at non-zero optimal velocity. In the numerical code, the signal timer is kept zero until the vehicle have completely passed the gate.

At $t = 0$, the vehicles are distributed randomly on the circular route and started with the optimal velocity for the initial spacing to the preceding vehicles. Fig. 4.8 shows the trajectories of the vehicles for traffic-signal and toll-gate cases. For the traffic-signal case, the vehicle behavior reaches equilibrium by the third cycle around the route. The simulation parameters are as follows.

(a) traffic signal

$$\begin{aligned} \Delta t = 0.1 \text{ s}, \quad 2\pi R = 500 \text{ m}, \quad \theta_s = (3/5)2\pi, \quad T_c = 160 \text{ s}, \quad T_s = 0 \text{ s}, \quad r_t = 0.5, \\ K = 30, \quad f = 0.7, \quad G = 1.0, \quad \tau = 1 \text{ s}, \\ V_m = 60 \text{ km/h}, \quad l = 8 \text{ m}, \quad V_{\text{stop}} = 2 \text{ km/h} \end{aligned}$$

(b) toll gate

$$\begin{aligned} \Delta t = 0.1 \text{ s}, \quad 2\pi R = 1000 \text{ m}, \quad \theta_s = (3/5)2\pi, \quad T_c = 10 \text{ s}, \quad T_s = 0 \text{ s}, \quad r_t = 1.0, \\ K = 30, \quad f = 0.7, \quad G = 1.0, \quad \tau = 1 \text{ s}, \\ V_m = 80 \text{ km/h}, \quad l = 8 \text{ m}, \quad V_{\text{stop}} = 2 \text{ km/h} \end{aligned}$$

Mean traffic properties As described later in §4.2.2, traffic properties as averages over the vehicles and over the cycles around the circular route are necessary to estimate the emission profile along the road. This subsection explains the methods of calculating the following traffic properties from the results θ_k^n and V_k^n of the optimal velocity model simulation.

$$\begin{aligned} \text{Average velocity: } & \bar{V} \\ \text{Average lap time: } & \bar{T}_c \\ \text{Average traffic flow rate: } & \bar{F} \\ \text{Average maximum queue length: } & \bar{L}_{q,\max}^i \\ \text{Average stop rate: } & \bar{r}_s^i \\ \text{Average stop-signal velocity: } & \bar{V}_s^i \\ \text{Average pass-signal velocity: } & \bar{V}_p^i \end{aligned}$$

The superscript i denotes the signal index, which increases opposite to the traffic flow direction.

- Average velocity \bar{V}
The average velocity is defined as the mean velocity after vehicles have made the first round, *i.e.*

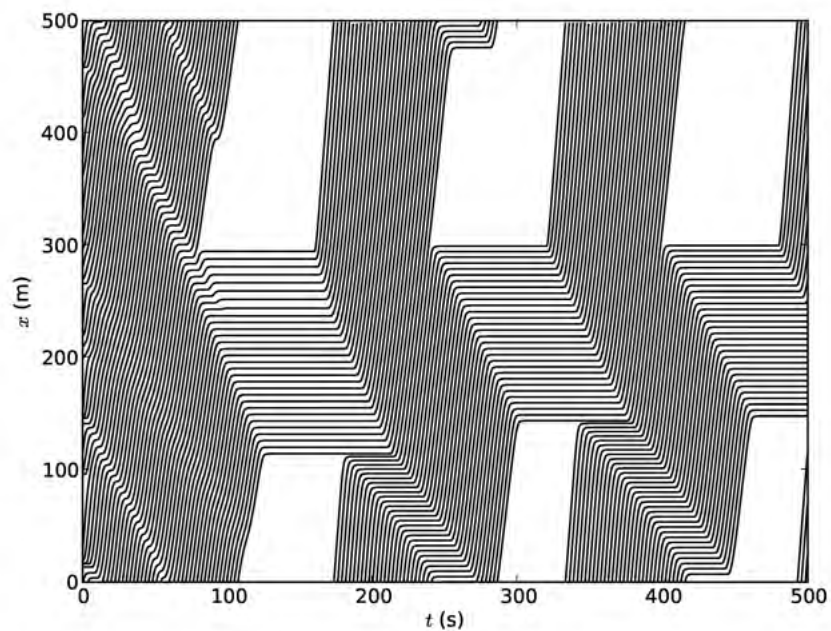
$$\bar{V} = \frac{1}{K} \sum_{k=0}^{K-1} \frac{1}{N_T - n_k^0} \sum_{n=n_k^0}^{N_T-1} V_k^n, \quad (4.44)$$

where $n = n_k^0$ is the time step index at the time when the k th vehicle has just made the first round, and N_T is the total number of time steps.

- Average lap time \bar{T}_{lap}
The lap time is the time required for a vehicle to make one cycle around the circular route. The average is calculated for the cycles excluding the first one, *i.e.*

$$\bar{T}_{\text{lap}} = \frac{1}{K} \sum_{k=0}^{K-1} \frac{(N_T - 1 - n_k^0)\Delta t}{\frac{\theta_k^{N_T-1} - \theta_k^{n_k^0}}{2\pi}}. \quad (4.45)$$

(a)



(b)

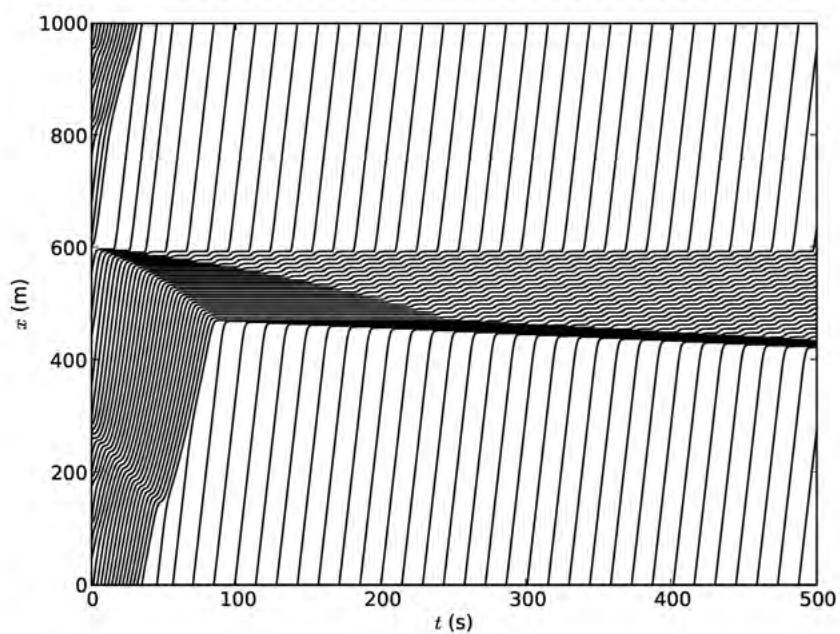


Figure 4.8: Vehicle trajectories for (a) traffic signal and (b) toll gate.

- Average traffic flow rate \bar{F}

Average traffic flow rate is the average number of vehicles passing at a point per unit time. It can be derived from \bar{T}_{lap} as

$$\bar{F} = \frac{K}{\bar{T}_{\text{lap}}}. \quad (4.46)$$

- Average maximum queue length $\bar{L}_{q,\text{max}}^i$

The queue length is the distance from the signal i to the farthest stopping vehicle in front of the signal. At each time step n , vehicles stopping in front of the signal i are identified as those satisfying

$$V_k^n < V_{\text{stop}},$$

$$R \left[\theta_{(k-1)\%K}^n - \theta_k^n \right] < 2l,$$

and

$$\begin{aligned} \theta_{S,(i-1)\%N_s} < \hat{\theta}_k^n < \theta_{S,i} & \quad (\theta_{S,(i-1)\%N_s} < \theta_{S,i}), \\ \theta_{S,(i-1)\%N_s} < \hat{\theta}_k^n \quad \text{or} \quad \hat{\theta}_k^n < \theta_{S,i} & \quad (\text{otherwise}), \end{aligned}$$

where $\theta_{S,i}$ is the angle location of the signal i and N_s is the number of signals. Fig. 4.9 shows a vehicle in front of a signal. The second condition is required in order to exclude a vehicle just leaving the signal $i + 1$ at a velocity less than V_{stop} . The third condition means that the vehicle is in front of the signal i . The case $\theta_{S,(i-1)\%N_s} < \theta_{S,i}$ occurs when the two signals do not straddle the angle origin, and the case ‘otherwise’ when they do. If there is just one signal ($N_s = 1$), the second and the third conditions are not examined because a vehicle is always in front of the signal. At each time step n , the queue length $L_q^{n,i}$ is calculated by

$$L_q^{n,i} = \max_{k \in \mathcal{K}_i} \left\{ R \left[\theta_{S,i} - \hat{\theta}_k^n \right] \right\}, \quad (4.47)$$

where \mathcal{K}_i is the set of vehicles stopping in front of the signal i . The average maximum queue length $\bar{L}_{q,\text{max}}^i$ is calculated as the maximum of $L_q^{n,i}$ after the average lap time T_{lap} has passed, *i.e.*

$$\bar{L}_{q,\text{max}}^i = \max_{n\Delta t > T_{\text{lap}}} \{ L_q^{n,i} \}. \quad (4.48)$$

- Average stop rate \bar{r}_s^i

The average stop rate \bar{r}_s^i is the probability that a vehicle stops at the signal i in one cycle around the circular route. In other words, if there are K vehicles, $K\bar{r}_s^i$ vehicles are likely to be stopped by the signal i in one cycle. To calculate \bar{r}_s^i , a stop-event flag $H_{i,k,c}$ is defined for signal i , vehicle k , and cycle c . The default value of $H_{i,k,c}$ is zero. $H_{i,k,c}$ is flagged,

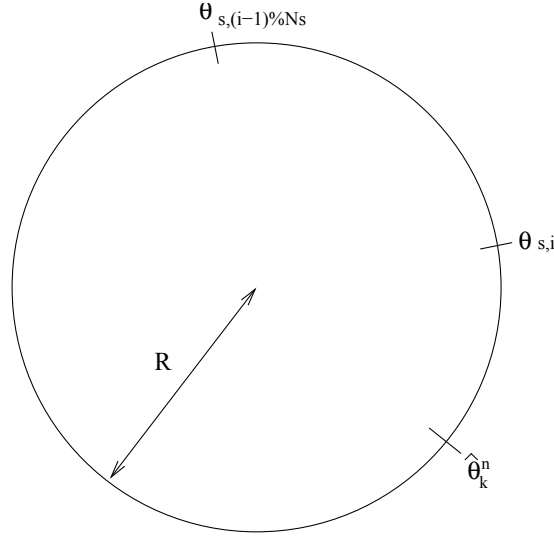


Figure 4.9: Configuration when vehicle k is in front of signal i .

or set unity, if the vehicle k decelerates to a stop in front of the signal i during the cycle c . Deceleration to a stop is detected by the occurrence of

$$V_k^{n-1} > V_{\text{stop}} \quad \text{and} \quad V_k^n < V_{\text{stop}}. \quad (4.49)$$

The mean stop rate \bar{r}_s^i is calculated by

$$\bar{r}_s^i = \frac{1}{K} \sum_{k=0}^{K-1} \frac{1}{C_k} \sum_{c=0}^{C_k-1} H_{i,k,c}, \quad (4.50)$$

where C_k is the number of completed cycles. Typical value of C_k is 2.

- Average stop-signal and pass-signal velocities \bar{V}_s^i and \bar{V}_p^i
 Average stop-signal and pass-signal velocities are the mean velocities in the near-signal region for vehicles that stop and pass the signal, respectively, in a cycle around the route. A near-signal region is defined between the end of the maximum queue and the front edge of the forward buffer L_f ahead of the signal (Fig. 4.10). The forward buffer is presumed to be the interval where vehicles accelerate toward the cruising velocity. For a cycle of a vehicle, if a stop event occurs in the cycle, the velocity V_k^n when the vehicle is inside the near-signal region is averaged to get the stop-signal velocity V_s . Similarly, if no stop event occurs in the cycle, the average of V_k^n inside the near-signal region becomes the pass-signal velocity V_p . The values for each cycle of each vehicle are averaged for all the cycles of all the vehicles to obtain \bar{V}_s^i and \bar{V}_p^i .

Fig. 4.11 shows examples of \bar{F} , \bar{V} , \bar{r}_s and $\bar{L}_{q,\text{max}}$ for $2 \leq K \leq 30$. They are averages over five simulation runs. Other parameter values are the same as for Fig. 4.8(a). The traffic flow rate \bar{F} saturates beyond $K \sim 15$ as \bar{V}

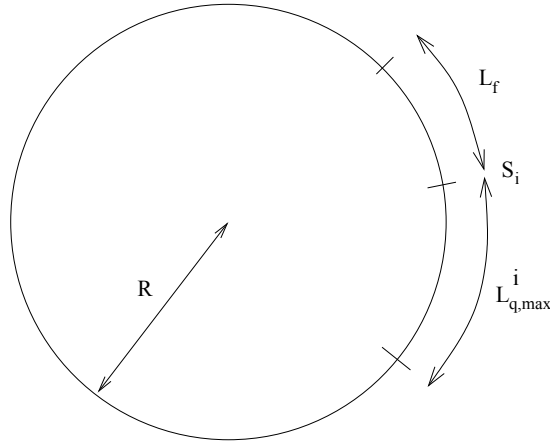


Figure 4.10: Near-signal region.

decreases rapidly. Similarly to \bar{V} , the stop rate \bar{r}_s and the maximum queue length $\bar{L}_{q,\max}$ changes rapidly as \bar{F} saturates. Typical daytime traffic flow rate per lane on urban trunk roads is $0.2 \sim 0.3$, which coincides with the saturation value. Hence, the figures indicate that it is quite difficult to estimate \bar{V} , \bar{r}_s or $\bar{L}_{q,\max}$ from \bar{F} although \bar{F} is the most readily available quantity from traffic census.

Emission rate profile

Overview Emission rate profile $q(x)$ around a signal is estimated using the traffic properties explained in the previous subsection. For simplicity, we consider the case where the signal is sufficiently separated from other signals, that is, the signal region (see Fig. 4.10) does not overlap with those of other signals. In the following, the index i for signals is omitted and the average maximum queue length $\bar{L}_{q,\max}^i$ is written as L_q

Near a signal, the emission rate $q(x)$ is modified from the mean \bar{q} given by equation (4.30) mainly by the following two driving modes:

- idling while the vehicles stop in front of the signal,
- acceleration after the signal turns from red to green.

Idling emission can be a significant contribution since it is from stationary vehicles. Enhanced emission by acceleration starts from the stop location and ends when the vehicle reaches the cruising velocity. A typical emission rate $q(x)$ around a signal at $x = 0$ is shown in Fig. 4.12.

Procedure In the signal-region, the emission consists of the contributions by signal-passing and signal-stopping vehicles, *i.e.*

$$q(x) = (1 - \bar{r}_s)\bar{q}(\bar{V}_p) + \bar{r}_s\bar{q}(\bar{V}_s), \quad (4.51)$$

where $\bar{q}(\bar{V}_p)$ and $\bar{q}(\bar{V}_s)$ are calculated by equation (4.30). Note that, since \bar{V} in (4.30) is for sufficiently long travel distance which includes speed variations,

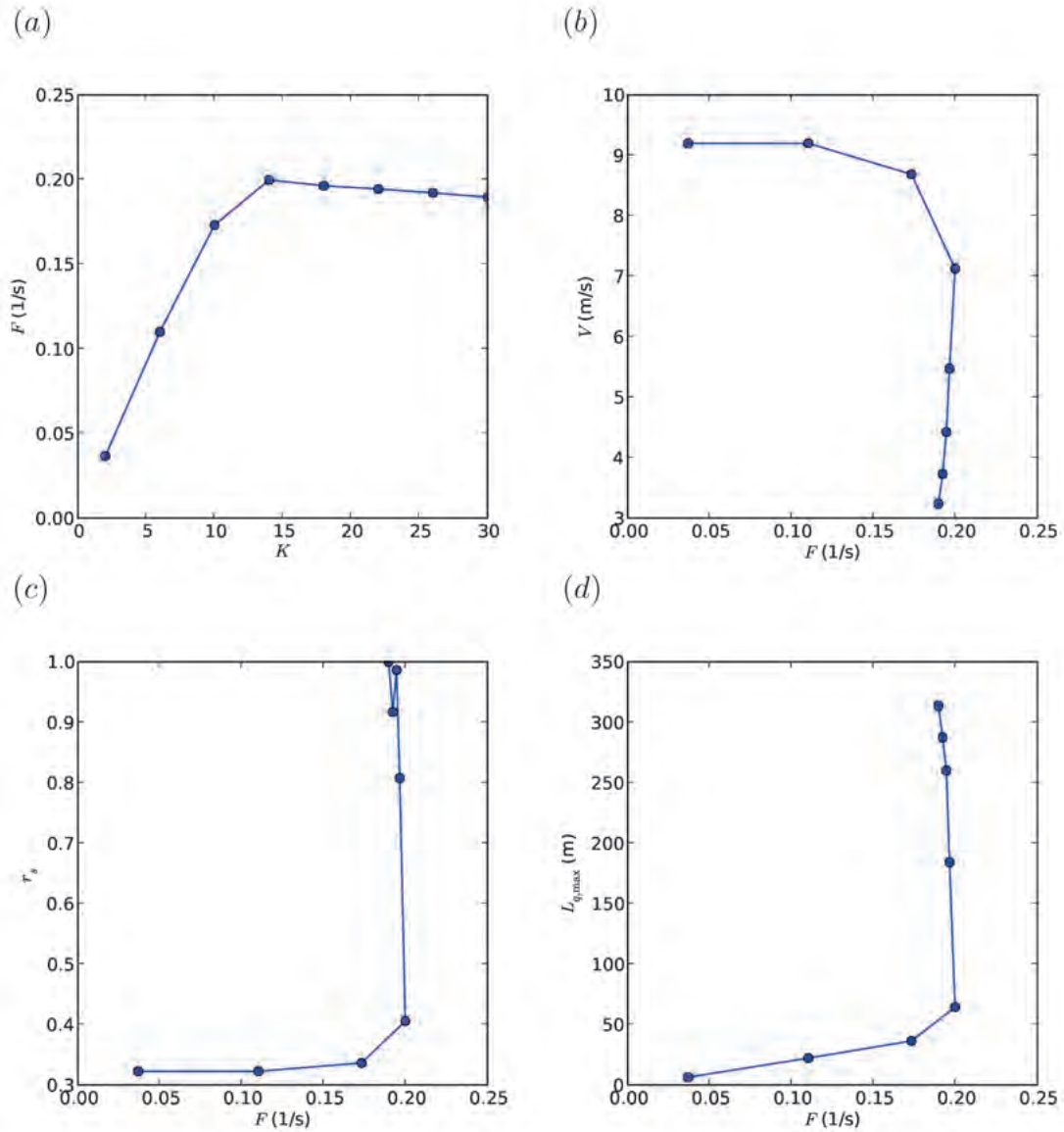


Figure 4.11: Mean traffic properties from optimal-velocity traffic simulations with $2 \leq K \leq 30$. Overbars on the mean quantities are omitted on the axis labels.

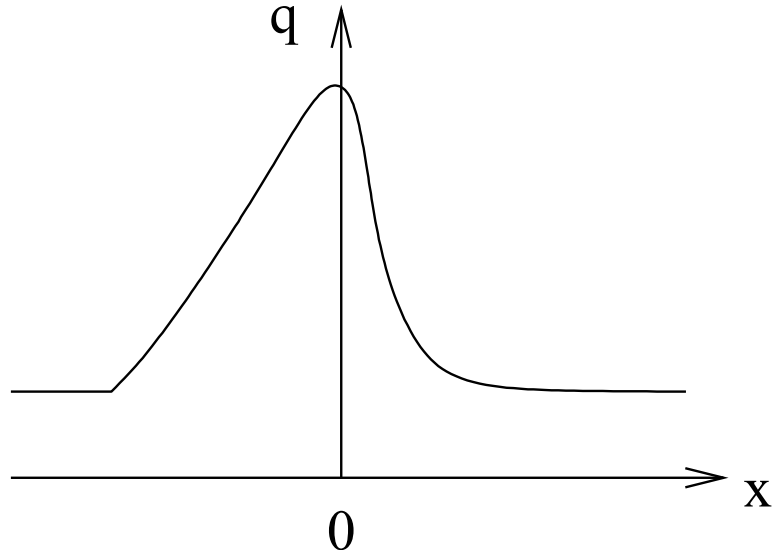


Figure 4.12: Typical signal emission profile

Table 4.2: Idling emission ratio taken from ERCA report in December 2005.

Speed range (km/h)	Representative speed (km/h)	Idling emission ratio (%)	
		Diesel	Gasoline
3 – 5	4	64	11
5 – 10	8	47	8
10 – 15	13	35	6
15 – 25	20	24	5
25 – 40	33	11	3
40 –	–	0	0

it may not be appropriate to apply (4.30) for the relatively short range around signals. Without better alternative, however, we compromise with the above formula. The term $\bar{q}(\bar{V}_s)$ by the signal-stopping vehicles is further divided into idling and non-idling components:

$$\bar{q}(\bar{V}_s) = b(\bar{V}_s)\bar{q}(\bar{V}_s) + (1 - b(\bar{V}_s))\bar{q}(\bar{V}_s), \quad (4.52)$$

where $b(\bar{V}_s)$ is the ratio of idling emission. The values of $b(\bar{V}_s)$ for gasoline and diesel vehicles are shown in table 4.2.

The idling component $b(\bar{V}_s)\bar{q}(\bar{V}_s)$ is distributed in front of the signal ($-L_q \leq x \leq 0$) in proportion to the probability to stop at x and the duration of stop (idling). It is assumed that the stop probability is proportional to $x + L_q$ (footnote ²) and the duration of stop is also proportional to $x + L_q$. Thus,

²For an equilibrium state like Fig. 4.8 of the optimal velocity simulation, L_q is the same for after the second or the third cycle. Hence the probability that there is a stopped vehicle in

writing the distribution factor as $\beta(x)$, we have

$$\beta(x) \propto (x + L_q)^2. \quad (4.53)$$

Normalizing such that

$$\int_{-L_q}^0 \beta(x) dx = 1, \quad (4.54)$$

we find

$$\beta(x) = \frac{3}{L_q^3}(x + L_q)^2, \quad (-L_q \leq x \leq 0). \quad (4.55)$$

The idling component is then altered as

$$b(\bar{V}_s)\bar{q}(\bar{V}_s)\beta(x). \quad (4.56)$$

The non-idling component, or the emission by moving vehicles, is distributed in the signal region using the on-vehicle measurements of real vehicles. The on-vehicle measurement is reported in the range 200 m in front and behind of the stop location. The probability density $\hat{R}(x)$ of the emission can be approximated by

$$\hat{R}(x) = \begin{cases} R_0 & (-200 \leq x \leq 0) \\ R_1 - (R_1 - R_0) \left\{ 1 - \left(1 - \frac{x}{200} \right)^p \right\}^{1/q} & (0 \leq x \leq 200) \end{cases}, \quad (4.57)$$

where $R_0 = 0.002$, $R_1 = 0.010622$, $p = 2$ and $q = 3$ (footnote ³). Fig. 4.13 shows the profile. Note that ERCA used a different function

$$10\hat{R}(x) = \begin{cases} 0.0189 & (-200 \leq x \leq 0) \\ -0.0183 \ln(x) + 0.1159 & (0 \leq x \leq 200) \end{cases}. \quad (4.58)$$

We opt for the formula (4.57) because it is free from singularity at $x = 0$ and is hence suitable for numerical calculation. Also, since the curved part is expressed by a quarter super-ellipse whose area can be calculated by the beta function (see Fig. 4.13), parameter fitting to the measured data is numerically inexpensive. However, as long as sufficiently coarse discretization is used in the numerical integration, the ERCA formula (4.58) also works fine. Since $\hat{R}(x)$ is a probability density function in $-200 \leq x \leq 200$, it satisfies

$$\int_{-200}^{200} \hat{R}(x) dx = R_0(400) + (R_1 - R_0)200\pi(p, q) = 1, \quad (4.59)$$

where

$$\pi(p, q) = 1 - \frac{1}{p+q} B\left(\frac{1}{p}, \frac{1}{q}\right). \quad (4.60)$$

$-L_q \leq x \leq 0$ is uniform. In reality, the queue length L_q varies with cycle, and the probability should be maximum at $x = 0$ and decrease toward negative x . The probability does not reach zero at $x = -L_q$. The functional form might be obtainable by some effort, but we find it not worth the effort. Hence, we use the crude form of linear decay toward $x = -L_q$.

³The parameters are determined by optimal fit to the measurement data with R_1 as the fitting parameter and the others fixed.

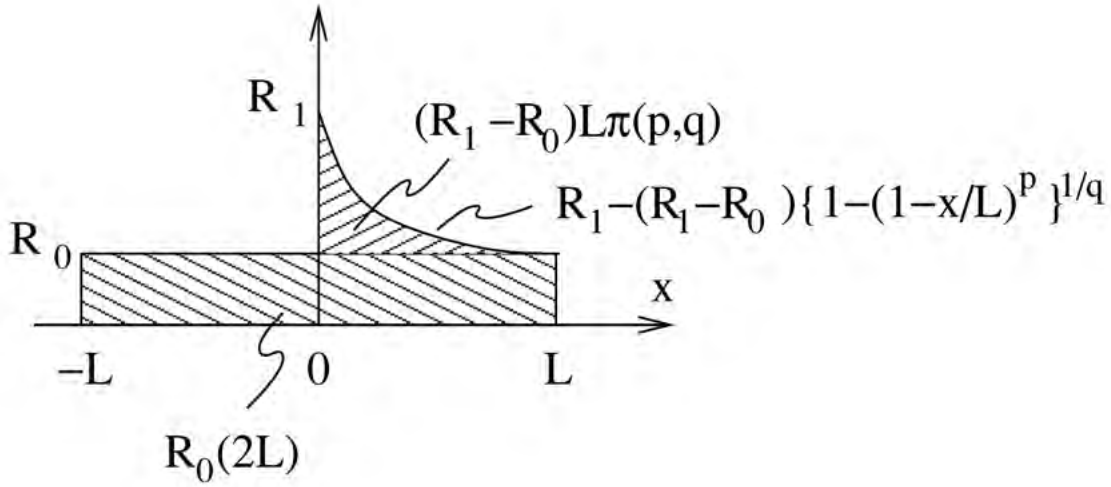


Figure 4.13: Non-idling emission component of a vehicle stopping at $x = 0$ with $L = 200$ m. The area function is defined by $\pi(p, q) = 1 - \frac{1}{p+q}B(\frac{1}{p}, \frac{1}{q})$.

Normally, we set $L_f = 200$ m, but L_q determined by traffic simulation differs from 200 m. For $L_q \neq 200$ m, $\hat{R}(x)$ is shortened or extended according as $L_q < 200$ and $L_q > 200$, respectively. Then, the generalized emission profile becomes

$$R(x) = \begin{cases} AR_0 & (-L_q \leq x \leq 0) \\ AR_1 - (R_1 - R_0) \left\{ 1 - \left(1 - \frac{x}{L_f} \right)^p \right\}^{1/q} & (0 \leq x \leq L_f) \\ AR_0 & (L_f \leq x) \end{cases}, \quad (4.61)$$

where the modification factor A is defined by

$$A = \frac{1}{1 + R_0(-L_f + L_q)} \quad (4.62)$$

so that

$$1 = \int_{-L_q}^{L_f} R(x) dx = \int_{-L_q}^{-200} + \int_{-200}^{200} AR(x) dx. \quad (4.63)$$

Further generalizing for the stop location $x = x_0$, we obtain

$$R(x, x_0) = \begin{cases} AR_0 & (-L_q \leq x \leq x_0) \\ AR_1 - (R_1 - R_0) \left\{ 1 - \left(1 - \frac{x-x_0}{L_f} \right)^p \right\}^{1/q} & (x_0 \leq x \leq x_0 + L_f) \\ AR_0 & (x_0 + L_f \leq x) \end{cases}. \quad (4.64)$$

Fig. 4.14 shows the generalized profile.

In order to get the emission profile by all the vehicles stopping in the queue, we need to sum (4.64) weighted by the probability that a vehicle stops at $x = x_0$. This probability $\alpha(x_0)$ is assumed to be

$$\alpha(x_0) = \frac{2}{L_q^2}(x + L_q) \quad (-L_q \leq x \leq 0). \quad (4.65)$$

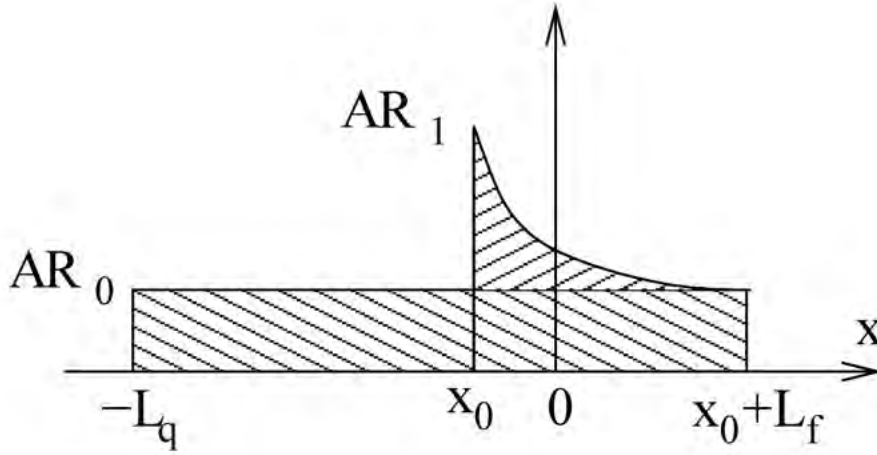


Figure 4.14: Generalized non-idling emission component of a vehicle stopping at $x = x_0$.

Then, weighting this probability, the emission profile of the non-idling component of the signal-stopping vehicles becomes

$$\mathcal{R}(x) = \int_{-L_q}^0 R(x, x_0) \alpha(x_0) dx_0. \quad (4.66)$$

The details of numerical integration are given in Appendix 4.2.5. Note that $\mathcal{R}(x)$ satisfies the normalization condition

$$1 = \int_{-L_q}^{L_f} \mathcal{R}(x) dx. \quad (4.67)$$

In summary, the near-signal emission profile becomes

$$q(x) = (1 - \bar{r}_s) \bar{q}(\bar{V}_p) + \bar{r}_s \{ b(\bar{V}_s) \bar{q}(\bar{V}_s) \beta(x) + (1 - b(\bar{V}_s)) \bar{q}(\bar{V}_s) \mathcal{R}(x) \}. \quad (4.68)$$

This formula derived bottom-up from the idling ratio, on-vehicle measurement and so on does not necessarily connect smoothly to the emission rate outside the signal region, nor is it consistent with the overall emission rate $\bar{q}(\bar{V})$. For the moment, we assume that the emission rate outside the signal region is equal to $\bar{q}(\bar{V}_p)$ and consider the continuity and overall conservation later in §4.2.3.

Parameter dependence of emission profile

The near-signal emission rate $q(x)$ is examined for various values of the signal and the traffic parameters. The emission species is NO_x whose emission factor is taken from an estimate in the Kanto area in 2005fy (table 4.3). The considered vehicle types are sedan (passenger car) and normal truck. The common parameters are

$$\begin{aligned} \Delta t &= 0.1 \text{ s}, & \theta_s &= (3/5)2\pi, & T_s &= 0 \text{ s} \\ f &= 0.7, & G &= 1.0, & \tau &= 1 \text{ s}, \\ l &= 8 \text{ m}, & V_{\text{stop}} &= 2 \text{ km/h}. \end{aligned}$$

Table 4.3: Emission factor ϵ of NO_x estimated for Kanto area in 2005fy (Naser *et al.* 2009).

$$\epsilon = c_0 + c_1V + c_2V^2 + c_3/V$$

	c_0	c_1	c_2	c_3
sedan	6.774e-2	6.7306e-4	2.3909e-5	1.5097
normal truck	2.6318	-2.8428e-2	2.4507e-4	1.8360e1

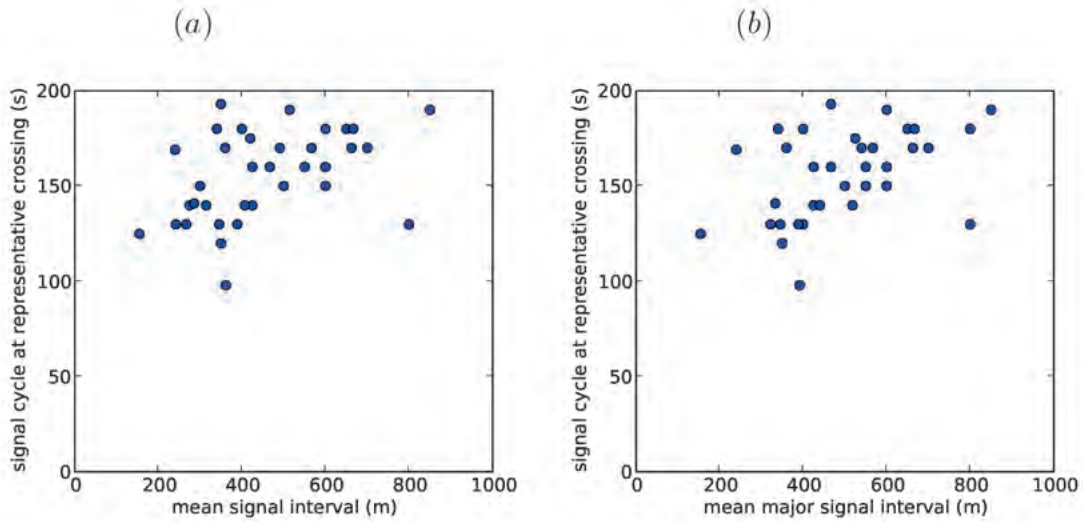


Figure 4.15: Cycle times of the signals in the routes relevant to the SORA project. The data are extracted from H17 traffic census. (a) all signals, (b) major signals only.

Signal cycle

From the H17 traffic census (Japan Ministry of Land, Infrastructure, Transport, and Tourism. H17 = fiscal year 2005), the cycle times of the signals in the routes relevant to the SORA project are shown in Fig. 4.15. In the SORA project, ten urban roads with estimated high diesel exhaust emission were selected for focus studies on pollutant exposure to residents. The simulation is run for the signal cycle T_c of 120, 140, 160, 180, and 200. Other parameters are

$$K = 18, \quad 2\pi R = 500 \text{ m}, \quad V_m = 60 \text{ km/h},$$

$$r_t = 0.5, \quad \text{sedan} : \text{normal truck} = 1 : 1.$$

Fig. 4.16 shows the result. The emission rate profile is relatively insensitive to the signal cycle.

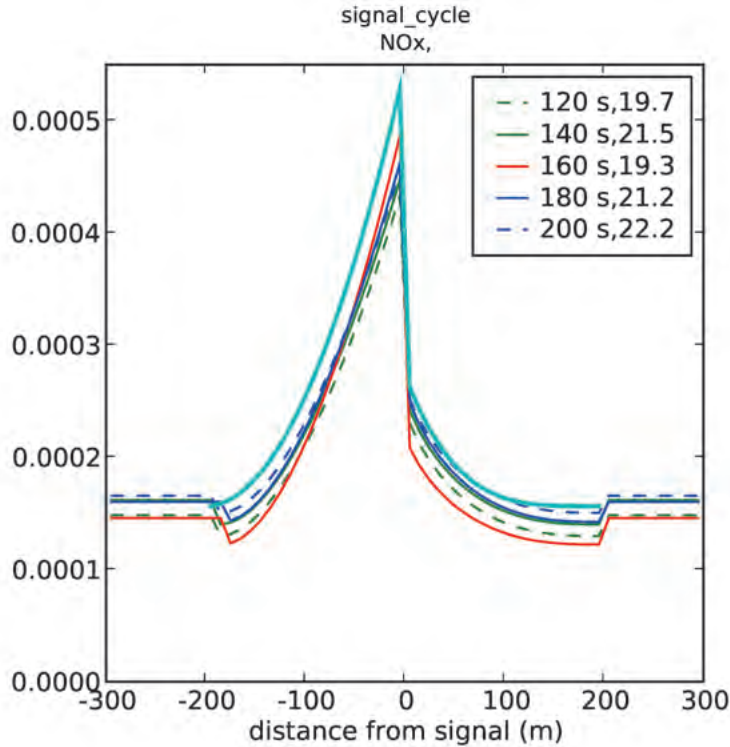


Figure 4.16: Dependence of $q(x)$ on the signal cycle T_c . The legend indicates T_c (s) and \bar{V} (km/h).

Red ratio

From the H17 traffic census, the red ratios of the signals in the routes relevant to the SORA project are shown in Fig. 4.17. The simulation is run for the red ratio r_t in 0.3, 0.4, 0.5, 0.6, 0.7. Other parameters are

$$K = 18, \quad 2\pi R = 500 \text{ m}, \quad V_m = 60 \text{ km/h}, \\ T_c = 160, \quad \text{sedan} : \text{normal truck} = 1 : 1.$$

Fig. 4.18 shows the result. The overall level of $q(x)$ decreases as r_t increases. This might contradict to the intuition that increased r_t should lead to slower traffic, then to larger emission factor and finally to larger $q(x)$. However, decrease of the traffic flow rate \bar{F} more than compensates the increase of the emission factor, and hence $q(x)$ decreases with increasing r_t .

Signal interval

As has been shown in Figs 4.16 and 4.18, the signal interval lies approximately in the range $300 \sim 800$ m. At first, the simulation was run for the signal interval $2\pi R$ in 300, 400, 500, 600, 700 m. However, for $2\pi R = 300$ and 400 m, the resulting queue length was about 250 m, and hence signal region exceeded the signal interval. Hence, the simulation range was shrunk to 450, 500, 600, 700 m,

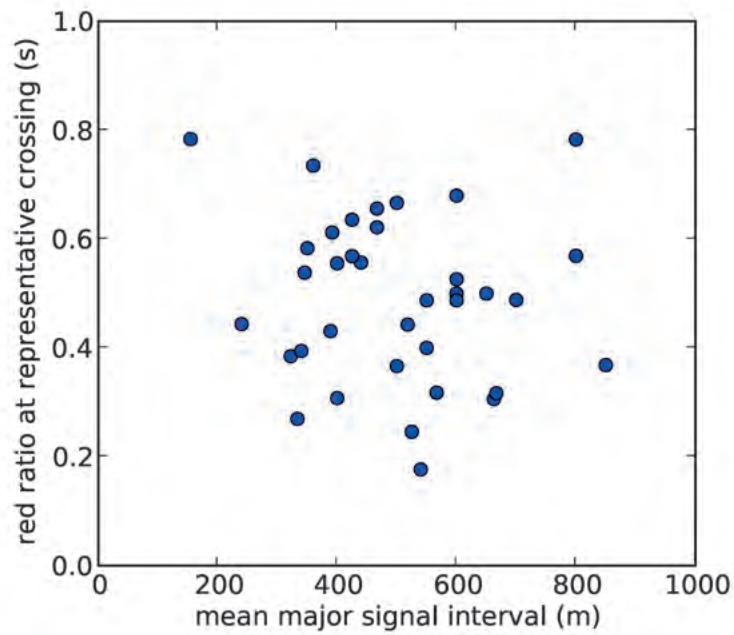


Figure 4.17: Red ratio of the signals in the routes relevant to the SORA project. The data are extracted from H17 traffic census.

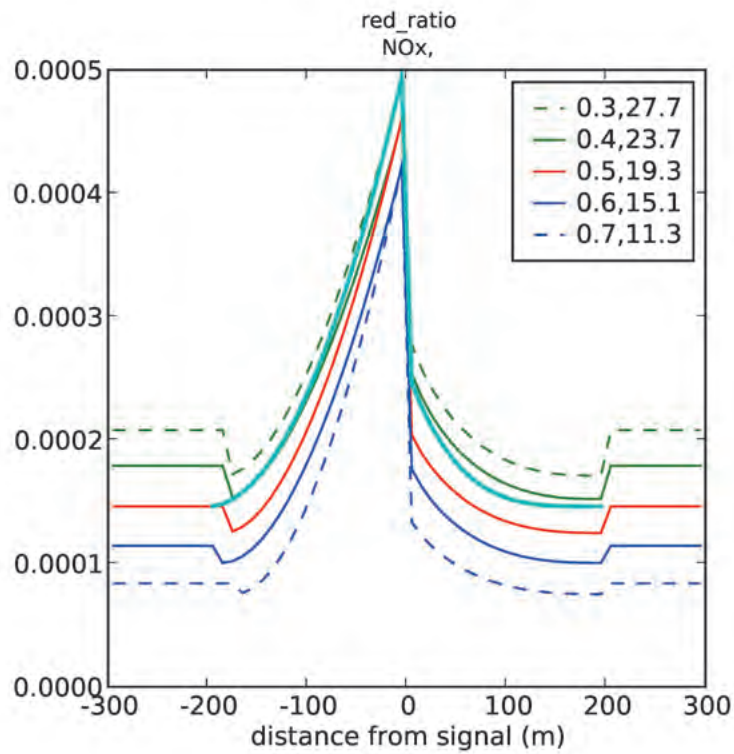


Figure 4.18: Dependence of $q(x)$ on the red ratio r_t . The legend indicates r_t and \bar{V} (km/h).

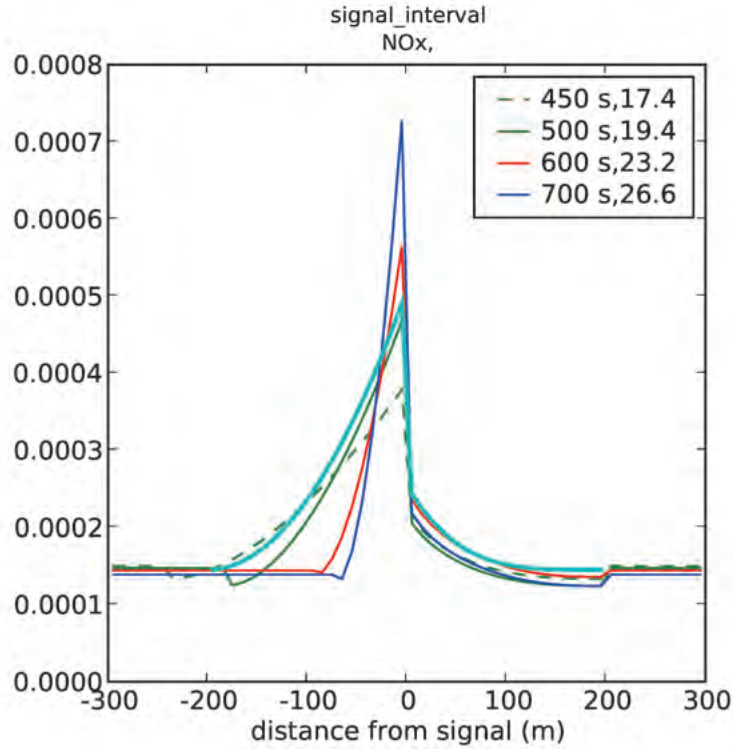


Figure 4.19: Dependence of $q(x)$ on the signal interval $2\pi R$. The legend indicates $2\pi R$ and \bar{V} (km/h).

and the results are shown in Fig. 4.19. The other parameters are

$$K = 18, \quad r_t = 0.5, \quad V_m = 60 \text{ km/h}, \\ T_c = 160, \quad \text{sedan : normal truck} = 1 : 1.$$

As the signal interval increases, the emission profile has a sharper peak.

Vehicle number

The vehicle number K is varied in 16, 18, 20, 22, and 24. Other parameters are

$$r_t = 0.5, \quad 2\pi R = 500 \text{ m}, \quad V_m = 60 \text{ km/h}, \\ T_c = 160, \quad \text{sedan : normal truck} = 1 : 1.$$

The result is shown in Fig. 4.20 From $K = 16$ to 20, the queue length increases relatively rapidly and the emission peak at the signal decreases. From $K = 20$ to 24, the queue length almost saturates and the emission peak at the signal increases.

Vehicle composition

Notable features of H17 traffic census at the SORA-project-related sites are summarized below.

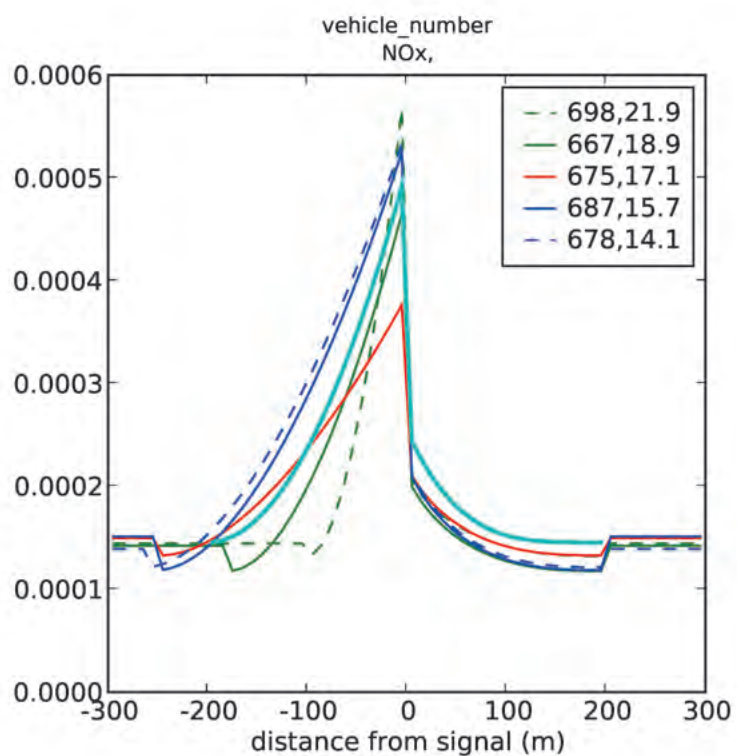


Figure 4.20: Dependence of $q(x)$ on the vehicle number K . The legend indicates \bar{F} (1/h) and \bar{V} (km/h). The number K of vehicles is 16, 18, 20, 22, 24 from the top of the legend.

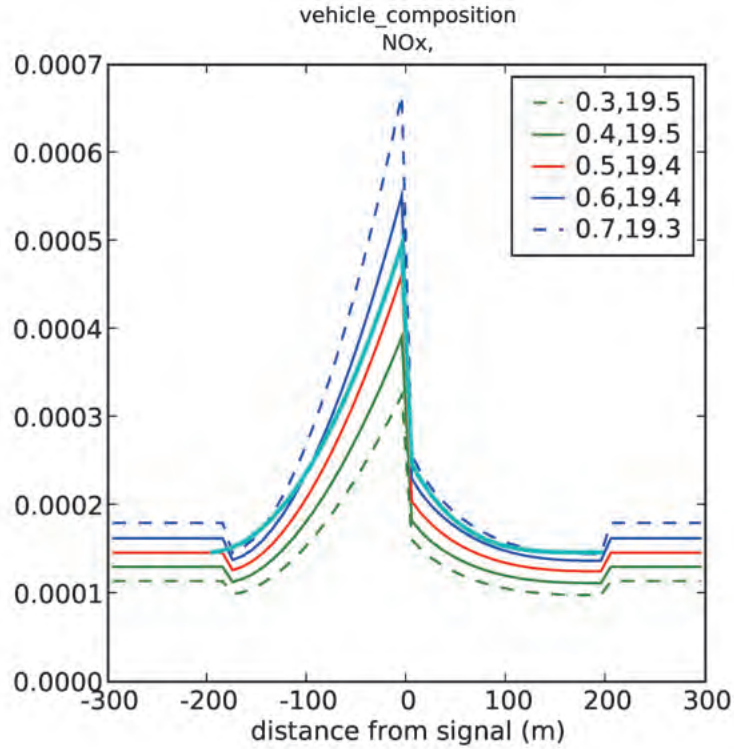


Figure 4.21: Dependence of $q(x)$ on the ratio of normal trucks. The legend indicates normal-truck ratio and \bar{V} (km/h).

- On non-highways, the ratio is high at night and low in the daytime.
- In the daytime, the ratio is in the range of $0.3 \sim 0.6$.
- The ratio differs with roads. High values (~ 0.6) are observed on bypasses of non-highways.
- The ratio is almost the same for the opposite directions on the same road.

The simulation is run for the normal-truck ratio in 0.3, 0.4, 0.5, 0.6, 0.7.

$$K = 18, \quad r_t = 0.5, \quad 2\pi R = 500 \text{ m}, \quad V_m = 60 \text{ km/h}, \\ T_c = 160.$$

The results are shown in Fig. 4.21. As the normal-truck ratio increases, the emission rate also increases, which is a natural consequence of the larger emission factor of normal trucks. The increase is more pronounced in the signal region because normal truck's emission factor increases more rapidly than sedan as \bar{V} decreases.

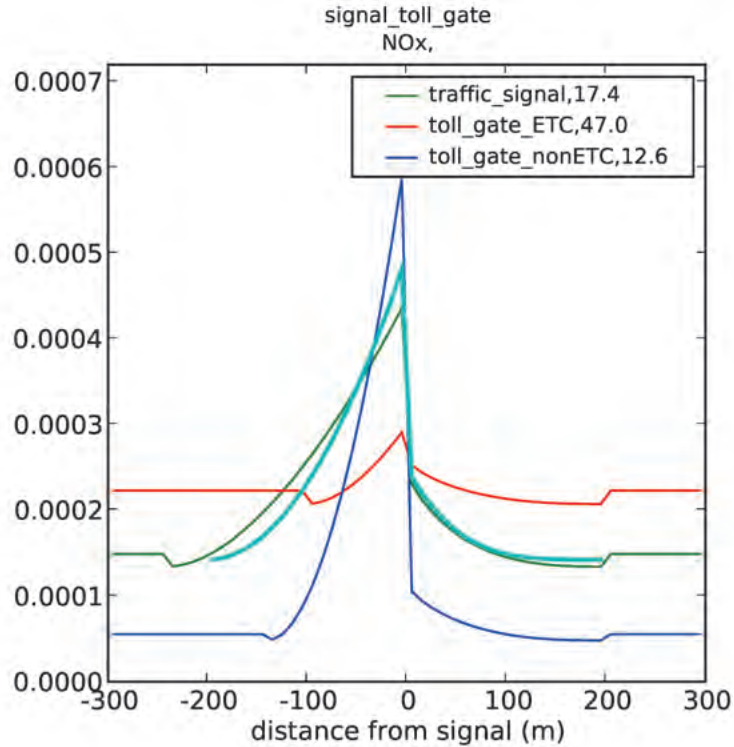


Figure 4.22: Dependence of $q(x)$ on the type of toll gate. The legend indicates toll-gate type and \bar{V} (km/h).

Toll gate

Today, highway toll gates are equipped with the ETC (Electronic Toll Collection) system, which reduces the payment time drastically. Here, the simulation is run for ETC and non-ETC cases. The toll-gate parameters are

$$\begin{array}{ll} \text{non-ETC} & T_c = 10 \text{ s} \\ \text{ETC} & T_c = 0.2 \text{ s} \end{array}$$

The other parameters are

$$\begin{aligned} 2\pi R &= 1000 \text{ m}, & V_m &= 80 \text{ km/h}, \\ r_t &= 1.0, & \text{sedan : normal truck} &= 1 : 1. \end{aligned}$$

The results are shown in Fig. 4.22. For the ETC case, the increase in the emission near the gate is much smaller than the non-ETC case. For comparison, the traffic-signal case is co-plotted for the typical parameter values ($T_c = 160$ s, $2\pi R = 500$ m, $V_m = 60$ km/h, $r_t = 0.5$, sedan:normal truck = 1:1). We observe that the traffic-signal case is about the middle of the ETC and the non-ETC cases. Since about half of the current toll gates are ETC, we may use this typical traffic-signal profile for toll gates.

4.2.3 Representative profile

Problems in applying the model to individual cases

As shown in the previous section, the simulation model produces emission profiles for given traffic and signal conditions. The input parameters are available from survey database such as traffic census. However, application of the simulation model to individual roads is not practical for the following reasons.

- Difficulty of estimating \bar{V} from \bar{F}

The simulation model takes K , or vehicle density, as an input, and produces \bar{F} and \bar{V} for the given condition. However, it is \bar{F} not K that is normally monitored in traffic surveys. Hence, \bar{V} , the essential parameter to calculate $q(x)$, can only be obtained by running the simulation for a range of K , plot a parametric curve $(\bar{F}(K), \bar{V})$, and then find \bar{V} for the concerned value of \bar{F} . As shown in Fig. 4.11(b), however, typical $\bar{F} - \bar{V}$ relationship has steep gradient in large \bar{F} region. This behavior agrees with the experience that traffic jam starts suddenly in an otherwise smooth but dense traffic flow. Therefore, \bar{V} obtained from \bar{F} through the simulation run may involve a large error. This error is serious since the traffic in urban area where estimation of $q(x)$ is often needed is usually close to saturation. There can be various sources of errors. Firstly, the simulation model is merely a crude approximation to the real traffic, and hence curves like Fig. 4.11(b) are not credible quantitatively. Secondly, the monitored \bar{F} is usually a one-time measurement on a day once in a few years. Chances that the monitored \bar{F} is close to the long-time average that is needed in environmental assessment may be relatively high but up to about 10% error should be expected. As can be observed in Fig. 4.11(b), 10% difference in \bar{F} in the large-value region results in considerable difference in \bar{V} . Thirdly, even if the long-time averaged traffic flow rate is available through, for example, automatic traffic counters, the \bar{F} value per lane may not be correct. The simulation input must be per-lane \bar{F} since the model assumes a single-lane traffic. On the real roads, however, the effective number of lanes usually differs from that marked on the roads. Some roads have the outermost lanes occupied by curb-parking vehicles, and others distribute vehicles into different lanes according to the destination or the vehicle type. Hence, (monitored traffic flow rate) / (number of lanes) may not be a good estimate of \bar{F} .
- Sensitivity of $q(x)$ to input parameters

As shown in the previous section, the emission profile $q(x)$ is sensitive to some parameters. Sensitive ones are the vehicle density K , the signal interval $2\pi R$, the vehicle composition, and the signal type. Relatively insensitive ones are the signal cycle T_c and the red ratio r_t . Since the runs in the previous section were conducted in the parameter range of the real variation, the magnitude of the variation of $q(x)$ can be appreciated from the results. Since both the input parameters and the simulation model

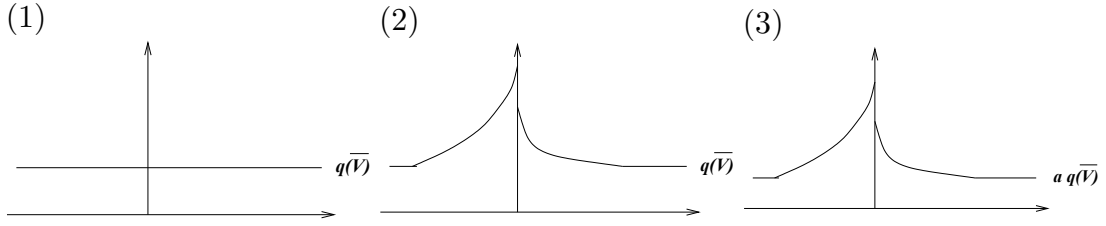


Figure 4.23: Procedure to maintain the total emission rate. a is the multiplication constant.

involve errors, applying the model to individual parameter sets produces intractable and low-quality variety of $q(x)$.

Representative profile formula

As explained above, it is not practical to apply the simulation model to individual traffic and signal conditions. Instead, we propose a simple analytical formula that approximates the simulated $q(x)$ for a typical set of parameters. The proposed formula is

$$\begin{cases} (q_1 - q_0) \left(\frac{x+L_q}{L_q} \right)^2 + q_0 & -L_q < x < 0 \\ \left(\frac{1}{2}q_1 - q_0 \right) \left(\frac{x-L_F}{L_F} \right)^4 + q_0 & 0 \leq x < L_F, \end{cases} \quad (4.69)$$

where $q_1 = 3.5q_0$ and $L_q = L_F = 200$ m. The thick cyan curves in Figs 4.16, 4.18, 4.19, 4.20, 4.21 and 4.22 indicate the proposed profiles with q_0 defined as the average of the plotted cases outside the signal region.

Global emission conservation

The overall emission rate $\bar{q}(\bar{V})$ per length in an interval including many signals is calculated by equation (4.30). If the length of the interval is \mathcal{L} , the total emission rate is $\bar{q}(\bar{V})\mathcal{L}$. This total value must be conserved after applying the near-signal profile (4.69).

For simplicity, we first consider the case where there is just one signal in the interval. The emission rate profile is calculated as follows.

- (1) Set a uniform value $\bar{q}(\bar{V})$ throughout the interval.
- (2) Apply the near-signal profile (4.69) with $q_0 = \bar{q}(\bar{V})$. At this stage, the total emission rate is larger than $\bar{q}(\bar{V})\mathcal{L}$.
- (3) Multiply the emission rate by a constant factor so that the total emission rate equals $\bar{q}(\bar{V})\mathcal{L}$.

The procedure is illustrated in Fig. 4.23 The constant factor in (3) can be calculated analytically, but as described in §4.2.4, such an analytical expression is not used in the numerical code.

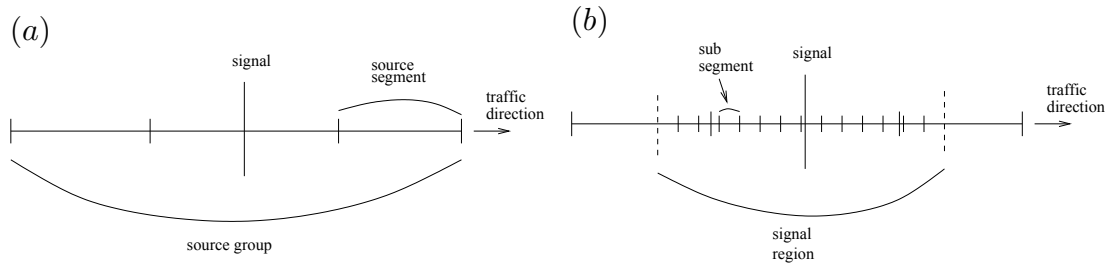


Figure 4.24: Outline of modifying source segments. (a) Original data in `gr_sources.dat`. (b) Source segments are divided in the signal region.

The procedure is basically the same when there are multiple signals in the interval. Problem arises when neighboring signal regions overlap, which can occur in reality as mentioned in §4.2.2. In such a case, the division of the signal regions is set at the mid-point of the signals and the profile (4.69) is applied to each signal region. Normally, $q(x)$ becomes discontinuous at the division point. More details are explained in the next section.

4.2.4 Modification to sources.dat

Overview

This section describes the detailed procedure of modifying the MCAD input file `gr_sources.dat` in accordance to the emission enhancement in the near-signal region. (For details of the MCAD input files, readers are referred to the MCAD user guide available at <http://sourceforge.net/projects/mcad/files/>) The file `gr_sources.dat` contains information of the source location and strength. Each line in the file corresponds to a linear segment of the emission source. The format of a line is

$$G \ I \ X0 \ Y0 \ Z00 \ Z01 \ X1 \ Y1 \ Z10 \ Z11 \ W \ Q \ \sigma_{y0} \ \sigma_{z0}.$$

G denotes the source group index whose meaning is explained later. I is the source segment index used in the original emission database. (X_i, Y_i, Z_{i0}) are the coordinates in the geographical system (X = north, Y = south, Z = vertical), $i = 0$ is the beginning and $i = 1$ is the end point. Z_{10} and Z_{11} are not used. W is the width of the source and Q is the emission rate in the segment. σ_{y0} and σ_{z0} are the initial diffusion widths in the horizontal and the vertical directions, respectively. Source segments in a source group G have the same diurnal variation of Q .

If a source segment overlaps with a signal region, the overlapping part is divided and the near-signal emission profile (4.69) is applied. After applying the near-signal profiles for all the source segments overlapping signal regions, the emission rate is multiplied uniformly by a constant so that the sum of Q in the `gr_sources.dat` file is conserved. Finally, the modified source segments are written out as a new file named, for example, `signal_gr_sources.dat`. Fig. 4.24 illustrates the procedure.



Figure 4.25: Signal example. At this Chitosedai crossing on Tokyo Loop8 (wider road running top to bottom), there are four major stop lines, which are to be recorded as signal shapefile.

Signal shape

A signal is identified by a line segment representing the stop lines. Hence, for a normal two-direction road, there are two line segments for a signal (Fig. 4.25). For automatic geometrical manipulation, the line segments representing signals are recorded as elements in a geographical database.

Source division

For each signal, source segments are divided by the following procedures.

- (1) For each signal, the whole source segments are searched for the nearest and sufficiently perpendicular one. If the signal and the source segments crosses, then the source segment immediately qualifies. If there is no such a source segment, the one closest and sufficiently perpendicular to the signal segment is selected.
- (2) The cross point between the signal segment and the selected source segment is calculated. If there is no cross point within the range of the segments, the cross point is found on the extended lines. A signal coordinate is defined with the cross point as the origin and directed from the node 0 to 1. The coordinate values s_0 and s_1 are calculated at the end nodes 0 and 1, respectively.
- (3) If the source segment overlaps with the signal's profile region $[-L_q, L_F]$, then the signal segment is divided into sub-segments and is given enhanced emission rate according to equation (4.69). The detail of this process is described later. If the segment has already been divided by a different

signal, which can occur by the next process (4), the previous division is reset and the division by this signal is applied if the source segment crosses the signal within the range of the segment or this signal is closer to the source segment than the other signal is.

- (4) Examine whether the neighboring source segments are within the signal profile region, and if so, divide the neighboring source segments. This examination is continued in both directions until the neighboring source segments are fully outside the signal profile region.

A source segment is divided if the segment overlaps with the signal profile region. There are four patterns of overlapping. Fig. 4.26 shows these patterns denoting the source segment as AB and signal profile region as EF . Note that the symbol Q is also used for the emission rate in a source segment, but the meanings can be distinguished by the context. We denote the end points of the overlapping region as P and Q with the respective signal coordinates s_P and s_Q . For each pattern, the geographical coordinates of P and Q , and the values of s_P and s_Q are given as follows. Note that point names are used to represent either X or Y coordinates of the points.

(1) $s_A < -L_q, -L_q < s_B < L_F$

$$P = E = \frac{(s_B + L_q)A + (-L_q - s_A)B}{s_B - s_A}, \quad s_P = -L_q,$$

$$Q = B, \quad s_Q = s_B.$$

(2) $-L_q < s_A, s_B < L_F$

$$P = A, \quad s_P = s_A,$$

$$Q = B, \quad s_Q = s_B.$$

(3) $-L_q < s_A < L_F, L_F < s_B$

$$P = A, \quad s_P = s_A,$$

$$Q = F = \frac{(s_B - L_F)A + (L_F - s_A)B}{s_B - s_A}, \quad s_Q = L_F.$$

(4) $s_A < -L_q, L_F < s_B$

$$P = E = \frac{(s_B + L_q)A + (-L_q - s_A)B}{s_B - s_A}, \quad s_P = -L_q,$$

$$Q = F = \frac{(s_B - L_F)A + (L_F - s_A)B}{s_B - s_A}, \quad s_Q = L_F.$$

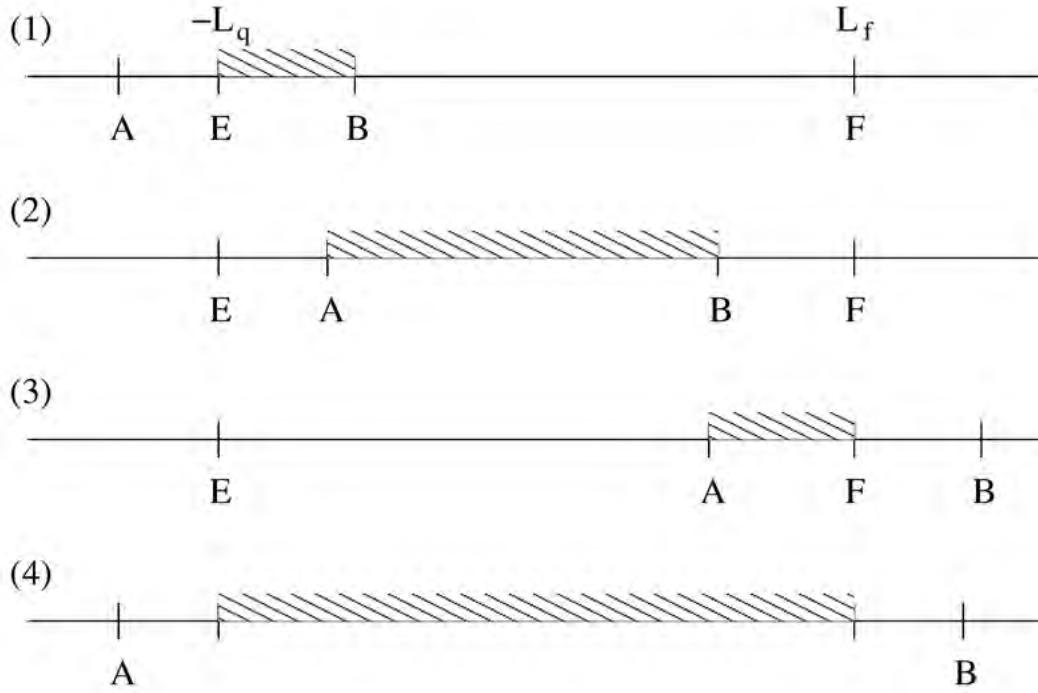


Figure 4.26: Signal-source overlapping patterns.

If the signal profile region is to be divided into sub-segments of length Δs , there would be

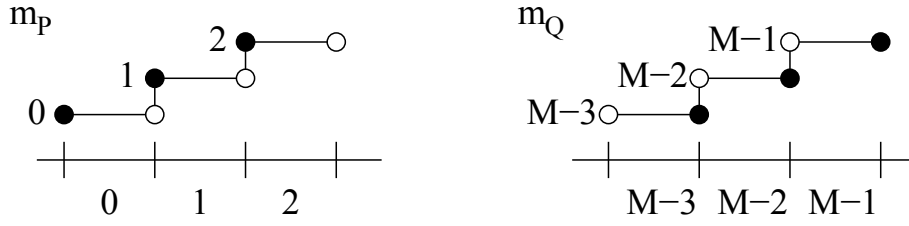
$$M = \frac{L_F + L_q}{\Delta s} \quad (4.70)$$

sub-segments in the signal profile region. The value of Δs should be chosen such that M becomes an integer. For $L_F = L_q = 200$ m, we usually set $\Delta s = 10$ m. Indexing the sub-segments from 0 to $M - 1$, the indices of the sub-segments containing P and Q become

$$m_P = \text{floor} \left(\frac{s_P + L_q}{\Delta s} \right),$$

$$m_Q = \text{ceil} \left(\frac{s_Q + L_q}{\Delta s} \right) - 1.$$

The above functions are illustrated in Fig. 4.27. Using these indices, sub-segments within PQ are shown in Fig. 4.28. New smaller segments ($R_0R_1, R_{m_Q-m_P}R_{m_Q-m_P+1}$) are defined inside next to P and Q . Note that if P or Q coincides with a nodal point of the original M -divided sub-segments, the definition of m_P and m_Q prevent creation of zero-length new segment (cf. Fig. 4.27).


 Figure 4.27: m_P and m_Q .

The geographical coordinates of the new nodal points $R_0 \sim R_{m_Q - m_P + 1}$ become

$$\begin{aligned}
 R_0 &= P, \\
 R_i &= \frac{\{(m_P + i)\Delta s - (s_P + L_q)\} Q + \{(s_Q + L_q) - (m_P + i)\Delta s\} P}{s_Q - s_P} \\
 &\quad (i = 1, 2, \dots, m_Q - m_P), \\
 R_{m_Q - m_P + 1} &= Q,
 \end{aligned}$$

where P , Q or R are to be interpreted as either X or Y coordinates of these points.

The emission rate Q'_m in the m 'th sub-segment is calculated by

$$Q'_m = \frac{Q}{M} l_m \alpha_{m_P + m}, \quad (4.71)$$

where l_m is the length of the m 'th segment and $\alpha_{m_P + m}$ is the profile multiplier given by setting $q_0 = 1$ in equation (4.69) at $x = -L_q + (m_P + m + 1/2)\Delta s$, *i.e.* at the mid-point of the $(m_P + m)$ 'th sub-segment of the original M -divided signal sub-segment. The length l_m is given by

$$m_Q > m_P$$

$$\begin{aligned}
 l_0 &= (m_P + 1)\Delta s - (s_P + L_q), \\
 l_i &= \Delta s \quad (i = 1, 2, \dots, m_Q - m_P - 1), \\
 l_{m_Q - m_P} &= (s_Q + L_q) - m_Q \Delta s,
 \end{aligned}$$

$$m_Q = m_P$$

$$l_0 = s_Q - s_P$$

The emission rate outside the signal profile region is distributed in proportion to the length.

Source group

In emission modification due to signals, source segments should be ordered with respect to geometrical continuity. Therefore, if the source segments are originally sorted into groups of the same pattern of diurnal variation of Q as required

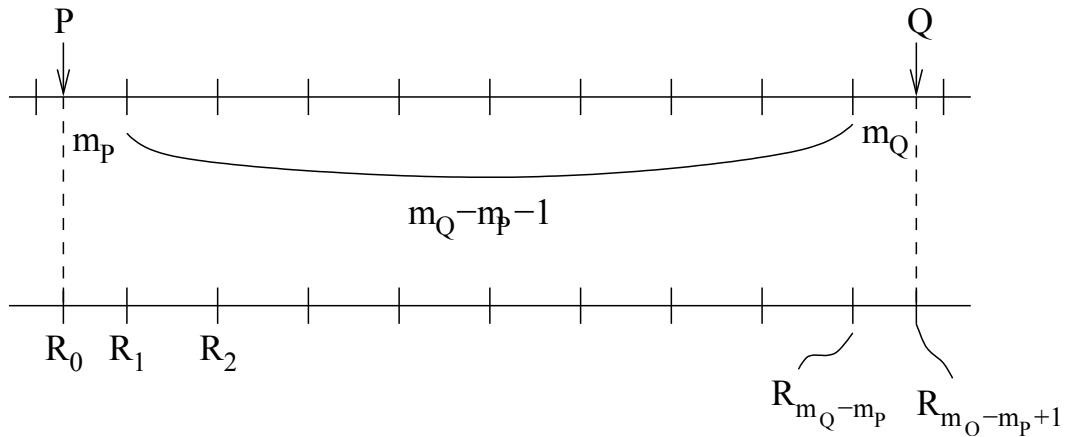
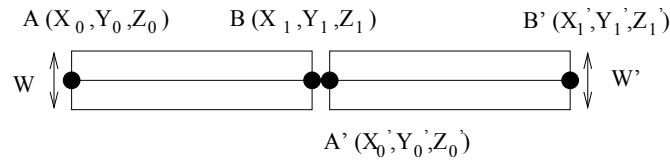


Figure 4.28: Sub-segments in the overlapping region PQ .

(a)



(b)

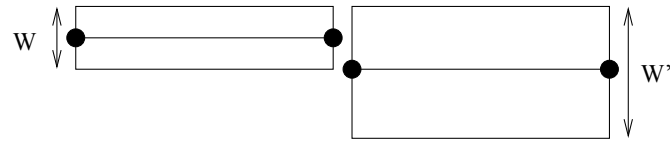


Figure 4.29: Notations for the criteria for source continuity. See text for explanation.

for calculating annual averages efficiently, the source segments need to be re-grouped into continuous members.

When the coordinates of the end points and source widths are given as in Fig. 4.29(a), we define the continuity criteria by

$$|Z_1 - Z'_0| < \epsilon,$$

$$d < \frac{1}{2} |W - W'| + \epsilon,$$

where $d = \sqrt{(X_1 - X'_0)^2 + (Y_1 - Y'_0)^2}$ is the horizontal distance between B and A' , and ϵ is the minimum meaningful distance for the considered length scale. Typical value is $\epsilon = 1$ m. The second criterion allows connection of roads with different widths as shown in Fig. 4.29(b). Because of the above criteria, source segments must be defined such that the source nodes 0 and 1 are ordered in the same direction as the traffic flow. Otherwise, the correct connecting end point cannot be found.

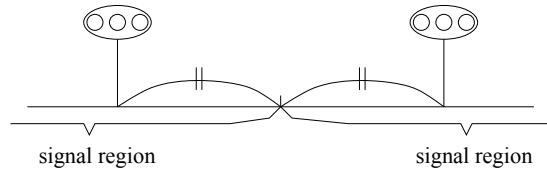


Figure 4.30: Signal region division when two signals are close to each other.

Global emission conservation

The sum of Q' after applying the signal-region emission enhancement is larger than that in the original `gr_sources.dat` file. Since the total emission rate is calculated from the travel speed over sufficiently long distance including many signals, the original sum of Q is the correct value and must be conserved after modification for signals. Here, emission conservation is achieved by multiplying the emission rate in a source group by a uniform factor β . The value of β is defined by

$$\beta \sum Q' = \sum Q, \quad (4.72)$$

where the summation is over all source segments in a source group. Each source group has a different value of β . The adjusted emission rate is thus $\beta Q'$. The divided source segments with the adjusted emission rate $\beta Q'$ are written out as a modified MCAD input file, say, `signal_gr_sources.dat`.

Special cases

Overlapping signal regions So far, it has been assumed that signals are sufficiently separated so that neighboring signal regions do not overlap. In reality, distance between signals is often less than $L_f + L_q = 400$ m (see Fig. 4.17). In such cases, the signal coordinate of a point between signals is defined as that relative to the closer signal (Fig. 4.30). In other words, the region between the signals is divided at the mid-point with the left-hand side belonging to the left signal and the right-hand side to the right signal.

Long segments The source segments are usually divided into lengths less than the signal separation distance. In some cases, however, a single source segment includes multiple signals. In such a case, the source segment has multiple signal regions. It is possible to write a computational code that accommodates such a situation, but it is easier to divide the long segment at the mid-points of neighboring signals so that a source segment includes at most one signal. We take this latter option, and divide long source segments by a program outside MCAD.

Bundled lanes So far, we assumed that a source segment has a definite direction. However, if the traffic census data are available only as the sum of the two opposite directions, the source segments can only be expressed as a wide segment spanning the whole road width. In such a case, signals expressed as

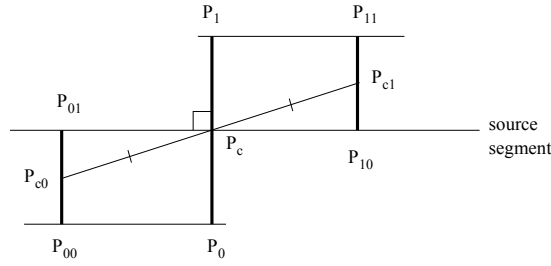


Figure 4.31: Combined signal.

stop lines of both directions do not make sense. Here, the signals are combined into an intermediate line segment and the corresponding emission profile is calculated as the average of the opposite direction profiles.

- Signal combination

Two signals are combined if they satisfy the following conditions.

- (1) They are the closest pair for both.
- (2) They are sufficiently parallel.
- (3) The nearest source segment with almost the same height as the signals have width close to the combined span of the signal segments.

The combined signal is constructed as follows (Fig. 4.31). If the source segment is represented by

$$ax + by - c = 0, \quad a^2 + b^2 = 1, \quad (4.73)$$

and the mid-points of the signal segments are P_{0c} and P_{1c} , the line equation of the combined signal is defined by

$$-b(x - P_{c,x}) + a(y - P_{c,y}) = 0, \quad (4.74)$$

where P_c is the mid-point of $P_{0c}P_{1c}$. Hence, the combined signal is perpendicular to the source segment and passes through P_c . Of the end points of the original signal segments, the ones more distant from the source segment (P_{00} and P_{11} in the case of Fig. 4.31) are selected and the lines through them and parallel to the source segment are calculated as

$$a(x - P_{iM,x}) + b(y - P_{iM,y}) = 0, \quad (4.75)$$

where $i = 0, 1$ and M denotes the farther end point from the source line (4.73). Then, the end points P_0 and P_1 of the combined signal is obtained as the cross points between the above line (4.75) and the new signal line (4.74).

- Combined emission profile

The combined emission profile is calculated as the average of the opposite-direction profiles with the peak at the combined signal. For generality, we

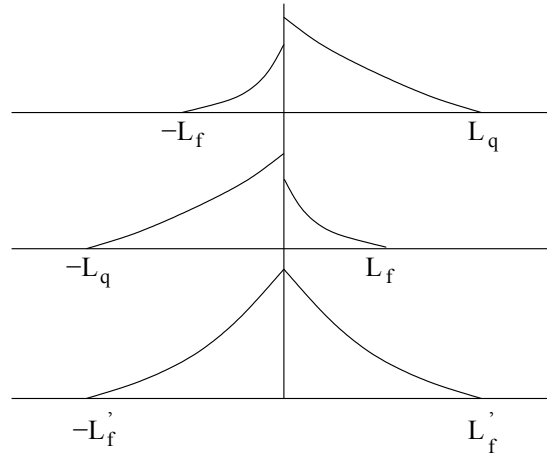


Figure 4.32: Emission profile around a combined signal.

consider the case $L_q \neq L_f$ (Fig. 4.32). The original profile $\alpha(x)$ ($q_0 = 1$ in (4.69)) is discretized as

$$\alpha_i = \alpha \left(x = -L_q + \left(i + \frac{1}{2} \right) \Delta x \right), \quad i = 0 \sim M - 1,$$

$$M = \frac{L_q + L_f}{\Delta x}.$$

The combined signal region is expanded to $[-L'_q, L'_f]$ where

$$L'_q = L'_f = \max(L_q, L_f). \quad (4.76)$$

The number M' of discretized sub-segments becomes

$$M' = \frac{L'_q + L'_f}{\Delta x}. \quad (4.77)$$

Then, an intermediate profile α''_i is defined by

$$\alpha''_i = \begin{cases} \begin{cases} \alpha_i & (i = 0 \sim M - 1) \\ 0 & (i = M \sim M' - 1) \end{cases} & (L_q \geq L_f) \\ \begin{cases} 0 & (i = 0 \sim M' - M - 1) \\ \alpha_{i-(M'-M)} & (i = M' - M \sim M' - 1) \end{cases} & (L_q < L_f) \end{cases} \quad (4.78)$$

Finally, the combined profile α'_i is given by

$$\alpha'_i = \frac{1}{2}(\alpha''_i + \alpha''_{M'-1-i}) \quad i = 0 \sim M' - 1. \quad (4.79)$$

4.2.5 Numerical integration of non-idling emission component

Since equation (4.64) has different forms in different domains, numerical integration of equation (4.66) is a little complicated. The range where $R(x, x_0)$ becomes the super-ellipse (the second branch of equation (4.64)) is shown in Fig. 4.33. For a given x , the integrand becomes as follows.

$$\underline{L_f < L_q}$$

$$-L_q \leq x \leq -L_q + L_f$$

$$\begin{array}{l} -L_q \leq x_0 \leq x \quad \text{super-ellipse} \\ x \leq x_0 \leq 0 \quad \quad \quad AR_0 \end{array}$$

$$-L_q + L_f \leq x \leq 0$$

$$\begin{array}{l} -L_q \leq x_0 \leq x - L_f \quad \quad \quad AR_0 \\ x - L_f \leq x_0 \leq x \quad \quad \quad \text{super-ellipse} \\ x \leq x_0 \leq 0 \quad \quad \quad \quad \quad AR_0 \end{array}$$

$$0 \leq x \leq L_f$$

$$\begin{array}{l} -L_q \leq x_0 \leq x - L_f \quad \quad \quad AR_0 \\ x - L_f \leq x_0 \leq 0 \quad \quad \quad \text{super-ellipse} \end{array}$$

$$\underline{L_f > L_q}$$

$$-L_q \leq x \leq 0$$

$$\begin{array}{l} -L_q \leq x_0 \leq x \quad \text{super-ellipse} \\ x \leq x_0 \leq 0 \quad \quad \quad AR_0 \end{array}$$

$$0 \leq x \leq -L_q + L_f$$

$$-L_q \leq x_0 \leq 0 \quad \text{super-ellipse}$$

$$-L_q + L_f \leq x \leq L_f$$

$$\begin{array}{l} -L_q \leq x_0 \leq x - L_f \quad \quad \quad AR_0 \\ x - L_f \leq x_0 \leq 0 \quad \quad \quad \text{super-ellipse} \end{array}$$

Denoting the super-elliptic part of (4.64) as $S_e(x_0, x)$, the integral (4.66) is divided as follows.

$$\underline{L_f < L_q}$$

$$-L_q \leq x \leq -L_q + L_f$$

$$\mathcal{R}(x) = A \int_{-L_q}^x S_e(x_0, x) \alpha(x_0) dx_0 + A \int_x^0 R_0 \alpha(x_0) dx_0$$

$$-L_q + L_f \leq x \leq 0$$

$$\begin{aligned} \mathcal{R}(x) = A \int_{-L_q}^{x-L_f} R_0 \alpha(x_0) dx_0 + A \int_{x-L_f}^x S_e(x_0, x) \alpha(x_0) dx_0 \\ + A \int_x^0 R_0 \alpha(x_0) dx \end{aligned}$$

$$0 \leq x \leq L_f$$

$$\mathcal{R}(x) = A \int_{-L_q}^{x-L_f} R_0 \alpha(x_0) dx_0 + A \int_{x-L_f}^0 S_e(x_0, x) \alpha(x_0) dx_0$$

$$\underline{L_f > L_q}$$

$$-L_q \leq x \leq 0$$

$$\mathcal{R}(x) = A \int_{-L_q}^x S_e(x_0, x) \alpha(x_0) dx_0 + A \int_x^0 R_0 \alpha(x_0) dx_0$$

$$0 \leq x \leq -L_q + L_f$$

$$\mathcal{R}(x) = A \int_{-L_q}^0 S_e(x_0, x) \alpha(x_0) dx_0$$

$$-L_q + L_f \leq x \leq L_f$$

$$\mathcal{R}(x) = A \int_{-L_q}^{x-L_f} R_0 \alpha(x_0) dx_0 + A \int_{x-L_f}^0 S_e(x_0, x) \alpha(x_0) dx_0$$

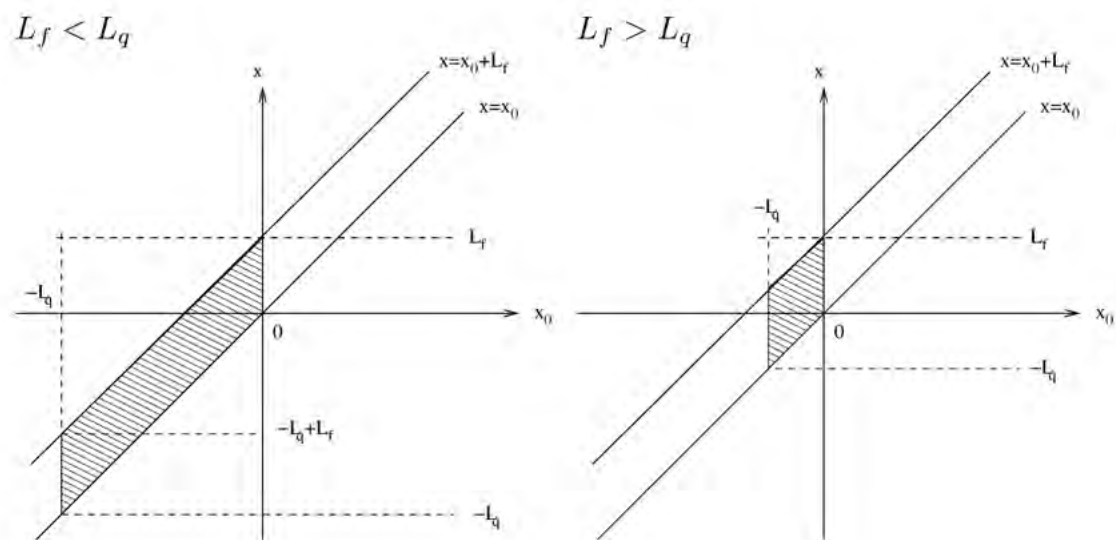


Figure 4.33: The range where $R(x, x_0)$ becomes the super-ellipse form.

Chapter 5

Summary

This report described a new roadside air-pollution prediction model MCAD. MCAD is based on the mass-conservation (MC) principle and the solution to the advection-diffusion (AD) equation. By incorporating previous experimental results in the MC process, MCAD can account for the effect of obstacles such as buildings and road structures at a substantially lower cost than conventional computational fluid dynamics models. By defining eddy diffusivity as a function of distance from emission sources, MCAD can simulate the Lagrangian nature of passive diffusion near emission sources. MCAD includes components that can account for enhanced horizontal diffusion due to wind meandering and non-uniform emission distribution due to traffic signals.

The scope of MCAD is limited to (1) non-reactive or conservative species such as black carbon or nitrogen oxides, (2) contribution by the emission sources inside the calculation domain, (3) spatial extent of up to about 600 meters in diameter, (4) neutral atmospheric stability, and (5) influences of the surface boundary layer where the Earth's rotation has negligible effect.

The model MCAD is under continuous development. As mentioned in Chapter 2, the coefficients for eddy diffusivity are determined empirically. We have collected as many experimental data as possible to deduce reliable coefficients, but as demonstrated in the comparison exercises in Chapter 3, the performance of MCAD cannot be said satisfactory for general purposes. Our evaluation of MCAD is that it is suited for statistical assessment of concentration at many target points, but not suited for concentration analysis at a particular point. To improve the model performance, the model parameters as well as the model structure need to be revised based on further experimental or numerical results. By 'numerical', we imply methods such as LES, which is very costly but proven to be reasonably accurate.

The model MCAD is implemented as a C code that can be run on Linux computers. The source code together with a user guide and examples is available at <https://sourceforge.net/projects/mcad/>. Further development of MCAD will be carried out on this sourceforge web site.

Bibliography

- AGARWAL, P., YADAV, A. K., GULATI, A., RAMAN, S., RAO, S., SINGH, M. P., NIGAM, S. & REDDY, N. 1995 Surface layer turbulence processes in low wind speeds over land. *Atmospheric Environment* **29**, 2089–2098.
- ENVIRONMENTAL PROTECTION AGENCY, U.S. 1994 User's guide for the Industrial Source Complex (ISC3) dispersion models. .
- AL-JIBOORI, M. H., XU, Y. & QIAN, Y. 2002 Local similarity relationships in the urban boundary layer. *Boundary-Layer Meteorology* **102**, 63–82.
- ANFOSSI, D., OETTL, D., DEGRAZIA, G. & GOULART, A. 2005 An analysis of sonic anemometer observations in low wind speed conditions. *Boundary-Layer Meteorology* **114**, 179–203.
- APSLEY, D. D. & CASTRO, I. P. 1997 Numerical modelling of flow and dispersion around Cinder Cone Butte. *Atmospheric Environment* **31**, 1059–1071.
- BARAD, M. L. 1958 Project Prairie Grass, A field program in diffusion. Vols I and II. Geophysical Research Papers No.59 AFCRC-TR-58-235. Air Force Cambridge Research Center.
- BATCHELOR, G. K. 1949 Diffusion in a field of homogeneous turbulence, I. Eulerian analysis. *Aust. J. Sci. Res.* **2**, 437–450.
- BERKOWICZ, R. 2000 OSPM – a parametrised street pollution model. *Environmental Monitoring and Assessment* **65**, 323–331.
- BLOCKEN, B., STATHOPOULOS, T., SAATHOFF, P. & WANG, X. 2008 Numerical evaluation of pollutant dispersion in the built environment: Comparisons between models and experiments. *Journal of Wind Engineering and Industrial Aerodynamics* **96**, 1817–1831.
- BRIGGS, G. A. 1973 Diffusion estimation for small emissions. *Tech. Rep.*. Air Resources Laboratory NOAA ARL Report ATDL-106.
- CARPENTIERI, M., ROBINS, A. G. & BALDI, S. 2009 Three-dimensional mapping of air flow at an urban canyon intersection. *Boundary-Layer Meteorology* **133**, 277–296.

BIBLIOGRAPHY

- CASTANS, M. & BARQUERO, C. G. 1994 A framework for the structure of a low windspeed field. *Boundary-Layer Meteorology* **69**, 137–147.
- CERC 2007 *ADMS 4 User Guide*. Cambridge Environmental Research Consultants Ltd., <http://www.cerc.co.uk>.
- CHANG, J. C. & HANNA, S. R. 2004 Air quality model performance evaluation. *Meteorology Atmos. Phys.* **87**, 167–196.
- CHENG, H. & CASTRO, I. P. 2002 Near wall flow over urban-like roughness. *Boundary-Layer Meteorology* **104**, 229–259.
- COCEAL, O. & BELCHER, S. E. 2004 A canopy model of mean winds through urban areas. *Quarterly Journal of the Royal Meteorological Society* **130**, 1349–1372.
- COUNIHAN, J., HUNT, J. C. R. & JACKSON, P. S. 1974 Wakes behind two-dimensional surface obstacles in turbulent boundary layers. *Journal of Fluid Mechanics* **64**, 529–563.
- CSANADY, G. T. 1973 *Turbulent Diffusion in the Environment*. D. Reidel Publishing Co.
- DAVIES, B. M. & THOMSON, D. J. 1999 Comparisons of some parametrizations of wind direction variability with observations. *Atmospheric Environment* **33**, 4909–4917.
- DEGRAZIA, G. & ANFOSSI, D. 1998 Estimation of the Kolmogorov constant C_0 from classical statistical diffusion theory. *Atmospheric Environment* **32**, 3611–3614.
- DEGRAZIA, G. A. & MORAES, O. L. L. 1992 A model for eddy diffusivity in a stable boundary layer. *Boundary-Layer Meteorology* **58**, 205–214.
- DIXON, N. S. & TOMLIN, A. S. 2007 A Lagrangian stochastic model for predicting concentration fluctuations in urban areas. *Atmospheric Environment* **41**, 8114–8127.
- ECKMAN, R. M. 1994 Influence of the sampling time on the kinematics of turbulent diffusion from a continuous source. *Journal of Fluid Mechanics* **270**, 349–375.
- EICHHORN, J. 1989 Entwicklung und anwendung eines dreidimensionalen mikroskaligen Stadtklima-Modells. Dissertation, Universität Mainz, Germany.
- EICHHORN, J. 1996 *Validation of a microscale pollution dispersal model*, pp. 539–548. Plenum Press, London.
- FACKRELL, J. E. & PEARCE, J. E. 1981 Parameters affecting dispersion in the near wake of buildings. *Tech. Rep.*. CEEB Report RD/M/1179/N81.

BIBLIOGRAPHY

- GJERSTAD, J., AASEN, S. E., ANDERSSON, H. I., BREVIK, I. & LOVSETH, J. 1995 An analysis of low-frequency maritime atmospheric-turbulence. *Journal of the Atmospheric Sciences* **52**, 2663–2669.
- GRIMMOND, C. S. B. & OKE, T. R. 1999 Aerodynamic properties of urban areas derived from analysis of surface form. *Journal of Applied Meteorology* **38**, 1262–1292.
- HAGISHIMA, A., TANIMOTO, J., NAGAYAMA, K. & MENO, S. 2009 Aerodynamic parameters of regular arrays of rectangular blocks with various geometries. *Boundary-Layer Meteorology* **132**, 315–337.
- HANNA, S. R. 1981*a* Diurnal variation of horizontal wind direction fluctuations in complex terrain at Geysers, Cal. *Boundary-Layer Meteorol.* **21**, 207–213.
- HANNA, S. R. 1981*b* Lagrangian and Eulerian time-scale relations in the daytime boundary layer. *Journal of Applied Meteorology* **20**, 242–249.
- HANNA, S. R. 1983 Lateral turbulence intensity and plume meandering during stable conditions. *Journal of Climate and Applied Meteorology* **22**, 1424–1430.
- HANNA, S. R., STRIMAITIS, D. G. & CHANG, J. C. 1958 Hazard response modeling uncertainty (a quantitative method) Vol II – Evaluation of commonly used hazardous gas dispersion models. *Tech. Rep.* ESL-TR-91-28. Sigma Research Corp.
- HARMAN, I. N., BARLOW, J. F. & BELCHER, S. E. 2004 Scalar fluxes from urban street canyons. Part II: Model. *Boundary-Layer Meteorology* **113**, 387–409.
- HAY, J. S. & PASQUILL, F. 1959 Diffusion from a continuous source in relation to the spectrum and scale of turbulence. *Adv. Geophys.* **6**, 345.
- HOFFMAN, J. D. 1992 *Numerical methods for engineers and scientists*. McGraw Hill.
- HOSKER, R. P. 1984 Flow and diffusion near obstacles. In *Atmospheric Science and Power Production* (ed. D. Randerson), pp. 241–326. National Technical Information Service, Springfield, VA, USA, publication DOE/TIC 27601.
- HOTCHKISS, R. S. & HARLOW, F. H. 1973 Air pollution transport in street canyons. *Tech. Rep.* EPA-R4-73-029.
- JAPAN WEATHER ASSOCIATION 2005 Report of survey and research on environment improvement. *Tech. Rep.* Environmental Restoration and Conservation Agency.
- JAPAN ENVIRONMENT AGENCY 2000 *Manual for regulation of total emission of nitrogen oxides*. Environmental Research and Control Center, Japan.

BIBLIOGRAPHY

- JOFFRE, S. M. & LAURILA, T. 1988 Standard deviations of wind speed and direction from observations over a smooth surface. *Journal of Applied Meteorology* **27**, 550–561.
- JOHNSON, W. B., LUDWIG, F. L., DABBERDT, W. F. & ALLEN, R. J. 1973 An urban diffusion simulation model for carbon monoxide. *Journal of Air Pollution Control Association* **23**, 490–498.
- KAIMAL, J. C. & FINNIGAN, J. J. 1994 *Atmospheric Boundary Layer Flows*. Oxford University Press.
- KAIMAL, J. C., WYNGAARD, J. C., YZUMY, Y. & COTÉ, O. R. 1972 Spectral characteristics of surface-layer turbulence. *Quarterly Journal of the Royal Meteorological Society* **98**, 563–589.
- KANDA, I. & YAMAO, Y. 2011 Velocity adjustment and passive scalar diffusion in and above an urban canopy in response to various approach flows. *Boundary-Layer Meteorology* **141**, 415–441.
- KANDA, I., YAMAO, Y., UEHARA, K. & OHARA, T. 2011 A wind-tunnel study on diffusion from urban major roads. *Journal of Wind Engineering and Industrial Aerodynamics* **99**, 1227–1242.
- KAPLAN, H. & DINAR, N. 1996 A Lagrangian dispersion model for calculating concentration distribution within a built-up domain. *Atmospheric Environment* **30**, 4197–4207.
- KOUCHI, A., OKABAYASHI, K., OKAMOTO, S., YOSHIKADO, H., YAMAMOTO, S., KOBAYASHI, K., ONO, N. & KOIZUMI, M. 2004 Development of a low-rise industrial source dispersion model (METI-LIS model). *International Journal of Environment and Pollution* **21**, 325–338.
- KRISTENSEN, L. & PANOFSKY, H. A. 1976 Climatology of wind direction fluctuations at Risø. *Journal of Applied Meteorology* **15**, 1279–1283.
- LEAHEY, D. M., HANSEN, M. C. & SCHROEDER, M. B. 1994 Variations of wind fluctuations observed at 10 m over flat terrain under stable atmospheric conditions. *Journal of Applied Meteorology* **33**, 712–720.
- LEONARDI, S. & CASTRO, I. P. 2010 Channel flow over large cube roughness: a direct numerical simulation study. *Journal of Fluid Mechanics* **651**, 519–539.
- LEUZZI, G. & MONTI, P. 1998 Particle trajectory simulation of dispersion around a building. *Atmospheric Environment* **32**, 203–214.
- LIU, C.-H. & BARTH, M. C. 2002 Large-eddy simulation of flow and scalar transport in a modeled street canyon. *Journal of Applied Meteorology* **41**, 660–673.
- LUMLEY, J. L. 1964 The spectrum of nearly inertial turbulence in a stably stratified fluid. *Journal of the Atmospheric Sciences* **21**, 99–102.

BIBLIOGRAPHY

- LYN, D. A., EINAV, E., RODI, W. & PARK, J. -H. 1995 A laser-doppler velocimetry study of ensemble-averaged characteristics of the turbulent near wake of a square cylinder. *Journal of Fluid Mechanics* **304**, 285–319.
- MACDONALD, R. W., GRIFFITHS, R. F. & HALL, D. J. 1998 An improved method for the estimation of surface roughness of obstacle arrays. *Atmospheric Environment* **32**, 1857–1864.
- MORIGUCHI, Y. & UEHARA, K. 1993 Numerical and experimental simulation of vehicle exhaust gas dispersion for complex urban roadways and their surroundings. *Journal of Wind Engineering and Industrial Aerodynamics* **46-47**, 689–695.
- NASER, T. M., KANDA, I., OHARA, T., SAKAMOTO, K., KOBAYASHI, S., NITTA, H. & NATAAMI, T. 2009 Analysis of traffic-related NO_x and EC concentrations at various distances from major roads in Japan. *Atmospheric Environment* **43**, 2379–2390.
- OETTL, D., ALMBAUER, R. A. & STURM, P. J. 2001 A new method to estimate diffusion in stable, low-wind conditions. *Journal of Applied Meteorology* **40**, 259–268.
- OETTL, D., GOULART, A., DEGRAZIA, G. & ANFOSSI, D. 2005 A new hypothesis on meandering atmospheric flows in low wind speed conditions. *Atmospheric Environment* **39**, 1739–1748.
- OGAWA, Y., DIOSEY, P. G., UEHARA, K. & UEDA, H. 1981 A wind tunnel for studying the effects of thermal stratification in the atmosphere. *Atmospheric Environment* **15**, 807–821.
- OGURA, Y. 1957 The influence of finite observation intervals on the measurement of turbulent diffusion parameters. *Journal of Meteorology* **14**, 176–181.
- OKE, T. R. 1987 *Boundary Layer Climates*, 2nd edn. Methuen, London.
- OKE, T. R. 1988 Street design and urban canopy layer climate. *Energy Bldng* **11**, 103–113.
- OLESEN, H. R. 1995 Regulatory dispersion modelling in Denmark. *International Journal of Environment and Pollution* **5**, 412–417.
- OLESEN, H. R., LARSEN, S. E. & HØJSTRUP, J. 1984 Modelling velocity spectra in the lower part of the planetary boundary layer. *Boundary-Layer Meteorology* **29**, 285–312.
- PANOFSKY, H. A. 1988 The effect of averaging time on velocity variances. *Meteorology Atmos. Phys.* **38**, 64–69.
- PANOFSKY, H. A., TENNEKES, H., LENSCHOW, D. H. & WYNGAARD, J. C. 1977 The characteristics of turbulent velocity components in the surface layer under convective conditions. *Boundary-Layer Meteorology* **11**, 355–361.

BIBLIOGRAPHY

- PAPADOPOULOS, K. H., HELMIS, C. G. & AMANATIDIS, G. T. 1992 An analysis of wind direction and horizontal wind component fluctuations over complex terrain. *Journal of Applied Meteorology* **31**, 1033–1040.
- PASCHEKE, F., BARLOW, J. F. & ROBINS, A. 2008 Wind-tunnel modelling of dispersion from a scalar area source in urban-like roughness. *Boundary-Layer Meteorology* **126**, 103–124.
- PASQUILL, F. 1974 *Atmospheric Diffusion*, 2nd edn. Wiley.
- PELTIER, L. J., WYNGAARD, J. C., KHANNA, S. & BRASSEUR, J. G. 1996 Spectra in unstable surface layer. *Journal of the Atmospheric Sciences* **53**, 49–61.
- PRESS, W. H., TEUKOLSKY, S. A., VETTERLING, W. T. & FLANNERY, B.P. 2007 *Numerical Recipes: The Art of Scientific Computing*, 3rd edn. Cambridge University Press, New York.
- REID, J. D. 1979 Markov chain simulations of vertical dispersion in the neutral surface layer for surface and elevated releases. *Boundary-Layer Meteorology* **16**, 3–22.
- RICHARDS, P. J., HOXEY, R. P. & SHORT, J. L. 2000 Spectral models for the neutral atmospheric surface layer. *Journal of Wind Engineering and Industrial Aerodynamics* **87**, 167–185.
- ROBINS, A. 2003 Wind tunnel dispersion modelling some recent and not so recent achievements. *Journal of Wind Engineering and Industrial Aerodynamics* **91**, 1777–1790.
- ROBINS, A. G. 1978 Plume dispersion from ground level sources in simulated atmospheric boundary layers. *Atmospheric Environment* **12**, 1033–1044.
- ROBINS, A. G., APSLEY, D. D. & CERC 2009 Modelling of building effects in ADMS.
- ROCKLE, R. 1990 Bestimmung der Stömungsverhältnisse im Bereich komplexer Bauungsstrukturen. Ph.d. thesis, Vom Fachbereich Mechanik, der Technischen Hochschule Darmstadt, Germany.
- RODI, W. 1997 Comparison of LES and RANS calculations of the flow around bluff bodies. *Journal of Wind Engineering and Industrial Aerodynamics* **69–71**, 55–75.
- SHARAN, M., SINGH, M. P. & YADAV, A. K. 1996 Mathematical model for atmospheric dispersion in low winds with eddy diffusivities as linear functions of downwind distance. *Atmospheric Environment* **30**, 1137–1145.
- SHARAN, M. & YADAV, A. K. 1998 Simulation of diffusion experiments under light wind, stable conditions by a variable K-theory model. *Atmospheric Environment* **32**, 3481–3492.

BIBLIOGRAPHY

- SMITH, F. B. & ABBOTT, P. F. 1961 Statistics of lateral gustiness at 16 meters above ground. *Quarterly Journal of the Royal Meteorological Society* **87**, 549–.
- SNYDER, W. H. & LAWSON, R. E. JR. 1993 Wind-tunnel simulation of building downwash from electric-power generating stations. Part II: pulsed-wire measurements in the vicinity of steam-boiler building. . Fluid Modeling Facility Internal Report, US-EPA.
- STULL, R. B. 1988 *An introduction to boundary layer meteorology*, 1st edn. Kluwer Academic Publishers.
- TAYLOR, G. I. 1921 Diffusion by continuous movements. *Proceedings to the London Mathematical Society* **20**, 196–212.
- TAYLOR, G. I. 1959 The present position in the theory of turbulent diffusion. *Adv. Geophys.* **6**, 101.
- TAYLOR, P. A. & SALMON, J. R. 1993 A model for the correction of surface wind data for sheltering by upwind obstacles. *Journal of Applied Meteorology* **32**, 1683–1694.
- TENNEKES, H. & LUMLEY, J. L. 1972 *A first course in turbulence*. MIT Press.
- TIELEMAN, H. W. 1995 Universality of velocity spectra. *Journal of Wind Engineering and Industrial Aerodynamics* **56**, 55–69.
- TINARELLI, G., ANFOSSI, D., BIDER, M., FERRERO, E. & CASTELLI, S. TRINI 1998 A new high performance version of the Lagrangian particle dispersion model spray, some case studies. In *Proceedings of the 23rd CCMS-NATO meeting, Varna*, pp. 499–507. Kluwer Academic.
- UEHARA, K., MURAKAMI, S., WAKAMATSU, S. & IKESAWA, T. 2001 Flow and concentration fields within and above asymmetric model urban street canyons in a wind tunnel. *J. Archit. Plann. Environ. Eng.* **541**, 37–42.
- UEHARA, K., WAKAMATSU, S. & MORIGUCHI, Y. 1993 Wind-tunnel experiments on diffusion of automobile exhaust gas in urban area (in Japanese). F-47-'93. National Institute for Environmental Studies (<http://www.nies.go.jp/kanko/gyomu/index.html>).
- US-EPA 1987 User's guide for the Industrial Source Complex (isc) dispersion models (revised), Volume 1,2, and 3. . U.S. Environmental Protection Agency, EPA-454/B-95-003a-c.
- US-EPA 2004 User's guide for the ams/epa regulatory model – AERMOD. *Tech. Rep.*. U.S. Environmental Protection Agency, EPA-454/B-03-001.
- WILLIAMS, M. D., BROWN, M. J., SINGH, B. & BOSWELL, D. 2004 QUIC-PLUME theory guide. La-ur-04-0561. Los Alamos National Laboratory.

BIBLIOGRAPHY

- WYGNANSKI, I., CHAMPAGNE, F. & MARASLI, B. 1986 On the large-scale structures in two-dimensional, small-deficit, turbulent wakes. *Journal of Fluid Mechanics* **168**, 31–71.
- YOSHIKAWA, Y., HAYASHI, S., HIRAI, H. & UEHARA, K. 2003 Roadside air quality simulation model for urban main roads in Japan Clean Air Program (I). *Journal of Japan Society for Atmospheric Environment* **38**, 269–286, in Japanese.
- YOSHIKAWA, Y. & KUNIMI, H. 1998 Numerical simulation model for predicting air quality along urban main roads: first report, development of atmospheric diffusion model. *Heat Transfer-Japanese Research* **27**, 483–496.

RESEARCH REPORT FROM
THE NATIONAL INSTITUTE FOR ENVIRONMENTAL STUDIES, JAPAN
No. 207

(R-207-2012)
Development of a roadside atmospheric diffusion model MCAD

Published by the National Institute for Environmental Studies
16-2 Onogawa, Tsukuba, Ibaraki 305-8506, Japan
January 2012

Asahi Printing Co., Ltd.
2-11-15, Higashi, Tsukuba, Ibaraki 305-0046, Japan
TEL+81-29-851-1188

This publication is printed on paper manufactured entirely from recycled material (Rank A), in accordance with the Law Concerning the Promotion of Procurement of Eco-Friendly Goods and Services by the State and Other Entities.